

Function of the actin nucleator mitoSPIRE1 in mitochondrial dynamics



DISSERTATION

ZUR ERLANGUNG DES DOKTORGRADES
DER NATURWISSENSCHAFTEN (DR. RER. NAT.)
DER FAKULTÄT FÜR BIOLOGIE UND VORKLINISCHE MEDIZIN
DER UNIVERSITÄT REGENSBURG

vorgelegt von

Felix Straub

aus

Weingarten

im Jahr

2020

Das Promotionsgesuch wurde eingereicht am:
20 Februar 2020

Die Arbeit wurde angeleitet von:
Prof. Dr. rer. nat. Eugen Kerkhoff

Unterschrift:

Datenblatt

Titel der Arbeit: Function of the actin nucleator mitoSPIRE1 in mitochondrial dynamics

Institut: Neurologie, Molekulare Zellbiologie, Universitätsklinikum Regensburg

Name, Vorname: Straub, Felix

Erstgutachter: Prof. Dr. rer. nat. Eugen Kerkhoff

Zweitgutachter: Prof. Dr. rer. nat. Christian Wetzel

Drittprüfer: Prof. Dr. rer. nat. Veronica Egger

Ersatzprüfer: Prof. Dr. rer. nat. Stephan Schneuwly

Prüfungsvorsitzender: Prof. Dr. rer. nat. Oliver Bosch

Eidesstattliche Erklärung

Ich, Felix Straub, geboren am 21.05.1991 in Weingarten,

versichere hiermit, dass ich die vorliegende Arbeit ohne unzulässige Hilfe Dritter und ohne Benutzung anderer als der angegebenen Hilfsmittel angefertigt habe. Ergebnisse, Abbildungen und Beschreibungen, die im Rahmen einer Kollaboration entstanden sind, habe ich entsprechend gekennzeichnet.

Die Stellen, die anderen Werken dem Wortlaut oder dem Sinn nach entnommen sind, habe ich durch Angabe der Quelle kenntlich gemacht. Insbesondere habe ich nicht die entgeltliche Hilfe von Vermittlungs- bzw. Beratungsdiensten (Promotionsberater oder andere Personen) in Anspruch genommen.

Ich erkläre hiermit weiterhin, dass ich meine wissenschaftlichen Arbeiten nach den Prinzipien der guten wissenschaftlichen Praxis gemäß der gültigen „Grundsätze zur Sicherung guter wissenschaftlicher Praxis“ der Universität Regensburg angefertigt habe.

Die Arbeit wurde bisher weder im In- noch im Ausland in gleicher oder ähnlicher Form einer anderen Prüfungsbehörde vorgelegt.

Figure 2, 11 und 13, sowie Abschnitte des Kapitels „Material und Methoden“ der hier vorliegenden Arbeit enthalten Inhalte bereits veröffentlichter Publikationen (Alzahofi, Robinson, Welz et al., 2018; Kollmar, Welz, Straub et al., 2019). Die besagten Inhalte wurden ausschließlich durch mich generiert / illustriert und sowohl für die Dissertation als auch für die genannten Publikationen erstellt.

Im Kapitel „Material und Methoden“ wurden Standardformulierungen (wie beispielsweise der Satzbaustein „*heating and shaking*“) der Arbeitsgruppe Kerkhoff zur Beschreibung der verwendeten Methodik benutzt. Diese Standardformulierungen finden sich in Publikationen sowie Protokollen der AG Kerkhoff wieder und wurden in der vorliegenden Arbeit nicht gekennzeichnet.

30.06.2020

Ort, Datum



Felix Straub

Table of contents

Datenblatt	II
Eidesstattliche Erklärung	III
Abstract.....	VIII
Zusammenfassung	IX
1. Introduction.....	1
1.1 Preamble	1
1.2 Mitochondrial dynamics	1
1.2.1 Mitochondrial fission.....	3
1.2.2 Mitochondrial fusion	4
1.2.3 Mitochondrial motility.....	5
1.3 Actin nucleators facilitate actin polymerization.....	6
1.3.1 SPIRE proteins	7
1.3.2 mitoSPIRE1	10
1.4 Cooperation of SPIRE and formin proteins.....	10
1.5 The SPIRE and myosin 5 interaction	14
1.6 Cellular functions of SPIRE proteins	16
1.6.1 SPIRE actin nucleators drive oocyte maturation.....	16
1.6.2 SPIRE actin nucleators drive vesicular transport processes.....	17
1.6.3 SPIRE1 / FMN1 / MYO5A cooperate in cytoplasmic melanosome dispersion.....	18
1.7 Knockout mouse models of the actin nucleators SPIRE and FMN subgroup formins ..	21
1.7.1 The <i>SPIRE1</i> mutant mouse.....	21
1.7.2 The FMN1 knockout mouse.....	22
1.7.3 The FMN2 knockout mouse	22
1.8 Mutations of the human FMN2 protein.....	23
1.9 Aim of the thesis.....	23
2. Materials and methods.....	25
2.1 Primer design.....	25
2.2 Agarose gel electrophoresis.....	25
2.3 Agarose gel clean-up	26
2.4 RNA isolation	26
2.4.1 RNA isolation of mouse organs.....	26
2.4.2 Total RNA isolation from eukaryotic cultured cells	26

2.4.3 Analysis of RNA / DNA purity and concentration.....	26
2.4.4 RNA quality.....	27
2.5 PCR techniques.....	27
2.5.1 Reverse transcription (synthesis of cDNA).....	27
2.5.2 Amplification of cDNA fragments.....	28
2.5.3 Amplification of genomic DNA fragments (genotyping of mice).....	29
2.5.4 Amplification of cDNA fragments for cloning.....	30
2.5.5 Quantitative real-time PCR.....	31
2.6 Cloning.....	32
2.6.1 Restriction digest and ligation of DNA vectors.....	32
2.6.2 Transformation of Escherichia coli bacterial cells.....	33
2.6.3 Plasmid DNA extraction and purification from bacterial cells.....	33
2.6.4 Control digests and DNA sequencing of plasmids.....	34
2.7 Cell culture techniques.....	34
2.7.1 Thawing cells.....	35
2.7.2 Freezing cells.....	35
2.7.3 Seeding cells.....	36
2.7.4 Staining of mitochondria in eukaryotic cells.....	36
2.7.5 Transfection of eukaryotic cells using Lipofectamine2000 reagent.....	37
2.8 Colocalization studies.....	37
2.9 Immunostaining.....	37
2.10 Microscopy.....	38
2.10.1 Microscopy of <i>in situ</i> hybridization experiments.....	38
2.10.2 Fluorescence microscopy of fixed and immunostained cells.....	38
2.10.3 Fluorescence microscopy of viable cells.....	38
2.11 Quantification of mitochondrial length using microscopy and ImageJ.....	39
2.12 Quantification of mitochondrial motility.....	39
2.13 Analysis of MYO5A positive mitochondria and mitochondrial sizes using FAMS....	40
2.14 Software.....	41
2.14.1 Statistical analysis.....	41
2.14.2 Graphs and cartoons.....	42
2.14.3 Written work.....	42
2.14.4 Identification of protein domains.....	42
2.14.5 DNA and cDNA sequences.....	43
2.15 Mitochondrial respiration.....	43
2.16 Isolation of pMEFs from mouse embryos.....	43
2.17 <i>In situ</i> hybridization.....	44
2.18 Protein work.....	46

2.18.1 Recombinant protein expression and purification	46
2.18.2 GST-pulldown from wild type and mitoSPIRE1 knockout fibroblast lysates	47
2.18.3 Immunoblotting	47
2.19 Generation of the mitoSPIRE1 knockout mouse.....	48
2.19.1 Overview of generating the mitoSPIRE1 knockout mouse.....	49
2.19.2 Guide selection and cloning of CRISPR constructs	50
2.19.3 Embryonic Stem Cell targeting	50
2.19.4 Genotyping and targeting efficiency	50
2.19.5 Off target screening	51
2.19.6 Chimeric mice generation and breeding.....	51
3. Results.....	52
3.1 Expression of <i>SPIRE</i> splice variants in mouse tissues	54
3.2 Similar expression patterns of <i>SPIRE1</i> and <i>mitoSPIRE1</i> in the mouse brain	56
3.3 Subcellular localization of SPIRE proteins	57
3.4 Interaction of mitoSPIRE1 with the outer mitochondrial membrane.....	59
3.5 mitoSPIRE1 targets FMN subfamily formin proteins towards mitochondria.....	63
3.6 mitoSPIRE1 targets MYO5 actin motor proteins towards mitochondria.....	67
3.7 Generation of a mitoSPIRE1 knockout mouse model.....	71
3.8 Mitochondria integrity in mouse SPIRE knockout models.....	74
3.8.1 Influence of SPIRE absence on mitochondrial morphology	74
3.8.2 Influence of <i>SPIRE1</i> absence on mitochondrial respiration.....	77
3.8.3 Function of mitoSPIRE1 in mitochondrial motility	78
3.8.4 Overexpression of mitoSPIRE1 influences mitochondrial motility.....	81
4. Discussion	84
4.1 Expression of <i>SPIRE</i> splice variants in mouse tissues	85
4.2 Similar expression patterns of <i>SPIRE1</i> and <i>mitoSPIRE1</i> in the mouse brain	87
4.3 Subcellular localization of SPIRE proteins	88
4.4 Interaction of mitoSPIRE1 with the outer mitochondrial membrane.....	89
4.5 mitoSPIRE1 targets FMN subfamily formin proteins towards mitochondria.....	90
4.6 mitoSPIRE1 targets MYO5 actin motor proteins towards mitochondria.....	91
4.7 Generation of a mitoSPIRE1 knockout mouse model.....	92
4.8.1 Influence of SPIRE absence on mitochondrial morphology	94
4.8.2 Influence of <i>SPIRE1</i> absence on mitochondrial respiration.....	96
4.8.3 Function of mitoSPIRE1 in mitochondrial motility	97

4.9 Model for mitoSPIRE1 function in mitochondrial transport processes	99
5. References	103
6. Supplement.....	116
6.1 Overview of used materials	116
6.1.2 Chemicals and reagents	116
6.1.3 Cell culture media, reagents and supplements.....	118
6.1.4 Buffers, solutions and media	119
6.1.5 Disposable materials.....	122
6.1.6 Kits.....	123
6.1.7 Antibodies.....	124
6.1.7.1 Primary antibodies	124
6.1.7.2 Secondary antibodies	124
6.1.8 Enzymes.....	124
6.1.8.1 Restriction endonucleases.....	124
6.1.8.2 DNA polymerases.....	125
6.1.8.3 Additional enzymes	125
6.1.9 Primer (PCR / qPCR)	125
6.1.10 Mouse lines.....	126
6.1.11 Machines and equipment.....	127
6.1.12 Eukaryotic expression vectors	128
6.1.12.1 pAcGFP1-C1 (Clontech).....	128
6.1.12.2 pcDNA3 (Invitrogen)	128
6.1.12.3 pEGFP-C1 (Clontech)	128
6.1.12.4 pEGFP-C2 (Clontech)	129
6.1.12.5 pmStrawberry-C1	129
6.1.12.6 List of used constructs	129
6.1.13 Sequence related data	130
6.2 Amino acids, one letter code	131
7. List of abbreviations	132
8. List of Figures	135
9. List of Tables	137
10. Acknowledgements / Danksagung	138

Abstract

Cells of all known living organisms require a constant energy supply in the form of adenosine triphosphate (ATP) for their survival and function. The intracellular transport and diffusion of ATP molecules are rather limited and thus, ATP producing mitochondria are directly transported to their site of action such as synaptic densities to provide all cellular compartments with an adequate amount of ATP. Fast and long-range transport of mitochondria along microtubule tracks via kinesin and dynein motor proteins is well established, whereas only little is known about actin / myosin functions in mitochondrial transport. There is growing evidence that actin filaments and myosin motor proteins play an essential role in the transport of mitochondria. A SPIRE formin actin nucleator complex facilitates actin filament generation. In addition, SPIRE proteins coordinate myosin 5 (MYO5) motor protein activation at vesicle and organelle membranes. Due to alternative splicing of the *SPIRE1* gene, mammalian cells generate four SPIRE proteins from two *SPIRE* genes. The SPIRE1 actin / myosin organizer is targeted by the alternatively spliced exon 13 towards mitochondrial membranes and the corresponding protein is named 'mitoSPIRE1'. The present thesis quantitatively addressed the expression of all *SPIRE* splice variants including *mitoSPIRE1* in distinct organs, showing that the brain has the majority of *SPIRE* expression. In a previous study it was shown that *SPIRE1* mutant mice lacking the expression of all *SPIRE1* proteins, including mitoSPIRE1, have increased fear in both cued and contextual fear conditioning experiments. To dissect the vesicular and mitochondrial SPIRE functions in fear behavior and to analyze the function of the mitoSPIRE1 protein in more detail, we generated a novel knockout model by targeted deletion of the mouse *SPIRE1 exon 13* - the mitoSPIRE1 knockout mouse. Fibroblasts of the novel mitoSPIRE1 knockout mouse and the *SPIRE1* mutant mouse show increased mitochondrial motility in live cell fluorescence microscopy analysis. Colocalization studies unraveled that mitoSPIRE1 colocalizes with FMN subfamily formins and MYO5 proteins at mitochondria. Subsequent fluorescence-activated mitochondria sorting (FAMS) experiments confirmed that SPIRE proteins contribute to target MYO5 actin motor proteins towards mitochondrial membranes. Furthermore, FAMS and fluorescence microscopy revealed an influence of mitoSPIRE1 on mitochondrial morphology. SPIRE proteins did not influence mitochondrial oxygen consumption rate, which was analyzed by a *Seahorse Mito Stress Test* assay. The mentioned function of mitoSPIRE1 in the regulation of mitochondrial motility led us to speculate that mitoSPIRE1 might be involved in targeting mitochondria towards synaptic terminals and thereby influencing synaptic transmission and possibly fear behavior.

Zusammenfassung

Sämtliche Zellen lebender Organismen benötigen für ihr Überleben und die erfolgreiche Ausführung der zellulären Funktion eine ausreichende Menge an Energie in Form von Adenosintriphosphat (ATP). Die Diffusion und der Transport von einzelnen Molekülen wie ATP, welches hauptsächlich von Mitochondrien synthetisiert wird, ist intrazellulär stark eingeschränkt. Aus diesem Grund werden Mitochondrien über ein Transportsystem an ihren Einsatzort, beispielsweise synaptische Kontakte, bewegt. In der Literatur ist bereits detailliert beschrieben, dass Kinesin- und Dynein-Motoren einen schnellen, weitreichenden und bidirektionalen Mitochondrientransport entlang von Mikrotubuli ermöglichen. Gleichzeitig ist über einen möglichen mitochondrialen Transport entlang von Aktinfilamenten mittels Myosin-Motoren bisher nur wenig bekannt. Dennoch häufen sich die Hinweise, dass Aktinfilamente sowie Myosin-Motoren den mitochondrialen Transport beeinflussen. Die intrazelluläre Aktinfilament-Bildung wird unter anderem durch den SPIRE / Formin Aktinnukleations-Komplex ermöglicht. Zusätzlich koordinieren SPIRE Proteine die Aktivierung von Myosin 5 Motoren an Vesikel- und Organell-Membranen. Durch alternatives Spleißen entstehen in einer Säugetier-Zelle aus zwei *SPIRE* Genen insgesamt vier SPIRE Proteine. Hierbei wird durch das alternative Spleißen der *SPIRE1* mRNA ein Protein synthetisiert, welches das alternative Exon 13 des *SPIRE1* Genes enthält. Das zusätzliche Exon 13 lokalisiert das eigentlich vesikuläre SPIRE1 Protein an die mitochondriale Membran, weshalb dieses dementsprechend als „mitoSPIRE1“ bezeichnet wird. In der hier vorliegenden Arbeit wurde die Expression aller *SPIRE* Spleißvarianten inklusive *mitoSPIRE1* in verschiedenen Organen der Maus quantitativ adressiert. Hierbei konnte gezeigt werden, dass das Gehirn der Hauptexpressionsort für *SPIRE* ist. In der Literatur wurde bereits ein Maus-Modell beschrieben, welches keinerlei funktionelle Proteine des *SPIRE1* Gens exprimiert und ein erhöhtes Angstverhalten in kontextuellen und reiz-induzierten Angstkonditionierungs-Experimenten aufweist. Um die Funktion des vesikulären und mitochondrialen SPIRE auf das Angstverhalten zu analysieren und die generelle mitoSPIRE1 Funktion zu untersuchen wurde in dieser Arbeit mittels Deletion des *SPIRE1 Exon 13* ein neues *Knock-out* Modell erstellt - die mitoSPIRE1 *Knock-out* Maus. In nachfolgenden Fluoreszenz-Mikroskopie-Analysen lebender Zellen zeigen Fibroblasten der neuen mitoSPIRE1 *Knock-out* Maus und der *SPIRE1* mutant Maus, welche keinerlei funktionsfähige Proteine des *SPIRE1* Genes besitzt, eine erhöhte mitochondriale Motilität. Außerdem konnte durch eine umfassende Kollokalisations-Studie gezeigt werden, dass das mitochondriale

mitoSPIRE1 mit FMN und MYO5 Proteinen an Mitochondrien kolokalisiert. Hierbei wurde durch *fluorescence-activated mitochondria sorting* (FAMS) Experimente bestätigt, dass unter anderem SPIRE für die Translokation von MYO5 Proteinen auf mitochondriale Membranen benötigt wird. Zusätzlich wurde mittels FAMS und mikroskopischen Analysen gezeigt, dass mitoSPIRE1 die mitochondriale Morphologie beeinflusst. Im Gegensatz dazu haben SPIRE Proteine des *SPIRE1* Genes keinen Einfluss auf die *oxygen consumption rate* der Mitochondrien, was mit einem *Seahorse Mito Stress Test* Assay festgestellt wurde. Die hier gezeigte Funktion von mitoSPIRE1 in der mitochondrialen Motilität impliziert, dass mitoSPIRE1 die mitochondriale Verankerung an synaptischen Nervenenden und aus diesem Grund die synaptische Transmission und das Angstverhalten beeinflussen könnte.

1. Introduction

1.1 Preamble

Evolutionary adaptation over millions of years generated animals which can rapidly react in response to external cues and are able to solve complex tasks. A perfect combination of energy consuming organs is required to recognize, evaluate and react to distinct events in time and space. In this respect, the analysis of changing environmental allurements is a continuous challenge for the organism and desires an adaptable processing system. To process complex novel information, neuronal networks of animal brains undergo structural and functional alterations induced by external and internal stimuli (Sehgal et al., 2013). In this context, the energy consuming structural rearrangement of synapses and dendrites is the cellular correlate for the process of learning, memory and cognition (Hamdan et al., 2011; van Bokhofen, 2011). To facilitate such adaptive alterations on a molecular level, the eukaryotic cytoskeleton plays a fundamental role, with the cytoskeleton serving as a transport system and being used together with mitochondria to provide distinct cell areas with energy in the form of ATP (Hollenbeck and Saxton, 2005; Mandal and Drerup, 2019). The filamentous components of the cytoskeleton build a highly dynamic system, which constantly undergoes alterations and facilitates the cell adaptation to distinct environmental influences (Fletcher and Mullins, 2010).

1.2 Mitochondrial dynamics

Eukaryotic cells require a constant energy supply in the form of adenosine triphosphate (ATP) for their survival and proper function (Nicholls and Budd, 2000). Mitochondria work as cellular power plants and provide all cell areas with an adequate amount of ATP (Sheng, 2014). In addition, these organelles function as Ca^{2+} storage for neurotransmission (Medler and Gleason, 2002), produce precursors for macromolecules, such as proteins or lipids, and generate metabolic byproducts like reactive oxygen species (Spinelli and Haigis, 2018). Overall mitochondrial function is very complex and is facilitated by the specific organelle structure, as mitochondria are enveloped by an inner and an outer membrane resulting in the intermembrane space and the mitochondrial matrix (Pagliuso et al., 2018). However, mitochondria are highly dynamic organelles undergoing processes of fission, fusion and controlled recycling called mitophagy (Chen and Chan, 2009). Furthermore, mitochondria migrate along the cytoskeleton to distinct cell areas where energy is needed. Fission, fusion and motility are the main components of mitochondrial dynamics, and allow these organelles to provide the demanded

energy in space and time. As a consequence of these dynamic processes, mitochondria are able to adapt to environmental and physiological requirements (Chen and Chan, 2009). In this context, mitochondrial fission and fusion events, as well as mitochondrial motility highly depend on the cellular subtype and its metabolic activity (Pagliuso et al., 2018). Mitochondrial dynamics influence the structure, function and the overall morphology of the organelle, and therefore, their functional integrity is of great importance for cellular homeostasis (Figure 1). Abnormalities in mitochondrial dynamics often lead to cellular dysfunction and can be lethal or result in diseases, particularly neurodegenerative diseases (Chen and Chan, 2009). These severe consequences for the organism show the importance of mitochondrial integrity by itself and the associated mitochondrial dynamics.

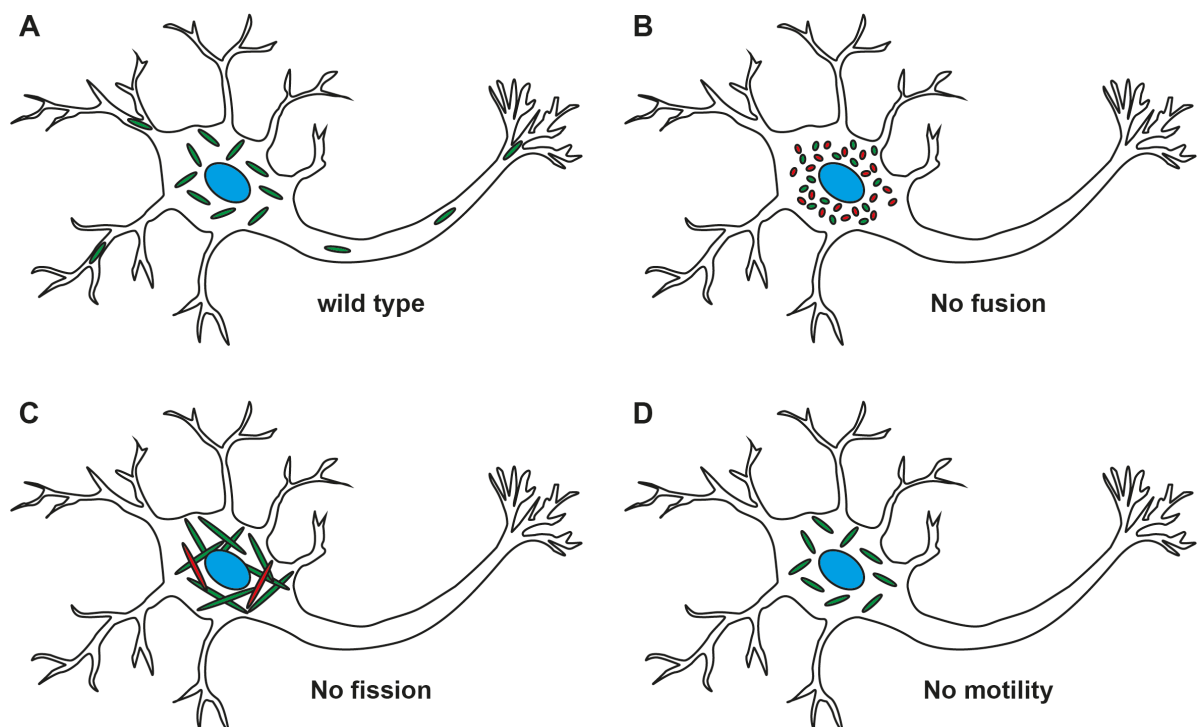


Figure 1 - Mitochondrial dynamics is characterized by fission, fusion and motility. A change of mitochondrial dynamics influences the function of mitochondria and can alter the supply of energy in distinct subcellular areas. **(A)** In wild type neurons, mitochondria are transported along the cytoskeleton to distinct cell areas and are well distributed to provide energy all over the cell. Mitochondria are functional and not fragmented or elongated. **(B)** A loss of mitochondrial fusion leads to fragmented mitochondria and a subpopulation of fragmented mitochondria becomes dysfunctional (*red*). In addition, fragmented mitochondria show transport defects to distal cell areas. **(C)** In the absence of mitochondrial fission, the mitochondrial population shows extremely elongated mitochondria and a subpopulation is not functional anymore (*red*). The elongated mitochondria show dysfunction in transport and cluster around the nucleus. **(D)** Without functional transport machinery, the mitochondria are not distributed throughout the cell but rather cluster in the perikaryon (modified from Chen and Chan, 2009).

1.2.1 Mitochondrial fission

The ratio of mitochondrial fission and fusion events determines the length of mitochondria. Mitochondrial fission is characterized by the division of a mitochondrion into two daughter mitochondria. In the case of excessively frequent fission events, the balance between fission and fusion is shifted, resulting in a large number of fragmented mitochondria (van der Bliek et al., 2013). Mitochondrial fission is probably required to ensure that a population of organelles is available for segregation, to produce smaller organelles that are easier to transport along the cytoskeleton, to maintain a healthy population of organelles, and to transfer mitochondrial DNA between organelles (Kraus and Ryan, 2017). Mice without effective mitochondrial fission die shortly after birth, which shows the necessity of mitochondrial fission in Mammalia (Ishihara et al., 2009). Mitochondrial fission is a complex process that requires the interplay of many proteins and actin filaments (Korobova et al., 2013, 2014; Hatch et al., 2014; Li et al., 2015; Manor et al., 2015; Lee et al., 2016). Mitochondrial fission can be separated into two consecutive / sequential stages; in the first stage, the mitochondrial diameter is significantly reduced at fission sites. This beginning step involves the endoplasmic reticulum (ER) wrapping around the mitochondrial membranes, which marks the fission zones and initiates constriction (Friedman et al., 2011). Along these fission zones, actin polymerization occurs and exerts pressure on the mitochondrial outer membrane to perform mitochondria constriction, because the floppy ER tubules fail to do so (Korobova et al., 2013, 2014; Hatch et al., 2014; Manor et al., 2015). The ER associated actin nucleator Inverted formin 2 (INF2) and the mitochondria located actin nucleator mitoSPIRE1 (also known as SPIRE1C or SPIRE1-E13) are thought to interact, and thus to facilitate actin polymerization at constriction sites (Manor et al., 2015). The second stage of mitochondrial fission describes the final mitochondrial membrane scission. The scission event is initiated by the GTPase dynamin-related protein 1 (Drp1), which forms a polymeric ring after being recruited to fission zones at the outer mitochondrial membrane (Smirnova et al., 2001; Lackner and Nunnari, 2009; Archer, 2013). The Drp1 ring is not large enough to enclose tubules of human mitochondria, which often have a diameter of ~ 300 nm. For the generation of a Drp1 polymeric ring the mitochondrial diameter should not be larger than ~ 150 nm (Friedman et al., 2011). That is why the mitochondrial constriction of the first fission stage reduces the diameter at fission zones to the appropriate size so that Drp1 can build the polymeric ring (Lackner and Nunnari, 2009; Friedman et al., 2011; Archer, 2013; Manor et al., 2015). Like it was done in the first fission stage the Drp1 polymeric ring exerts pressure on the mitochondrial fission zone. After the fission zone is narrowed to its maximum,

dynamamin-2 is recruited to the constricted area and drives the final membrane scission event (Lee et al., 2016; Kraus and Ryan, 2017).

1.2.2 Mitochondrial fusion

The balance between the opposed processes of mitochondria organelle fission and fusion regulates mitochondria number and size (Liesa et al., 2009). Mitochondrial fusion is characterized by two mitochondria merging into one mitochondrion. An excessive increase of mitochondria fusion events brings the equilibrium of mitochondrial fission and fusion out of balance, resulting in a large number of hyperfused mitochondria (Pagliuso et al., 2018). Fusion of mitochondria is required to mix mitochondrial contents like mitochondrial DNA (mtDNA) to maintain a homogenous population of organelles, and to prevent the permanent loss of essential components. Consequently, a decreased rate of fusion events results in a subpopulation of mitochondria that lack functional mtDNA. Mitochondria with deficient mtDNA show respiration defects and can impair the neuronal outgrowth, thereby promoting neurodegenerative diseases (Chen and Chan, 2010). Mitochondrial fusion can be separated into two stages; The first stage describes the outer mitochondrial membrane (OMM) fusion of two mitochondria mediated by the membrane-anchored dynamamin GTPase family members mitofusin 1 (Mfn1) and mitofusin 2 (Mfn2). In the second step, the inner mitochondrial membrane (IMM) fusion is mediated by the optic atrophy 1 (OPA1) protein. In the absence of mitofusins, the fusion of both the inner and the outer mitochondrial membrane is abolished (Chen and Chan, 2009). The need for mitochondrial fusion is demonstrated by two knockout mouse models which lack either Mfn1 or Mfn2. A homozygous knockout of Mfn1 or Mfn2 results in embryonic lethality. In contrast, heterozygous animals demonstrate full viability and fertility (Chen et al. 2003). Interestingly, heterozygous mutations in human Mfn2 cause an axonal peripheral neuropathy, known as Charcot-Marie-Tooth disease type 2A (Amiott et al., 2008). In addition, heterozygous mutations in the human *OPA1* gene can cause dominant optic atrophy. Patients who suffer from dominant optic atrophy develop a bilateral degeneration of the optic nerves, and usually lose their visual sense within the first decade of their life (Lenaers et al., 2012).

1.2.3 Mitochondrial motility

Diffusion and transport of intracellular molecules like ATP are rather limited, and therefore simple molecule diffusion is not sufficient to provide all cell areas with energy (Kinsey et al., 2011). A complex transport machinery enables mitochondrial motility, and facilitates transport of these cellular power plants to their sites of operation (Hollenbeck and Saxton, 2005). The mitochondrial transport system is essential, especially in highly polarized cells, such as neurons, to efficiently distribute mitochondria to distal cell compartments (Hollenbeck and Saxton, 2005; Sheng, 2014). A dysfunction in the mitochondrial transport machinery results in the absence of mitochondria in dendrites and axons, leading to neurotransmission defects (Guo et al., 2005). In addition, transport defects of mitochondria can influence mitochondrial morphology resulting in an imbalance of fission and fusion events (Varadi et al., 2004). Mitochondrial trafficking in neurons and thus their distribution depends on synaptic activity, certain stress conditions, and mitochondria integrity (Miller and Sheetz, 2004; Chang and Reynolds, 2006; Cai et al., 2012; Sheng, 2014). In mature neurons, ~ 20 - 30 % of axonal mitochondria are motile whereas the remaining mitochondria are stationary. Mitochondria are specifically docked / anchored to synaptic sites in order to provide a stable ATP supply as stationary power plants (Kang et al., 2008). The absence of stationary mitochondria significantly influences the synaptic vesicle release due to fluctuations in synaptic ATP levels, which are induced by mitochondrial movement (Sheng, 2014). Furthermore, spatially stable mitochondrial compartments fuel local translation during synaptic plasticity in neuronal dendrites (Rangaraju et al., 2019). As an effect of altered metabolic requirements, the anchored stationary mitochondria can become motile and motile mitochondria can become stationary (Sheng, 2014).

The molecular transport of mitochondria in mammalian neuronal cells is well researched and allows assumptions to be made about the mitochondrial transport system of other cell types. However, there is still uncertainty concerning the exact mechanism of mitochondrial targeting. It is known that mitochondria are transported along cytoskeletal components mediated by motor and adapter proteins (Hollenbeck and Saxton, 2005). The transport of axonal mitochondria is modulated by microtubule- and actin-dependent mechanisms, in which the majority of mitochondria are transported on fast tracks along microtubules via kinesin and dynein motor proteins (Hollenbeck and Saxton, 2005; Pathak et al., 2010; Sheng, 2014). Microtubules are polarized along the axonal processes, which makes it possible to study bidirectional mitochondrial transport (Heidemann et al., 1981; Baas et al., 1988, 1989). Dynein motor

proteins mediate a retrograde (towards the cell body) movement of mitochondria, whereas kinesin motor proteins drive an anterograde (towards axonal termini) mitochondria transport. KIF5, a member of the kinesin-1 family, is described as a key motor protein of neuronal mitochondrial transport (Hurd and Saxton, 1996; Tanaka et al., 1998; Górska-Andrzejak et al., 2003; Cai et al., 2005; Glater et al., 2006; Pilling et al., 2006; Sheng, 2014). In line with all other mitochondria-associated motor proteins, KIF5 does not bind directly to mitochondria, but rather interacts with the adapter protein complex Miro1-Trak2 to be finally connected to mitochondria and facilitate transport along microtubules (MacAskill et al., 2009; van Spronsen et al., 2013; Sheng, 2014). A large number of adapters between motor proteins and mitochondria have already been identified, but it is often unclear how exactly they influence mitochondrial motility and how they are regulated (Sheng, 2014). However, the adapter protein syntrophin immobilizes motile axonal mitochondria by anchoring them to microtubules, which results in stationary pools of mitochondria (Sheng, 2014). Compared to the microtubule-associated mitochondrial transport, only little is known about the role of actin / myosin forces in mitochondrial transport. The actin / myosin transport machinery might be used to move mitochondria to cell regions where there is a lack of microtubules or it could be used to recouple mitochondria to microtubules after kinesin or dynein motor proteins are disengaged (Hollenbeck and Saxton 2005). Further research into *Drosophila melanogaster* shows an increase of mitochondrial movement and velocity following myosin 5 depletion in neuronal cells. These data indicate that myosin 5 activity opposes microtubule-based axonal transport of mitochondria (Pathak et al., 2010). However, the role of actin / myosin in mitochondrial transport has not been investigated sufficiently and is not well understood. In contrast to KIF5, it is still unknown how myosin motor proteins interact with mitochondria, or which proteins might mediate their connection.

1.3 Actin nucleators facilitate actin polymerization

Actin filaments are highly dynamic and function in diverse cellular processes (Rottner et al., 2017). They provide mechanical stability and regulate cell shape, enable cell membrane dynamics and facilitate intracellular transport processes (Dominguez and Holmes, 2011; Pollard and Goldman, 2016; Rottner et al., 2017). Actin filaments are generated by the polymerization of actin monomers (G-actin) into double helical filaments (F-actin). Actin dimers and trimers are relatively unstable, and therefore a spontaneous polymerization of actin monomers into actin filaments is possible, but insufficient and rare. In addition, actin monomer

binding proteins like profilin and β -thymosin further inhibit spontaneous actin polymerization in cells (Sept and McCammon, 2001; Pollard und Cooper, 2009; Xue and Robinson, 2013). A well-regulated initiation of actin polymerization in cells in space and time is thus essential and is controlled by a large set of actin nucleators. These actin nucleators bind actin monomers and stabilize an actin nucleus (dimer, trimer, tetramer), which enables further polymerization (Firat-Karalar and Welch, 2011). There are three major classes of actin nucleators; namely the Arp2/3 complex, the formin superfamily and the Wiskott-Aldrich-Syndrome protein homology 2 (WH2) domain containing nucleators, including the SPIRE proteins. These actin nucleators differ in their molecular mechanisms to initiate actin polymerization (Robinson et al., 2001; Quinlan et al., 2005; Kerkhoff, 2006; Schönichen and Geyer, 2010; Carlier et al., 2011).

1.3.1 SPIRE proteins

SPIRE proteins were first identified in 1999 / 2000 and were shown to play a role in *Drosophila* oocyte maturation (Wellington et al., 1999; Otto et al., 2000). Twenty years later, modern technology traced back the origin of SPIRE to be at least a holozoan invention, because SPIRE proteins were found in *Ichthyosporea*, *Choanoflagellida*, and *Metazoa* (Kollmar, Welz, Straub et al., 2019). Mammals have two *SPIRE* genes, namely *SPIRE1* and *SPIRE2*. The mammalian *SPIRE1* gene locus contains two alternatively spliced exons - *exon 9* and *exon 13*. In contrast, the *SPIRE2* gene locus encodes only a single transcript (Figure 2A). As a result, the two mammalian *SPIRE* genes encode a total of four different SPIRE proteins: SPIRE1, SPIRE1-E9, mitoSPIRE1 and SPIRE2, which are highly similar proteins regarding their domain organization. The primary structure of the mouse SPIRE1 and SPIRE2 proteins show an identity of 37 % and a similarity of 50 % (Kerkhoff, 2006). SPIRE1 and SPIRE2 proteins do not contain alternatively spliced exons and have similar subcellular localization at vesicular membranes (Kollmar, Welz, Straub et al., 2019). The vesicle located SPIRE1-E9 contains the alternatively spliced exon 9, a unique 14 amino acid spanning sequence. The alternatively spliced exon 13, which encodes a sequence of 58 amino acids, is part of the mitoSPIRE1 protein, which is localized at mitochondria. A SPIRE protein containing both the exon 9 and the exon 13 was not detected (Kollmar, Welz, Straub et al., 2019).

All SPIRE proteins contain highly conserved regions in their structural protein organization (Figure 2, B, C). The SPIRE proteins consist of an N-terminal kinase non-catalytic C-lobe domain (KIND) for FMN subgroup formin interaction (Pechlivanis et al., 2009), and a cluster

of four Wiskott-Aldrich-Syndrome protein homology 2 (WH2) domains for actin monomer binding and nucleation (Quinlan et al., 2005). The globular tail domain binding motif (GTBM) in the central linker region of SPIRE proteins mediates a direct interaction between SPIRE and myosin 5 (MYO5) proteins (Pylypenko, Welz et al., 2016). The C-terminal SPIRE-box (SB) shows sequence homology to the Slp homology domain (SHD) of RAB GTPase interacting proteins like rabphilin 3A (Kerkhoff, et al. 2001; Fukuda 2013). In this context, the C-terminal SPIRE SHD-like sequences mediate the interaction between SPIRE1 and RAB27A/B (Alzahofi, Robinson, Welz et al., 2018). Furthermore, SPIRE1 and SPIRE2 interact with comparable affinity with RAB8A (Kollmar, Welz, Straub et al., 2019). This indicates the opportunity of the SPIRE-box to interact with different RAB family GTPases. The C-terminal FYVE-type zinc-finger (FYVE) domain contains a hydrophobic turret loop which integrates into lipid bilayers, enabling intracellular membrane localization of the whole protein (Misra and Hurley, 1999; Dumas et al., 2001; Kerkhoff et al., 2001; Tittel et al., 2015).

In situ hybridization in mouse brains revealed a high expression of *SPIRE1* in the hippocampus, dentate gyrus, and the cerebellum (Schumacher et al., 2004; Pleiser et al., 2010). Expression analysis in mice show that *SPIRE* mRNA is most abundant in oocytes and in the brain (Pfender et al., 2011; Pleiser, 2012). As a conclusion of the expression studies, the overall *SPIRE* expression levels seem to be low, which complicates the study of endogenous SPIRE functions. Nevertheless, in several studies, the function of SPIRE has been addressed. SPIRE nucleated actin filaments mediate long-range transport of vesicles in mouse oocytes (Schuh, 2011) and are essential for asymmetric oocyte cell division (Pfender et al., 2011). In addition, SPIRE1 function influences fear expression (Pleiser et al., 2014) and contributes to the regulation of melanosome transport in melanocytes (Alzahofi, Robinson, Welz et al., 2018).

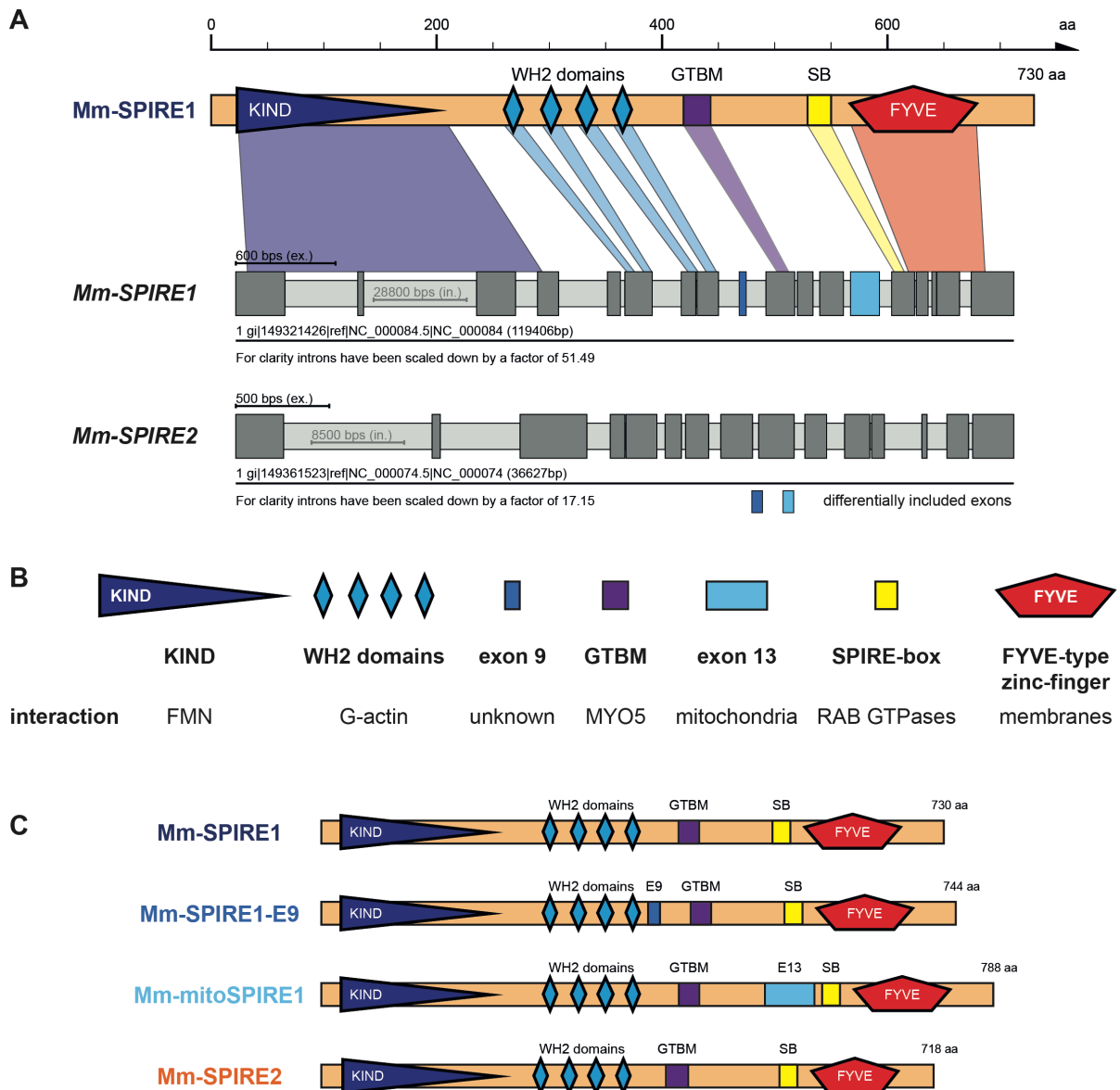


Figure 2 - Structure of mouse SPIRE genes and proteins. (A) Schematic drawing of the mouse SPIRE1 protein and the predicted gene structure of mouse *SPIRE1* and *SPIRE2*. Conserved domains of the SPIRE1 protein are highlighted in color and are assigned to their respective exon sequence. Dark and light grey boxes indicate exons and introns, respectively. Introns have been scaled down for a better presentation of the gene structures as denoted. (B) Overview on functional SPIRE protein domains and the specific interactions they mediate. *KIND*, kinase non-catalytic C-lobe domain; *WH2*, Wiskott-Aldrich-Syndrome protein homology 2; *GTBM*, globular tail domain binding motif; *FYVE*, FYVE-type zinc-finger. (C) Overview on mouse SPIRE proteins and their respective domain organizations. Numbers indicate amino acids. The *SPIRE1* gene encodes for three different proteins, SPIRE1, SPIRE1-E9 and mitoSPIRE1. The *SPIRE2* gene encodes for one protein, SPIRE2. *E9*, exon 9; *E13*, exon 13; *SB*, SPIRE-box; *aa*, amino acids. Figure 2 was already published in Kollmar, Welz, Straub et al., 2019.

1.3.2 mitoSPIRE1

The alternatively spliced actin nucleator protein mitoSPIRE1 was first described in 2015. Until recently, the protein was named SPIRE1C, because it includes the alternatively spliced exon 13 also known as exon C. Unfortunately, *Drosophila* already encodes a SPIRE protein isoform which is called SPIREC. To avoid misunderstandings, in 2019 we renamed the mammalian SPIRE1C protein in agreement with its discoverer Uri Manor into mitoSPIRE1. We chose this name, because mitoSPIRE1 is localized at mitochondria, and is a splice variant of the *SPIRE1* gene. The 58 amino acid sequence of the alternatively spliced exon 13 binds to the outer mitochondrial membrane, and targets the mitoSPIRE1 protein towards mitochondria (Manor et al., 2015). Manor and colleagues describe a role of mitoSPIRE1 in mitochondrial fission. In their current model, a dimer of mitoSPIRE1 is expected to interact with the endoplasmic reticulum (ER)-localized inverted formin 2 (INF2) to form an actin nucleation complex during ER initiated mitochondrial constriction. The subsequent nucleation and elongation of actin filaments along fission zones by the mitoSPIRE1 / INF2 complex might exert pressure on the mitochondrial outer membrane, and therefore cause constriction of the mitochondrial membrane. The mitoSPIRE1 / INF2 complex could be necessary for mitochondrial fission (Manor et al., 2015). Additional functions of mitoSPIRE1 remain unknown thus far.

1.4 Cooperation of SPIRE and formin proteins

Initial findings of the association between the two actin nucleators SPIRE and formin were already provided in the late 1980s. A mutation in the gene locus of the Cappuccino protein (a *Drosophila melanogaster* FMN2 ortholog) revealed the same phenotype in oocytes of *Drosophila melanogaster* as a mutated *SPIRE* gene (Manseau and Schüpbach, 1989). Years later, the identical oocyte phenotype was explained. SPIRE and Cappuccino cooperate to assemble a cytoplasmic mesh of actin filaments that controls a distinct microtubule organization during oocyte development (Dahlgaard et al., 2007). In addition to this functional cooperation, further studies also revealed a physical interaction between formins and SPIRE proteins (Quinlan et al., 2007; Pechlivanis et al., 2009). The mammalian FMN subgroup formins (FMN1, FMN2) and SPIRE proteins (SPIRE1, SPIRE2) interact directly with each other in order to form a functional actin nucleator complex (Pechlivanis et al., 2009; Pfender et al., 2011). The very C-terminal end of FMN1/2 contains a basic amino acid cluster in the so called formin-SPIRE Interaction (FSI) sequence, which binds to an acidic cluster in the N-terminal KIND of SPIRE proteins (Pechlivanis et al., 2009; Zeth et al., 2011).

FMN subfamily formins contain, like all formins, two formin homology domains which are termed formin homology domain 1 (FH1) and formin homology domain 2 (FH2). Formin proteins dimerize which results in a dimeric ring of the two FH2 domains that encircles and processively moves with the growing plus end of an actin filament, therefore, facilitating its elongation (Schönichen and Geyer, 2010). The FH1 domains of the formin dimer contain multiple clusters of poly-proline stretches, which enable the binding of profilin-actin and providing it to the FH2 dimer for actin filament elongation (Romero et al., 2004; Otomo et al., 2005; Paul and Pollard, 2008; Schönichen and Geyer, 2010). The actin nucleation activity of FMN formins and the binding of FH2 to barbed ends of actin filaments is inhibited by the formation of the SPIRE-FMN complex. However, the formation of the SPIRE-FMN actin nucleator complex significantly increases the overall actin nucleation in comparison to the single nucleator proteins acting alone (Vizcarra et al., 2011; Montaville et al., 2014). The SPIRE-formin complex facilitates both actin nucleation via the WH2 domains of SPIRE and actin filament elongation via FMN (Figure 3; Quinlan and Kerkhoff, 2008; Kerkhoff, 2011).

It has been shown that the four WH2 domains of SPIRE are sufficient to nucleate actin polymerization *in vitro*, but these domains are not able to nucleate actin polymerization of profilin bound actin, being the most abundant source of actin monomers in cells (Quinlan et al., 2005; Montaville et al., 2014; Pollard, 2016). Thus, for SPIRE actin nucleation actin monomers have to be provided as a non-coupled actin monomer directly or by other proteins, which are able to process profilin-actin (Quinlan et al., 2005; Montaville et al., 2014). A present model of the SPIRE-formin complex explains that SPIRE WH2 domains nucleate actin monomers and passes over to an FMN dimer which elongates the newly synthesized SPIRE nucleated filaments (Quinlan and Kerkhoff, 2008; Kerkhoff, 2011). This model accumulates evidence for the theory that FMN subfamily formins provide SPIRE with actin monomers, because FMN processes profilin-actin with its FH1 domains and as a consequence, could supply actin monomers to SPIRE (Figure 3). However, in a current model, the building of the SPIRE-formin complex leads to the dimerization of SPIRE proteins at the membrane and initiates actin nucleation (Quinlan and Kerkhoff, 2008). The increase of SPIRE WH2 domains could be an explanation for higher actin nucleation activity of SPIRE in the complex.

A further model shows that SPIRE proteins exist in two distinct states: a potentially auto-inhibited inactive state and an unfolded, membrane-bound active state (Figure 4). In the inactive state, the SPIRE protein is cytosolic and might adopt a backfolded structure by an intramolecular interaction between the C-terminal FYVE domain and the N-terminal KIND. In

this state membrane-binding of the FYVE domain is inhibited and KIND is not accessible for binding to FMN subfamily formins. In the active state, the SPIRE protein gets unfolded, is targeted to intracellular membranes and is now able to recruit FMN subfamily formins through the accessible KIND. The intramolecular FYVE / KIND and the trans-regulatory FMN-FSI / KIND interactions are competitive and couples the membrane binding of SPIRE to the recruitment of FMN subfamily formins (Tittel et al., 2015). A distinct mechanism which drives SPIRE protein activation and membrane targeting is still not completely understood. In this context, the interaction of SPIRE proteins and myosin 5 actin motors might contribute to the SPIRE activation process (Pylypenko, Welz et al., 2016).

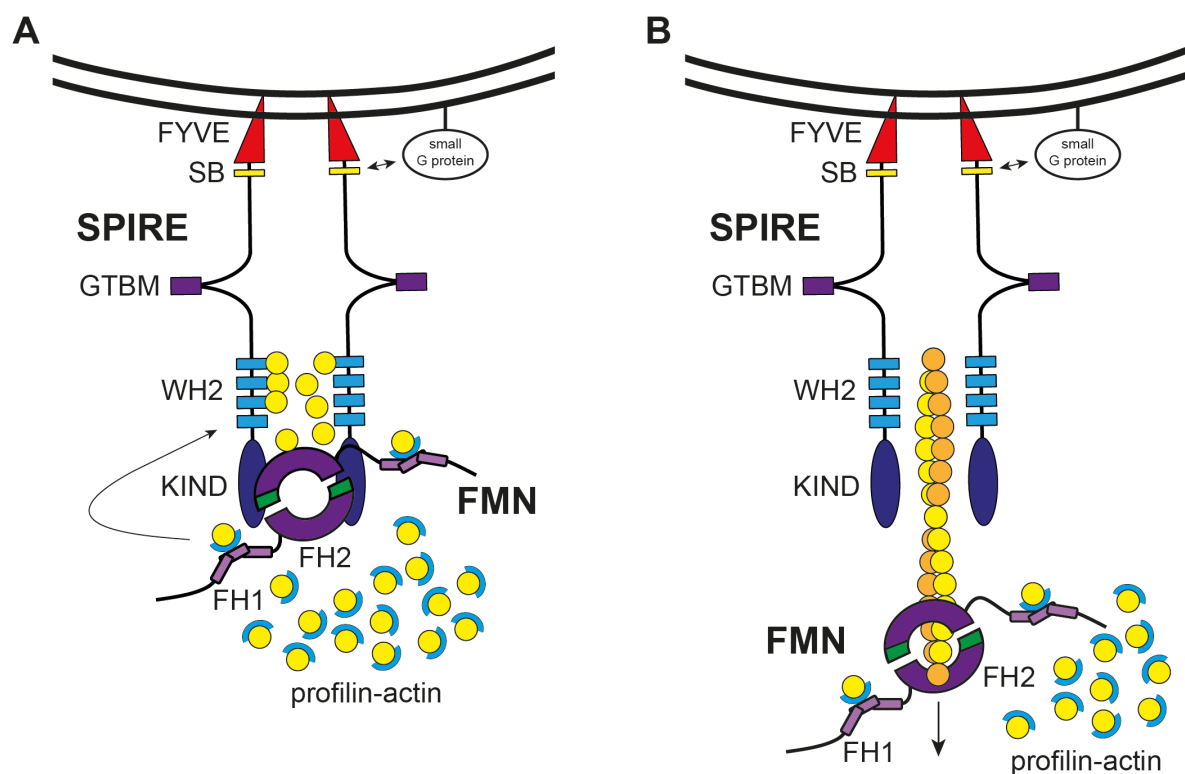


Figure 3 - Model of SPIRE / FMN subfamily formin cooperation in efficient actin nucleation and filament elongation. For actin nucleation SPIRE proteins need monomeric unbound actin molecules, whereas FMN subfamily formins can process profilin bound actin monomers which are the most abundant form of actin monomers in eukaryotic cells. In the current model SPIRE WH2 domains nucleate actin monomers and passes over to an FMN dimer which elongates the novel synthesized SPIRE nucleated filaments. (A) Activated SPIRE proteins are targeted at subcellular membranes by the interaction of the SPIRE FYVE-type zinc-finger with negatively charged lipids of the membrane. Specific subcellular localization of SPIRE proteins could be determined by the interaction of the SPIRE-box with small G-proteins like RAB27 and the localization might be influenced by dimerization of SPIRE proteins. After SPIRE dimerization FMN subfamily formins are translocated to SPIRE and FH2 domains of FMN formins form a dimer as well, whereas each FSI motif interacts directly with a single N-terminal SPIRE KIND. In addition, each WH2 domain of the SPIRE dimer is used to interact with an unbound actin monomer to facilitate actin nucleation. It is not verified but in the

following functional cooperation of SPIRE and FMN formins, the proline rich region of FMN FH1 could process profilin bound actin monomers to provide SPIRE WH2 domains with non-bound actin monomers for actin nucleation (indicated by the arrow). If FMN does not provide unbound actin monomers to the WH2 domains, the SPIRE dimer is mainly dependent on cytosolic unbound actin monomers. **(B)** After SPIRE mediated actin nucleation, the novel actin filament is released from WH2 domains and the dimerized donut shaped FH2 domains of FMN elongate the growing actin filament by processive addition of actin monomers. Actin monomers for the FH2 mediated elongation of the actin filament are provided by the FH1 domains, processing profilin bound actin monomers. The FSI domain is highlighted in *green* (modified from Kerkhoff, 2011).

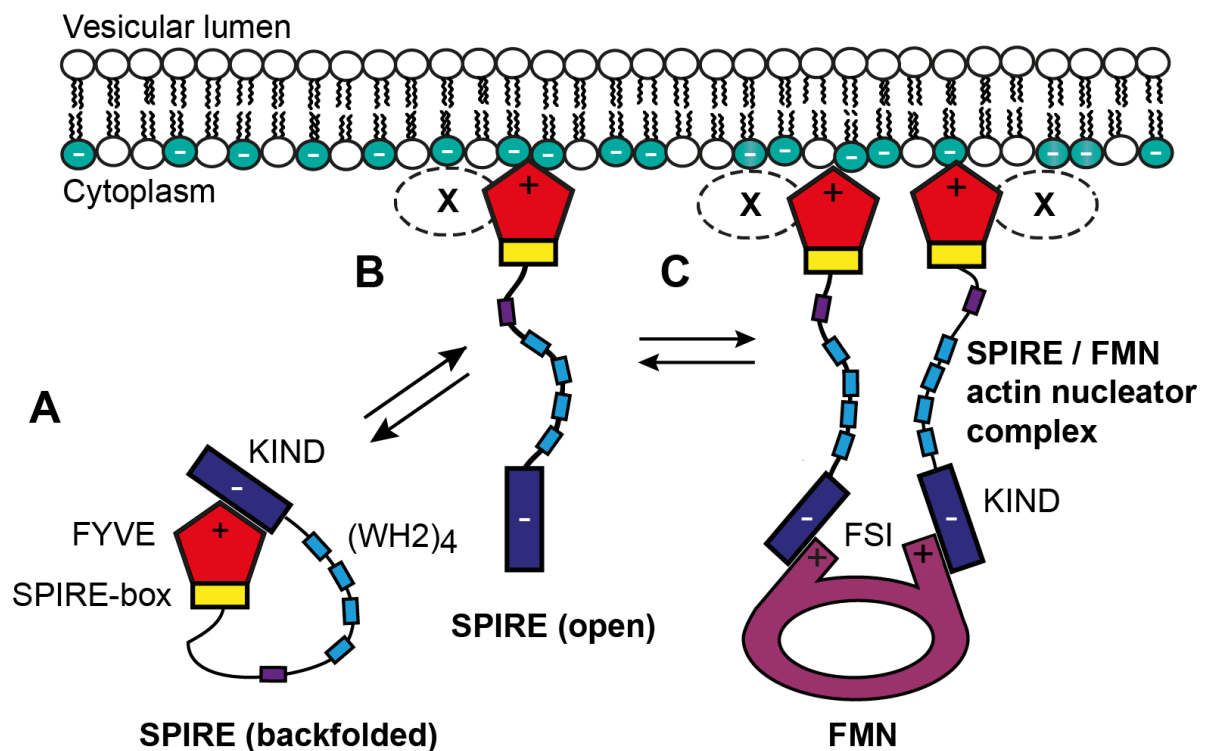


Figure 4 - Model for the different molecular states of the SPIRE / FMN actin nucleation complex at vesicle membranes. In this model cytosolic SPIRE proteins are primarily inactive (closed conformation) as backfolded monomers, but after transient membrane binding SPIRE proteins are activated (open conformation), able to dimerize and interact with FMN subfamily formins to build a functional unit as SPIRE / FMN actin nucleator complex. **(A)** The cytosolic backfolded SPIRE monomer is inactive due to interaction by FYVE / KIND with itself. The KIND is blocked by FYVE which is why the protein is not able to interact with FMN subfamily formins. **(B)** After transient interaction of the SPIRE C-terminus in a non-specific pattern with negatively charged intracellular membranes, the protein is unfolded. The accessible KIND is able to interact with FMN-FSI to initiate formation of a functional SPIRE / FMN actin nucleator complex. **(C)** A donut shaped FMN subfamily dimer interacts with two SPIRE proteins. The FMN subfamily formin and SPIRE build a functional unit to nucleate and elongate actin filaments. Additional factors (X) may specify targeting of SPIRE at vesicle membranes (modified from Tittel et al., 2015).

1.5 The SPIRE and myosin 5 interaction

Myosin actin motor proteins are molecular motors that are involved in a variety of cellular and sub-cellular mechanisms including cell migration and adhesion, muscle contraction, cytokinesis and signal transduction (Vicente-Manzanares et al., 2009; Hartman and Spudich, 2012). Furthermore, motor proteins are essential for intracellular transport of distinct cargos (Hartman and Spudich, 2012). In particular, neurons depend on these transport mechanisms as they synthesize most axonal and synaptic proteins in the cell body. These proteins need to be transported to their respective places of action for instance in large neurites and therefore, they require a molecular transport system (Hirokawa et al., 2010). In this context, myosin motors transport cargos along actin filaments, which facilitate a slow but precise transport system to subcellular target regions (Ross et al., 2008; Hirokawa et al., 2010; Welz et al., 2014).

Myosin superfamily motor proteins are actin binding ATPases. ATP hydrolysis induces an intramolecular conformational change within the motor. This conformational change is used to generate forces along actin filaments in order to induce morphological changes of cells, to mediate muscle contractions or to transport distinct cargos along actin tracks (Hartman and Spudich, 2012; Houdusse and Sweeney, 2016). Myosin motor proteins are divided into conventional myosins (myosin 2 family) and unconventional myosins (all other myosins; Venkatesh et al., 2019). To date, 38 different myosin genes have been identified in humans, which are grouped into distinct classes. In general, myosins consist of three different regions: An N-terminal motor domain, a neck region, and a tail region (Hammer and Sellers, 2011; Figure 5). The motor domain, which is also known as the head, harbors the ATPase activity and binds to actin filaments (Hammer and Sellers, 2011).

In the present thesis, myosin 5 motor proteins are of great interest because these motor proteins serve as cargo transporters (Hammer and Sellers, 2011). In humans, there are three different *myosin 5* genes: *myosin 5A*, *5B* and *5C*, encoding myosin 5A (MYO5A), myosin 5B (MYO5B) and myosin 5C (MYO5C) proteins, respectively (Mercer et al., 1991; Zhao et al., 1996; Berg et al., 2001; Rodriguez et al., 2002). In gene expression studies, *MYO5A*, *MYO5B* and *MYO5C* are found in the brain (Espreafico et al., 1992; Cheney et al., 1993; Rodriguez et al., 2002; Tilelli et al., 2003; Lisé et al., 2006). Myosin motor proteins like MYO5 assemble as a dimer to form a two-headed motor and work as a unit to allow the dimer to ‘walk’ along actin filaments (Hammer and Sellers, 2011). The neck region of MYO5 contains six IQ motifs and each IQ repeat binds to calmodulin or a related light chain (Espindola et al., 2000). As a consequence,

the MYO5 neck region builds the lever arm required for processive movement of the whole protein. In the case of MYO5, the tail region contains a proximal coiled coil domain to form a dimerization of heavy chains and a C-terminal globular tail domain (GTD). The GTD of MYO5 has an important role in cargo binding because it enables the motor protein to bind to adapter proteins, which mediate vesicle or organelle targeting (Wu et al., 1998; Reck-Peterson et al., 1999; Hammer and Sellers, 2011; Syamaladevi et al., 2012). In 2016, it was demonstrated that the GTDs of MYO5A, 5B and 5C, interact directly with an evolutionarily conserved sequence motif termed globular tail domain binding motif (GTBM) of the SPIRE actin nucleator. Through the interaction of MYO5 with RAB11, the SPIRE GTBM facilitates the formation of a tripartite complex at vesicle membranes made of SPIRE, MYO5 and RAB11. In summary, this complex could explain how RAB11 vesicles coordinate actin filament nucleation and myosin force generation at RAB11 vesicle membranes to regulate transport processes (Pylypenko, Welz, et al., 2016). Human homozygous mutation of MYO5A is known as Griscelli syndrome type 1, which is characterized by partial albinism and primary neurological defects (Thomas et al., 2009; Çağdaş et al., 2012). Mutations of MYO5B are also found in humans, and cause microvillus inclusion disease, a rare genetic disorder of the small intestine (Knowles et al., 2014).

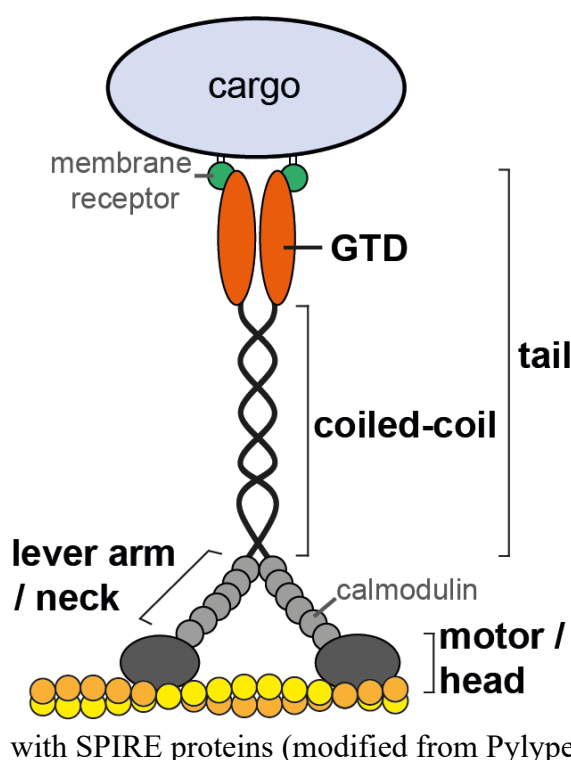


Figure 5 - Schematic overview of a vertebrate myosin 5 motor protein. The myosin 5 motor protein is organized into three different functional units, facilitating processive movement and consequently transport of cargos along actin filaments. The N-terminal motor domain provides ATPase activity and binds to actin filaments. The following lever arm / neck carries six calmodulin binding IQ motifs. Given the elongated nature of the neck region compared to other myosin motors the ATP hydrolysis induced conformational change is translated into a large step size of the motor which allows for processive movements. The C-terminal tail is divided into two functional and structural parts: the coiled-coil region necessary for dimerization of two myosin 5 heavy chains and at the very end of the protein the globular tail domain (GTD) which mediates as cargo binding domain cargo interaction of the motor and direct interaction with SPIRE proteins (modified from Pylypenko, Welz et al., 2016; Welz, 2018).

1.6 Cellular functions of SPIRE proteins

As mentioned previously, SPIRE proteins are expressed at very low levels but still have a significant impact on several cell biological mechanisms, including oocyte maturation, transport of RAB11 vesicles and peripheral transport of melanosomes in melanocytes (Pfender et al., 2011; Schuh et al., 2011; Pleiser, 2012; Alzahofi, Robinson, Welz et al., 2018; Kollmar, Welz, Straub et al., 2019). The ability of SPIRE to directly interact with FMN subfamily formins and MYO5 actin motors suggests a much wider spectrum of SPIRE function in vesicle and organelle transport (Pechlivanis et al., 2009; Pylypenko, Welz, et al., 2016). Further investigations are necessary to unravel the diversity of SPIRE functions.

1.6.1 SPIRE actin nucleators drive oocyte maturation

The maturation of oocytes into eggs is a complex differentiation program that is initiated early on in embryonic development. During early meiosis, the diploid precursor cells termed ‘oocytes’ are arrested at prophase I and wait for their chance to mature into pregnable eggs. During sexual maturity, mostly a single oocyte per menstrual cycle matures into a haploid egg and becomes ovulated from its surrounding follicle. The maturation of an oocyte into an egg is dependent on asymmetric cell division, including a reduction to half of the oocyte chromosomes (Mogessie et al., 2018). The process of asymmetric meiotic cell division can be described by two different stages. In the first stage, an asymmetric positioning of the meiotic spindle takes place in order to move excessive chromosomes for a haploid egg into a small cell termed the polar body. In this context, the dense chromosomes must first be aligned to the spindle apparatus, which is necessary to separate chromosomes in space (Kirschner et al., 1986; Kline-Smith et al., 2004). After chromosomes are aligned to the spindle, the whole spindle has to be moved to the cell cortex to initiate the second stage of asymmetric cell division. Spindle positioning is dependent on a dynamic actin meshwork, which is generated by FMN2 and SPIRE actin nucleators (Leader et al., 2002; Dumont et al., 2007; Pfender et al. 2011). For that matter, SPIRE and FMN interact as a functional unit in which both actin nucleators depend on each other. Interestingly, a single depletion of either SPIRE1 or SPIRE2 compared to a double depletion does not affect spindle positioning, indicating that the protein similarity allows a mutual rescue of both proteins. Finally, the extrusion of polar bodies describes the second stage of the asymmetric meiotic division. A loss of SPIRE proteins not only inhibits proper spindle positioning, but consequently impairs polar body extrusion as well. In summary, SPIRE proteins are important for flawless oocyte maturation (Pfender et al., 2011). Interestingly the

corresponding *Drosophila melanogaster* (Dm) SPIRE and Cappuccino (a Dm FMN2 ortholog) produce a similar actin meshwork in fly oocytes, which is necessary to facilitate the maturation of the oocyte into an egg (Dahlgaard et al., 2007). Errors in the maturation of oocytes may result in aneuploidy, hypofertility, and genetic disorders in offspring (Leader et al., 2002; Zhai et al., 2018).

1.6.2 SPIRE actin nucleators drive vesicular transport processes

Intracellular transport of cargo and organelles is essential for communication, organization and polarity of mammalian cells (Pylypenko, Welz et al., 2016). In this respect, cargo, such as proteins, lipids, or even RNA molecules, have to be transported to their target areas, and especially proteins are therefore wrapped into membrane enclosed carriers termed vesicles. Transport of intracellular cargo is generally mediated by microtubules and actin filaments. Polarized microtubules serve as long bidirectional transport tracks and provide a fast but constricted path used by kinesin and dynein motor proteins (Schliwa and Woehlke, 2003; Hirokawa et al., 2009; Welz et al., 2014). Actin filament-based transport processes are much slower but more dynamic than microtubule-based transports and are mostly important for precise short-range movements of vesicles, facilitated by myosin motor proteins (Hirokawa et al., 2009; Kneussel and Wagner, 2013; Welz et al., 2014). Typical intracellular transport processes including microtubule- and actin-based transport systems for cargo are commonly described as the *highways and local roads* model (Figure 6). In this controversial discussed model, vesicles are transported quickly along microtubules to the cell periphery. Here, vesicles are detached from microtubules and begin to move slowly along actin filaments to their final destinations (Langford, 1995; Ross et al., 2008; Woolner and Bemet, 2009; Welz et al., 2014). The dynamic actin cytoskeleton facilitates transport of vesicles to areas which are not reached and therefore supplied with cargos by the coarse microtubule network (Welz et al., 2014). Already in 2001, it was found that the actin nucleator SPIRE is targeted to intracellular membranes and involved in vesicle transport processes (Kerkhoff et al., 2001). Years later, in mouse metaphase oocytes, SPIRE was identified to contribute to a microtubule-independent long-range transport of RAB11 vesicles (Schuh et al., 2011). In this context, SPIRE and FMN proteins cooperate in nucleating actin filaments originating from vesicle membranes to facilitate the formation of a cytoplasmic actin mesh and to allow a myosin 5B (MYO5B)-dependent RAB11 vesicle transport. A lack of SPIRE1 and SPIRE2 results in a loss of directed transport of RAB11 vesicles to the oocyte cortex (Schuh et al., 2011). SPIRE

function in oocytes therefore presents two interesting facts: SPIRE can be necessary for the movement of vesicles, and actin filaments are used as alternative routes for distinct long-range transport processes.

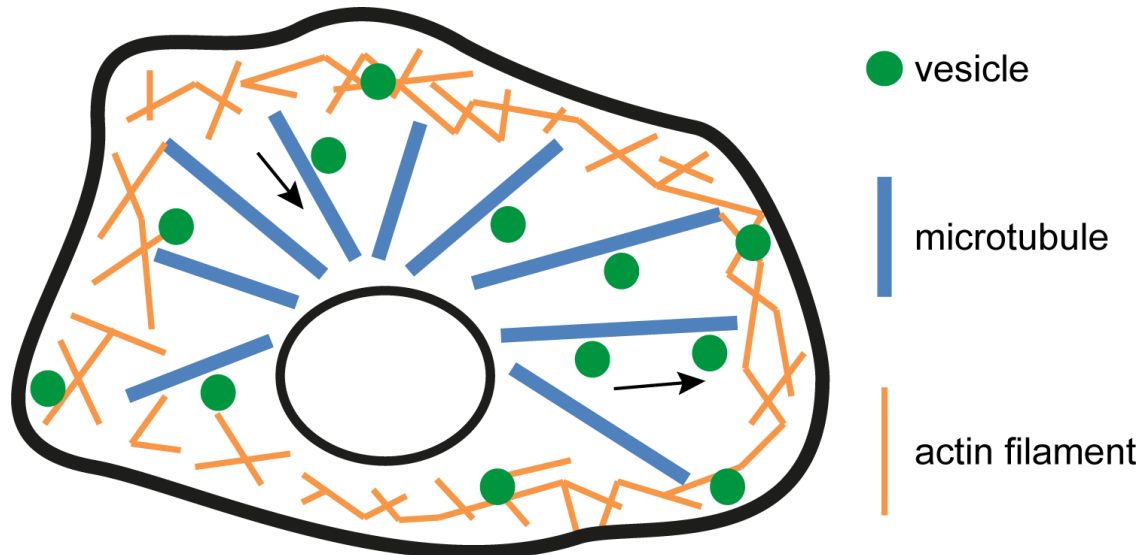


Figure 6 - Schematic overview of the *highways and local roads* model for intracellular transport. Microtubules serve as fast transport tracks for cargo and organize a coarse transport structure, which enables a bidirectional transport of cargos between the center and the periphery of the cell. The more dynamic actin cytoskeleton localizes in more cortical areas of the cell and facilitates a slower but more precise transport system of cargos to subcellular target regions, which are not connected to the microtubule tracks. In this model, vesicles are first transported from the cell center to the periphery along microtubules (*highways*) and then the slower, but dynamic actin filament system (*local roads*) take over the transportation of the cargo to its specific target site (modified from Ross et al., 2008; Welz et al., 2014; Welz, 2018).

1.6.3 SPIRE1 / FMN1 / MYO5A cooperate in cytoplasmic melanosome dispersion

Melanosomes produce, store and transport the natural pigment melanin required for tissue coloration and photoprotection. In mammals, melanosomes are synthesized in skin-located melanocytes, choroidal melanocytes and retinal pigment epithelial cells (RPE cells), which supply surrounding tissues with an adequate number of melanosomes (Wasmeier et al., 2008). In general, the transport and release of melanosomes into distinct tissues provide the melanosome receiving cells with the photoprotective and dark-colored melanin. As a consequence, melanin colors mammalian skin, hair and eyes. In addition, the pigment prevents cellular DNA damages caused by ultraviolet irradiation (Raposo and Marks, 2007; Wasmeier et al., 2008; D'Orazio et al., 2013). Consequently, a loss of melanosome function is associated with albinism and is linked to the pathogenesis of skin melanoma (Wasmeier et al., 2008; Oberhofer et al., 2017).

Skin melanocytes distribute melanosomes via dendrites to provide keratinocytes with an adequate amount of melanin. In this process, the intra- and intercellular transport mechanisms of melanosomes play an important role in facilitating melanin supply to a specific area (Alzahofi, Robinson, Welz et al., 2018). In the 1990s, it was described that melanosomes are transported along microtubules and actin filaments, but only the actin-based transport mechanism was investigated in more detail (Wei et al., 1997; Wu et al., 1997). In this context, an old model hypothesized that melanosomes are transported in a fast microtubule-dependent long-range distance transport to the tip of melanocyte dendrites where they are captured by a MYO5-based mechanism at actin filaments (Wu et al., 1998).

In dendrites of melanocytes, the intracellular melanosome transport along actin filaments is facilitated by a tripartite complex containing RAB27A, melanophilin (MLPH) and MYO5A. The melanosome bound RAB27A associates with MLPH, which acts as an adapter between RAB27A and MYO5A to finally target MYO5A towards melanosomes (Hume et al., 2001; Matesic et al., 2001; Wu et al., 2001; Fukuda et al., 2002; Hume et al., 2002; Nagashima et al., 2002; Provance et al., 2002; Wu et al., 2002; Oberhofer et al., 2017). In the old melanosome transport model, the tripartite complex therefore facilitates the association of melanosomes to actin filaments in dendrites of melanocytes, enables the detachment of melanosomes from microtubules, and facilitates positioning of melanosomes close to the plasma membrane. The tripartite complex is therefore required for the retention of melanosomes in the dendrites of skin melanocytes (Wasmeier et al., 2008). In RPE cells, transport of melanosomes along actin filaments is organized by a tripartite complex containing RAB27A, the myosin- and RAB-interacting protein MYRIP and MYO7A. This complex is similar to the RAB27A / MLPH / MYO5A tripartite complex of skin melanosomes and appears to perform the same function in RPE cells as its corresponding complex at skin cell melanosomes (Lopes et al., 2007; Ramalho et al., 2009).

In contrast to the intracellular melanosome transport system described herein, a recent study revealed that the distribution of melanosomes seems to be determined by the balance of two different mechanisms: An actin dependent long-range dispersion and a microtubule based perinuclear clustering, but not peripheral dispersion of melanosomes (Alzahofi, Robinson, Welz et al., 2018). It was previously shown in 2014 that microtubule depletion by nocodazole had little effect on pigment distribution, while disruption of the actin cytoskeleton by latrunculin A resulted in significant perinuclear clustering of melanosomes (Evans et al., 2014). In the recently published model, the small GTPase RAB27A recruits SPIRE1 to melanosomes

and the actin nucleator cooperates in a complex with FMN1 organizing a melanosome-originated actin meshwork to drive MYO5A dependent peripheral melanosome transport in mouse melanocytes. A lack of FMN1 or SPIRE leads to the loss of peripheral melanosome dispersion in melanocytes, and results in a perinuclear clustering of melanosomes (Alzahofi, Robinson, Welz et al., 2018). The experiments of the recent publication indicate that SPIRE1 / FMN1 / RAB27A are important to produce a dynamic actin meshwork for melanosome transport, while the tripartite complex of RAB27A / MLPH / MYO5A uses the actin meshwork to transport melanosomes (Figure 7). In addition to mouse oocytes, the publication also shows a long-range transport mechanism along dynamic actin filaments mediated by SPIRE / FMN-nucleated actin filaments (Alzahofi, Robinson, Welz et al., 2018).

The importance of the RAB27A / MLPH / MYO5A complex is underscored by the fact that gene mutations within any member of the complex result in a rare disease - the Griscelli syndrome (GS). The autosomal recessive hereditary GS is classified into three different subtypes, of which GS type 3 represents the mildest form of the disease. All known patients suffering from any subtype of GS have hypopigmentation of skin and hair (characteristically silvery gray hair), and show a perinuclear accumulation of melanosomes in melanocytes, caused by a transport failure of melanosomes (Huizing et al., 2008; van Gele et al., 2009). GS type 1 is caused by specific mutations in the *MYO5A* gene and patients show severe impairments of brain function, primary neurological symptoms and hypopigmentation. In contrast, GS type 2 is associated with immune system abnormalities in addition to hypopigmentation, but is not associated with brain dysfunctions. Mild GS type 3 patients only show hypopigmentation of skin and hair (Huizing et al., 2008).

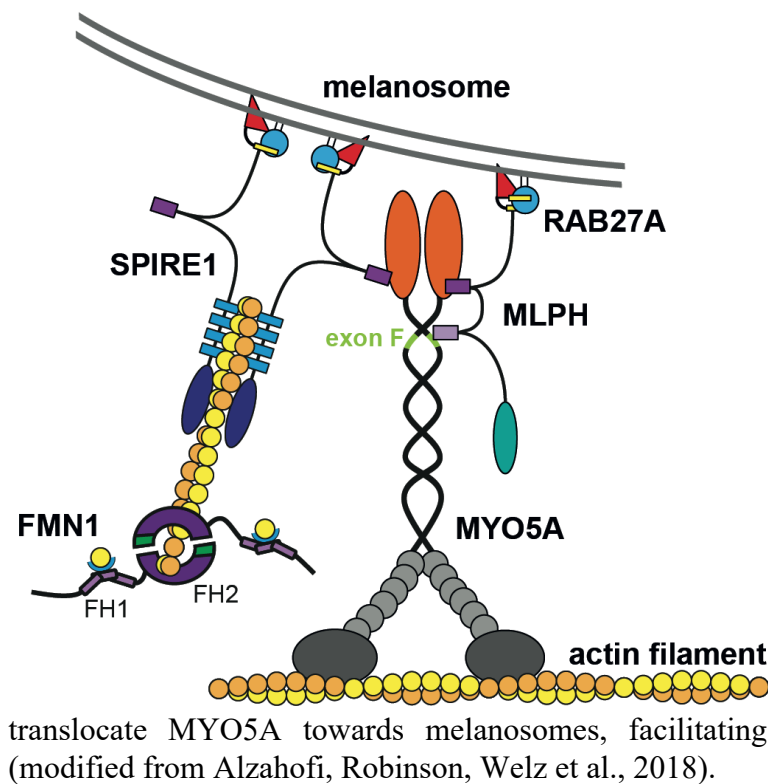


Figure 7 - Model how RAB27A could regulate actin filament driven melanosome transport in melanocytes by recruiting SPIRE1 / FMN1 and MLPH / MYO5A towards melanosomes. In this model RAB27A recruits SPIRE1 / FMN1 and MLPH / MYO5A to melanosomes. The SPIRE1 / FMN1 / RAB27A complex is important to produce a dynamic actin meshwork for melanosome transport, while the tripartite complex of RAB27A / MLPH / MYO5A uses the actin meshwork to ultimately transport melanosomes. In this context, SPIRE1 and MLPH proteins recruited by RAB27A could transport along actin filaments

1.7 Knockout mouse models of the actin nucleators SPIRE and FMN subgroup formins

The low expression levels of the actin nucleators SPIRE and FMN subgroup formins make it complicated to investigate the intracellular functions of these proteins at endogenous levels. In order to explain the cell biological mechanisms to which the proteins contribute, mouse models have been established.

1.7.1 The *SPIRE1* mutant mouse

To gain a deeper insight into the cellular functions of the SPIRE1 protein, a mutant mouse model lacking the expression of any functional *SPIRE1* protein was generated. A DNA gene-trap insertion following the fifth exon inhibits the translation of the *SPIRE1* mRNA immediately after N-terminal SPIRE1 KIND. As a result, the expression of all three *SPIRE1* isoforms is abolished, i.e. neither a functional SPIRE1 nor SPIRE1-E9 nor mitoSPIRE1 protein is synthesized. The N-terminal SPIRE1 domain of *SPIRE1* mutant mice can be translated as a single truncated protein containing a functional KIND. In this context, the presence of the single KIND domain could influence SPIRE / FMN interaction in a dominant negative effect (Pleiser

et al., 2014). However, SPIRE2 protein expression is not affected by the *SPIRE1* inserted gene-trap, because the *SPIRE2* gene locus is located on a different chromosome (Pleiser et al., 2014; Kollmar, Welz, Straub et al., 2019). SPIRE proteins affect the spindle positioning and polar body extrusion of maturing oocytes and therefore their maturation into eggs (Pfender et al., 2011). The redundant function of SPIRE2 is sufficient to compensate SPIRE1 functions for oocyte maturation that *SPIRE1* mutant mice are still fertile (Pleiser et al., 2014). Interestingly, *SPIRE1* mutant mice do not show any anatomical abnormalities. However, on a cellular level, cortical neurons of *SPIRE1* mutant mice show a reduced number of dendritic spines. Phenotyping of *SPIRE1* mutant mice revealed an increased fear expression in contextual and cued fear conditioning experiments of male mice. The fear expression phenotype indicates a highly specific function of proteins expressed from the *SPIRE1* gene in fear learning (Pleiser et al., 2014). A human correlate to the *SPIRE1* mutant mouse model with a functional loss of *SPIRE1* or *SPIRE2* has not yet been discovered.

1.7.2 The FMN1 knockout mouse

In 2009, a mouse model lacking the expression of functional FMN1 proteins was established - the FMN1^{Pro} mouse model. The FMN1^{Pro} mouse has a genetic disruption at the proline-rich FH1 domain of FMN1, which is why these mice fail to synthesize any full-length FMN1 proteins. The loss of functional FMN1 splice variants causes kidney aplasia and limb development defects (oligodactyly phenotype) in mice, but FMN1^{Pro} mice are still viable and fertile (Zhou et al., 2009). Until now the FMN1^{Pro} mouse model has not been characterized in fear conditioning experiments.

1.7.3 The FMN2 knockout mouse

In 2002, a knockout mouse model for the SPIRE interacting FMN2 was established. The knockout mice neither show abnormalities of anatomic structures nor obvious defects in the central nervous system. Nevertheless, metaphase I oocytes of female FMN2 knockout mice fail in spindle positioning and polar body extrusion. As a consequence, female FMN2 knockout mice are hypo-fertile and fertilization of FMN2 knockout oocytes results in a polyploid embryo formation. In contrast fertility of male knockout animals is not affected by the absence of FMN2 (Leader et al., 2002; Dumont et al., 2007). A more recent study shows that the absence of FMN2 causes a reduced number of dendritic spines in neuronal cells (Law et al., 2014). In addition,

the loss of FMN2 induces mild deficits in neuronal plasticity (Agís-Balboa et al., 2017). Phenotyping of these knockout mice revealed an impairment of fear extinction and an age dependent loss of fear memory (Peleg et al., 2010; Agís-Balboa et al., 2017).

1.8 Mutations of the human FMN2 protein

As the maturation of mouse oocytes is dependent on FMN2 function, it might be obvious that the fertility of women is also affected by defects of the FMN2 protein. For this reason, a study analyzed the *FMN2* gene for women with unexplained infertility. Only six patients with unexplained infertility were investigated, but none of these patients showed an abnormality in the *FMN2* gene. To figure out if FMN2 also affects human fertility, women with unexplained infertility and meiosis I arrest of oocytes, as shown for the FMN2 knockout mouse, have to be analyzed for FMN2 mutations (Ryley et al., 2005).

Homozygous FMN2 truncations in two independent and consanguineous families show offsprings with an intellectual disability (ID). An ID is defined by cognitive deficits, which means an IQ lower than 70, and limitations in adaptive behavior. One consanguineous family originates from Pakistan and the other one from Egypt. The healthy Pakistani parents have 6 offspring, three of which are affected by ID. On the other hand, two of the six children of the healthy Egyptian parents are affected. All individuals affected by ID, regardless of which family they're from, harbored a homozygous frameshift mutation in the *FMN2* gene, which suggests a recessive inheritance. Fibroblasts from an affected individual and a non-affected littermate were reprogrammed to neuronal cells and the synaptic density was determined. Synaptic density in diseased cells was nearly reduced by half in comparison to the healthy control (Law et al., 2014). The culmination of these studies demonstrates the importance of the actin nucleator FMN2 for neuronal systems.

1.9 Aim of the thesis

This thesis aims to explain on a molecular level the increased fear-related behavior in contextual and cued fear conditioning experiments of *SPIRE1* mutant mice, lacking the expression of any functional SPIRE proteins from the *SPIRE1* gene.

SPIRE actin nucleators organize local actin / myosin networks at vesicle membranes, which mediate the cortical transport of RAB11 vesicles in oocytes and the cytoplasmic dispersion of

melanosomes (Schuh et al., 2011; Alzahofi, Robinson, Welz et al., 2018). In this context, mitochondrial motility seems to be influenced by actin-associated myosin motor proteins and actin filaments (Hollenbeck and Saxton, 2005; Pathak et al., 2010; Gutnick et al., 2019). Recently, the mitochondrial targeting of a splice variant of the *SPIRE1* actin nucleator was discovered and the corresponding protein was named ‘mitoSPIRE1’ (Manor et al., 2015). The localization of mitoSPIRE1 is most likely unique to SPIRE proteins, and might therefore not be compensated by SPIRE2 proteins expressed from the *SPIRE2* gene. Knowledge of the intracellular expression and function of mitoSPIRE1 could help to interpret the fear conditioning phenotype of *SPIRE1* mutant mice.

Accordingly, the work presented here addresses the expression, localization and the specific function of the mouse mitoSPIRE1 protein. As a basic tool to differentiate the mitochondrial from vesicular SPIRE1 functions, a mitoSPIRE1 knockout mouse has been generated. Following the hypothesis that mitoSPIRE1, in analogy to its vesicular homologs, organizes actin / myosin networks at mitochondria membranes, I have analyzed if mitoSPIRE1 influences mitochondrial morphology, function and motility. Overall these studies provide basic cell biological knowledge to resolve the function of *SPIRE1* in fear learning. Based on the theory that mitoSPIRE1 influences fear behavior, it is indispensable to understand the molecular function of mitoSPIRE1, which could potentially be used in the future as a medical treatment for patients suffering from anxiety disorders.

2. Materials and methods

Parts of the materials and methods section were already published in Alzahofi, Robinson, Welz et al., 2018 and in Kollmar, Welz, Straub et al., 2019. These materials and methods sections are written by myself and generated for the mentioned publications and my dissertation.

2.1 Primer design

Primer pairs for polymerase chain reaction (PCR) and quantitative real-time PCR (qPCR) to amplify specific genomic DNA and cDNA sequences were designed using the web-based tool Primer3 (<http://primer3.ut.ee>). The sequence specificity of each primer pair was checked by performing a Primer-BLAST search against the genomic DNA database (www.ncbi.nlm.nih.gov/blast). Primer oligonucleotides consist of 18 to 30 nucleotides and have a GC content of 40 - 60 %. qPCR primer pairs were chosen to amplify exon specific sequences less than 150 base pairs and flank a region that contains at least one intron. PCR primer pairs were mostly chosen to amplify fragments less than 1000 base pairs. All primers were synthesized by Sigma-Aldrich (St. Louis, USA) and purified by HPLC. Lyophilized primers were resuspended in DEPC-H₂O and stored at -20 °C. Prior to use in qPCR all primers were tested to amplify a specific band in PCR and agarose gel separation (method written as presented in Kollmar, Welz, Straub et al., 2019).

2.2 Agarose gel electrophoresis

Agarose gel electrophoresis was used to visualize the fragment lengths of amplified PCR products or digested vectors and DNA inserts. By heating and shaking a specific amount of ultrapure agarose (Thermo Fisher Scientific Inc. (ThermoFisher), Waltham, USA) was solved in 0.5x TBE buffer. For subsequent visualization of DNA in UV light 10 mg/ml ethidiumbromide (Carl Roth, Karlsruhe, Germany) was added to the hot mixture and the mixture was finally poured into a sealed gel casting tray. Here we generated agarose gels with an agarose concentration between 1 % (used for separation of DNA fragments longer than 1000 bp) and 2.5 % (used for separation of DNA fragments shorter than 1000 bp). DNA samples were mixed with 6x DNA loading dye, filled into gel pockets of the agarose gel and separated at 120 V for 30 min in 0.5x TBE buffer. As a molecular length marker one pocket of each gel was loaded with a 1 kb or 100 bp (ThermoFisher) -standard, which allows the identification of DNA samples in size by comparison with the utilized size standard.

2.3 Agarose gel clean-up

For further processing of DNA fragments, which are separated by fragment length in an agarose gel, electrophoresis DNA bands were extracted from the agarose gel and purified with the NucleoSpin Gel and PCR Clean-up kit (Macherey-Nagel, Düren, Germany). The kit was used according to the manufacturer's protocol. In general, the kit is based on the binding of DNA to a silica membrane, followed by multiple washing steps and finally DNA is eluted with 30 µl elution buffer (5 mM Tris-HCl, pH 8.5). The concentration and purity of extracted DNA was analyzed by spectrophotometric analysis.

2.4 RNA isolation

2.4.1 RNA isolation of mouse organs

Male C57BL/6J mice were ordered from Charles River Laboratories (Sulzfeld, Germany) at an age of 6 weeks. Immediately after arrival mice were killed by cervical dislocation and organs of interest were isolated. Organs were weighted and stored in an adequate amount of *RNA later* (Qiagen, Hilden, Germany) at 4 °C, which inhibits RNA degradation. For total RNA preparations of organs, the RNeasy Midi Kit (Qiagen) was used according to manufacturer's recommendation. Disruption and homogenization of organs was done with the TissueRuptor (Qiagen). Isolated RNA was stored in the freezer at -20 °C (method written as presented in Kollmar, Welz, Straub et al., 2019).

2.4.2 Total RNA isolation from eukaryotic cultured cells

Mammalian cells were cultured until they are 80 - 90 % confluent. Total RNA from cells of interest was isolated according to the manufacturer's protocol of the NucleoSpin RNA Kit from Macherey-Nagel. Following the protocol genomic DNA is eliminated and RNA is isolated by binding to a silica membrane. After isolation the amount and purity of total RNA was directly determined by spectrophotometric analysis. Isolated RNA was stored in the freezer at -20 °C.

2.4.3 Analysis of RNA / DNA purity and concentration

In order to determine the yield and purity of isolated RNA spectrophotometric analysis by a Nanophotometer[®] (Implen GmbH, Munich, Germany) spectrophotometer was done. Nucleic acid concentration measurements in the Nanophotometer[®] are based on absorbance at a

wavelength of 260 nm. A volume of 1 µl isolated total RNA was used to determine RNA concentration as well as purity and measured in triplicates per sample. 260/280 absorbance ratio was obtained and used in assessment of sample purity. In this context a value of ~ 1.8 describes pure DNA and a value of ~ 2.0 indicates pure RNA. In this thesis only isolated total RNA and DNA with a high purity were used.

2.4.4 RNA quality

Sample integrity of isolated total RNA from mouse organs was measured with the QIAxcel (Qiagen) using the QIAxcel RNA QC Kit v2.0 (Qiagen) according to the manufacturer's protocol. For each organ the quality of isolated total RNA from a single organ was determined vicariously for all isolated organs from the same type. QIAxcel instruments determine the RNA Integrity Score by capillary gel electrophoresis of nucleic acids, which allows interpretation of sample integrity. In this context the highest RNA Integrity Score of 10 describes a completely intact RNA, whereas the lowest RNA Integrity Score of 1 indicates a high degradation of the RNA sample. An RNA Integrity Score above 6 still indicates a high quality of RNA, why in this thesis isolated total RNAs were only used if they have an RNA Integrity Score higher than 6.

2.5 PCR techniques

The belonging sections (2.5.2 - 2.5.4) of the chapter 'PCR techniques' are written as described in standard protocols of the Kerkhoff laboratory and as presented in Welz, 2018.

2.5.1 Reverse transcription (synthesis of cDNA)

Using isolated total RNA as template cDNA was generated by reverse transcription employing the QuantiNova Reverse Transcription Kit (Qiagen) according to the manufacturer's protocol. In this method, the ability of the enzyme reverse transcriptase enables the synthesis of DNA from an RNA template. The QuantiNova Reverse Transcription Kit includes a genomic DNA removal step, which excludes the abundance of false positive cDNA fragments made from genomic DNA. For cDNA used in qPCR we used an internal control RNA provided by the kit to verify successful and efficient reverse transcription. After successful cDNA generation, cDNA was used for PCR and qPCR and stored in -20 °C.

2.5.2 Amplification of cDNA fragments

Standard qualitative PCR amplification of cDNA fragments was performed to check for general gene expression from specific mouse tissues or cultured cells. PCR was done in 200 μ l PCR-SoftTubes (Biozym Scientific GmbH, Hessisch Oldendorf, Germany) using Q5 High-Fidelity DNA Polymerase (New England Biolabs (NEB), Frankfurt am Main, Germany) employing 50 - 200 ng cDNA or 1 ng plasmid DNA as a control. In addition, 10 mM of each dNTP, the Mg^{2+} containing Q5 Reaction Buffer, 10 μ M of the reverse and forward primer, and upon need the GC Enhancer (all from NEB), which enables better amplification of GC-rich sequences, were mixed and added gently to the PCR reaction tube. For each PCR the elongation time for DNA synthesis (t_E) was calculated individually for the length of the amplified fragment (30 sec per 1000 bp) and extension temperature was set to 72 $^{\circ}C$. The primer annealing temperature (T_A) was set 5 $^{\circ}C$ lower than the primers melting temperature (T_m) of the lower primer T_m . To generate a sufficient product yield 30 - 35 amplification cycles were used. The specific length of PCR products was analyzed by agarose gel electrophoresis. The cycling protocol is shown in Table 1.

(i)

Reagent	Volume
5X Q5 Reaction Buffer	5 μ l
10 mM dNTPs (each)	0.5 μ l
10 μ M forward primer	1.25 μ l
10 μ M reverse primer	1.25 μ l
template cDNA	50 - 200 ng
Q5 DNA Polymerase	0.25 μ l
(5X Q5 High GC Enhancer)	(5 μ l)
nuclease-free water	to 25 μ l
total	25 μl

(ii)

Step	Temperature	Time	
Initial Denaturation	98 °C	30 sec	
Denaturation	98 °C	8 sec	
Annealing			
Extension			
	30 - 35 cycles	50 - 72 °C (T_A)	25 sec
		72 °C	30 sec/kb (t_E)
Final Extension	72 °C	120 sec	
Storage	4 °C	hold	

Table 1 - Protocol for routine PCR using defined components (i) and thermocycling conditions (ii) for DNA fragment amplification by Q5 High-Fidelity DNA Polymerase. Annealing temperature (T_A) = 5 °C less than melting temperature (T_m) of the lower T_m from used primer pair. Elongation time (t_E) = 30 sec for 1000 bp.

2.5.3 Amplification of genomic DNA fragments (genotyping of mice)

General PCR amplification was performed in 200 μ l PCR-SoftTubes (Biozym Scientific GmbH) using up to 50 ng template DNA mixed with Taq DNA Polymerase (NEB) and Standard Taq Buffer (NEB). This method was used besides others to genotype wild type, *SPIRE1* mutant and mitoSPIRE1 knockout mice. For each PCR the elongation time for DNA synthesis (t_E) was calculated individually for the length of the amplified fragment (60 sec per 1000 bp) and extension temperature was set to 72 °C. The primer annealing temperature (T_A) was set 5 °C lower than the primers melting temperature (T_m) of the lower primer T_m . For generation of a sufficient product yield 35 amplification cycles were used. The specific length of PCR products was analyzed by agarose gel electrophoresis. The cycling protocol is shown in Table 2.

(i)

Reagent	Volume
template DNA	0.1 - 50 ng
25 mM dNTPs (each)	0.3 μ l
10 μ M forward primer	0.3 μ l
10 μ M reverse primer	0.3 μ l
Standard Taq Buffer	3 μ l
Taq DNA Polymerase	0.3 μ l
nuclease-free water	to 30 μ l
total	30 μl

(ii)

Step	Temperature	Time	
Initial Denaturation	95 °C	180 sec	
Denaturation	95 °C	20 sec	
Annealing			
Extension			
	35 cycles	T_A °C	30 sec
	68 °C	60 sec/kb (t_E)	
Final Extension	68 °C	300 sec	
Storage	4 °C	hold	

Table 2 - Protocol for routine PCR using defined components (i) and thermocycling conditions (ii) for DNA fragment amplification by Taq DNA Polymerase. Annealing temperature (T_A) = 5 °C less than melting temperature (T_m) of the lower T_m from used primer pair. Elongation time (t_E) = 60 sec for 1000 bp.

2.5.4 Amplification of cDNA fragments for cloning

DNA fragment amplification for cloning was performed in 200 μ l PCR-SoftTubes (NEB) using 50 ng template DNA (plasmid DNA) and the Pfx DNA Polymerase (ThermoFisher). For each PCR the elongation time for DNA synthesis (t_E) was calculated individually for the length of the amplified fragment (60 sec per 1000 bp) and extension temperature was set to 68 °C. The primer annealing temperature (T_A) was set 5 °C lower than the primers melting temperature (T_m) of the lower primer T_m . For generation of a sufficient product yield 35 amplification cycles were used. The cycling protocol is shown in Table 3.

(i)

Reagent	Volume
template DNA	50 ng
10 μ M forward primer	3 μ l
10 μ M reverse primer	3 μ l
10X Pfx Buffer	5 μ l
Pfx DNA Polymerase	1 μ l
nuclease-free water	to 50 μ l
total	50 μl

(ii)

Step	Temperature	Time
Initial Denaturation	95 °C	300 sec
Denaturation	95 °C	60 sec
Annealing		
Extension		
	35 cycles	30 sec
	68 °C	60 sec/kb (t_E)
Final Extension	68 °C	300 sec
Storage	4 °C	hold

Table 3 - Protocol for routine PCR using defined components (i) and thermocycling conditions (ii) for DNA fragment amplification by Pfx DNA Polymerase. Annealing temperature (T_A) = 5 °C less than melting temperature (T_m) of the lower T_m from used primer pair. Elongation time (t_E) = 60 sec for 1000 bp.

2.5.5 Quantitative real-time PCR

Expression vectors encoding mouse *SPIRE1*, *SPIRE1-E9*, *mitoSPIRE1* and *SPIRE2* cDNAs (see Table 18) were used as positive controls. The absolute gene quantification by quantitative real-time PCR (qPCR) was performed with the Rotor-Gene Q thermocycler (Qiagen) and the QuantiNova SYBR Green PCR Kit (Qiagen). Each reaction was set up in triplicates and cycle threshold (C_T) values were calculated by the Qiagen Rotor-Gene Q Series Software. Reactions were pipetted with Filter pipette tips (Sarstedt, Nümbrecht, Germany; and Greiner Bio-One, Frickenhausen, Germany). For absolute quantification of sample mRNA copy numbers specific expression vectors encoding mouse *SPIRE1*, *SPIRE1-E9*, *mitoSPIRE1* and *SPIRE2* cDNAs (see Table 18) were used to generate a standard curve with known copy number concentrations. Therefore, plasmid DNA was linearized by restriction digest and then serially diluted in water. The copy number of standard DNA molecules was then determined by the following formula (from the script ‘Critical Factors for Successful Real Time PCR’, Qiagen):

$$\left(\frac{X \frac{\text{g}}{\mu\text{l}} \text{ DNA}}{[\text{plasmid length in basepairs} \times 660]} \right) \times 6.022 \times 10^{23} = Y \frac{\text{molecules}}{\mu\text{l}}$$

C_T values of the samples were compared to those of the standard curve with known concentrations to calculate the sample mRNA copy numbers. The primer pairs used for quantitative PCRs are shown in Table 15. The primer pair for ‘*SPIRE1*’ amplifies all three splice variants from the *SPIRE1* gene whereas the primer pairs for ‘*SPIRE1-E9*’ and ‘*mitoSPIRE1*’ are specific for the distinct splice variant. To determine the exact copy number of *SPIRE1* mRNA, the calculated copy numbers of *SPIRE1-E9* and *mitoSPIRE1* were subtracted from the calculated total *SPIRE1* copy number (method written as presented in Kollmar, Welz, Straub et al., 2019).

2.6 Cloning

Most of the used DNA constructs (plasmids with specific DNA inserts) in the present thesis were generated by Annette Samol-Wolf and Dr. Tobias Welz from the Kerkhoff laboratory (see Figure 9, 10). In the following chapter the general procedure for cloning is described as it is performed in the Kerkhoff laboratory. Point mutants were generated using the In-Fusion HD cloning kit (TakaraBio, Kusatsu, Japan). The belonging sections (2.6.1 - 2.6.4) of the chapter ‘Cloning’ are written as described in standard protocols of the Kerkhoff laboratory and as presented in Welz, 2018.

2.6.1 Restriction digest and ligation of DNA vectors

A commercial DNA vector (plasmid) like pAcGFP1-C1 (Clontech, Kusatsu, Japan) have been chosen to finally integrate a DNA fragment of interest. For successful integration of a novel DNA fragment 2 μ g of plasmid DNA was first digested with specific restriction endonucleases (NEB) in the appropriate buffer for 2 hours at 37 °C. In general, a combination of two restriction endonucleases was chosen, each cutting the plasmid only once, resulting in a truncated vector and a belonging inlay. Therefore, the digested plasmid shows two DNA bands in agarose gel electrophoresis - a digested vector and the cut insert. Indeed, the cut insert has mostly only a few bp why it is hard to see it in the agarose gel. As a conformation for successful plasmid digestion two controls were used: an undigested vector and a vector which was only digested with one of the two restriction endonucleases. Calf Intestinal Alkaline Phosphatase (CIP; NEB) removes the phosphate groups at the 5’ ends of DNA and inhibits therefore the religation of the digested plasmid, why CIP was added 60 and 90 min after the start of the restriction digest. The DNA fragment of interest was amplified by PCR, separated by agarose gel electrophoresis,

purified and finally digested with identical restriction endonucleases (NEB) as the plasmid. After separation by gel electrophoresis and DNA purification a ligation from the digested plasmid and the digested DNA fragment of interest was performed using T4 DNA Ligase (NEB) at 16 °C over night.

2.6.2 Transformation of Escherichia coli bacterial cells

For amplification of newly generated DNA plasmids the chemo-competent NEB10-beta competent *E. coli* ($\Delta(ara-leu)$ 7697 *araD139 fhuA Δ lacX74 galK16 galE15 e14- ϕ 80dlacZ Δ M15 recA1 relA1 endA1 nupG rpsL (Str^R) rph spoT1 Δ (mrr-hsdRMS-mcrBC)*; NEB) were used. Bacteria were transformed with the ligated plasmid from 2.6.1 to finally produce and purify plasmid DNA in a high demand. For transformation 100 μ l competent *E. coli* were thawed on ice and the ligation mixture was subsequently added to the thawed *E. coli*. After 1 h incubation on ice the mixture of *E. coli* cells and the ligated plasmid were treated with a heat shock (42 °C) in a water bath for 55 seconds, which facilitates plasmid uptake for bacterial cells. Following incubation on ice for 2 min, 900 μ l LB₀ medium (Carl Roth) was added to bacteria and the suspension was incubated for at least 1 h at 37 °C while shaking. After centrifugation (10 min; 4600 \times g; room temperature) 800 μ l of the supernatant was discarded and bacteria are resuspended in the remaining supernatant and were plated and cultured on respective agar selection plates over night at 37 °C.

2.6.3 Plasmid DNA extraction and purification from bacterial cells

After successful transformation of *E. coli* bacteria with newly generated plasmid DNA or existing plasmid DNA for re-transformations, single bacterial colonies on selective agar plates from 2.6.2 are used to extract plasmid DNA and check for its correctness. Therefore, single colonies were picked, and each bacterial colony is transferred into its own reaction vessel containing LB₀ medium, including respective antibiotics, and incubated over night at 37 °C while shaking. On the following day, LB₀ medium turned into a turbid suspension which indicates that bacteria have been replicated, why plasmid DNA was extracted and purified from bacterial cells at this day. Extraction and purification of lower plasmid amounts for control digests and control DNA sequencing of plasmids was performed by Plasmid-Mini-Purification (MiniPrep). After confirmation of the correct plasmid DNA sequence a higher yield of plasmids for usage in different experiments was generated by Plasmid-Maxi-Purification (MaxiPrep).

MiniPrep was performed using the QIAprep Spin Miniprep Kit (Qiagen), while the QIAGEN Plasmid Maxi Kit (Qiagen) was used for MaxiPrep. Both plasmid purification kits were used according to the manufacturer's protocol. Concentration of purified plasmids was measured by spectrophotometric analysis and plasmids were subsequently stored in the fridge at 4 °C upon usage.

2.6.4 Control digests and DNA sequencing of plasmids

Extracted and purified plasmids by MiniPrep were used to perform control digests and DNA sequencing of plasmids. First purified plasmids were used to perform a control digest to confirm successful DNA fragment insertion in the plasmid. Therefore, plasmid solution was treated for 2 h at 37 °C with respective endonucleases and resulting DNA bands were separated by agarose gel electrophoresis. The presence of a digested vector and a released insert in the gel confirmed the successful DNA fragment insertion into the plasmid. As a second control step the correct DNA sequence of the plasmid was confirmed by DNA sequencing. Here, plasmid DNA was diluted to a concentration of 100 ng/μl and sent to the commercially available sequencing service of LGC Genomics (LGC Genomics, Berlin, Germany). Primers for cloning as well as standard primers provided by LGC Genomics were used for DNA sequencing. The resulting sequence was checked for correctness by DNA nucleotide sequence alignments (Nucleotide BLAST; NCBI) in comparison to the respective cDNA sequence from the DNA fragment of interest. In addition, the correct reading frame of the cDNA sequence in relation to the vector sequences was verified using the Serial Cloner software (SerialBasics, Franck Perez).

2.7 Cell culture techniques

HEK293, HeLa cells (both from ATCC, Manassas, Virginia, USA), immortalized mouse embryonic fibroblasts (iMEFs) and primary mouse embryonic fibroblasts (pMEF) were cultured in Dulbecco's Modified Eagle's Medium (DMEM; ThermoFisher) supplemented with 10 % (v/v) fetal calf serum (FCSIII; GE Healthcare Life Sciences, Chalfont St Giles, UK), 2 mM L-glutamine (ThermoFisher), penicillin (100 units/ml; ThermoFisher) and streptomycin (100 μg/ml; ThermoFisher) at 37 °C, 5 % CO₂, 95 % humidity and were passaged regularly at 80 % confluency. Passaging of cells was performed by washing cells once with 1x PBS (Sigma-Aldrich), detaching cells using 0.05 % Trypsin-EDTA solution (ThermoFisher) and inactivating Trypsin-EDTA with an appropriate amount of *Full Medium* (DMEM, 10 % FCSIII,

2 mM L-glutamine, 100 units/ml Penicillin, 100 µg/ml Streptomycin). Finally, a fraction of the cell suspension was transferred to a new culture dish containing fresh *Full Medium*. The chapter ‘Cell culture techniques’ and the belonging sections (2.7.1 - 2.7.3) are written as described in standard protocols of the Kerkhoff laboratory and as presented in Welz, 2018.

2.7.1 Thawing cells

A cryovial of HEK293, HeLa cells, immortalized mouse embryonic fibroblasts (iMEFs) or primary mouse embryonic fibroblasts (pMEF) was taken out of long-term liquid nitrogen storage and frozen cells were thawed rapidly (< 1 minute) in a 37 °C water bath. Thawed cells were transferred into a 50 ml centrifuge tube containing 15 ml prewarmed *Full Medium* and centrifugated for 6 min at 800 × g, room temperature. Supernatant was discarded, and cell pellet was gently resuspended in 1 ml of *Full Medium*. Finally, the cell suspension was transferred into a new 10 cm culture dish (Greiner Bio-One) containing prewarmed *Full Medium* and cells were cultured at 37 °C, 5 % CO₂.

2.7.2 Freezing cells

For long-term storage eukaryotic cells are kept in liquid nitrogen and thawed upon request. Cells were frozen in a special *Freezing Medium* containing *Full Medium* supplemented with FCSIII and the cryoprotective agent dimethylsulfoxide (DMSO). In this context, DMSO allows a slow cooling of the *Freezing Medium* by reducing the freezing point of the medium and therefore avoids the risk of ice crystal formation, which can cause cell damages and cell death. The specific *Freezing Medium* is prepared with DMEM supplemented with 10 % DMSO, 20 % FCSIII, 2 mM L-Glutamine, penicillin (100 units/ml) and streptomycin (100 µg/ml). Cultured cells from eight 10 cm culture dishes were washed with 1x PBS, detached using Trypsin-EDTA and Trypsin-EDTA was inactivated by adding *Full Medium*. Cell suspension was transferred to a 50 ml centrifuge tube containing 5 ml *Freezing Medium* and centrifuged for 6 min at 800 × g, room temperature. Supernatant was discarded, cell pellet gently resuspended in 18 ml *Freezing Medium* and 1 ml aliquots were transferred into cryovials (ThermoFisher). Aliquots were transferred in a cryo-box filled with isopropanol, which allows a slow cooling at -80 °C of the aliquots at a rate of 1 °C/h and therefore inhibits formation of intracellular ice crystals causing cell damage and cell death. At the next day the aliquots are transferred into liquid nitrogen for extended storage periods.

2.7.3 Seeding cells

For most experiments a certain number of cells were seeded on 6-well plates (Greiner Bio-One), microscope cover glasses (A. Hartenstein, Würzburg, Germany) or WillCo dishes (WillCo-Dish, 40 mm; WillCo Wells B.V., Amsterdam, The Netherlands). Therefore, cells from a 10 cm culture dish were detached using Trypsin-EDTA (as described for passaging cells) and the number of cells in the cell suspension was determined by using a Neubauer counting chamber (Paul Marienfeld GmbH & Co. KG, Lauda-Königshofen, Germany). To distinguish between dead and living cells 10 μ l Trypan Blue solution (0.4 %; Sigma-Aldrich) were mixed with 10 μ l of the cell suspension and mixture was transferred to the Neubauer counting chamber. Viable cells in the four independent quadrants, each with an area of 1 mm² and a height of 0.1 mm, were counted and the mean value was calculated. The cell suspension was diluted in a 1:1 ratio with Trypan Blue solution, why the mean value was multiplied by 2 to equal the dilution factor. Finally, this value represented the number of cells in a volume of 0.1 μ l from the cell suspension, because 1 mm² (quadrant area) \times 0.1 mm (quadrant height) = 0.1 mm³ (quadrant volume) = 0.1 μ l. The total number of cells was calculated for the cell suspension and by determining the appropriate volume of a certain cell number, a certain cell number was seeded in appropriate culture vessels containing pre-warmed *Full Medium*. Cells were cultured at 37 °C, 5 % CO₂.

2.7.4 Staining of mitochondria in eukaryotic cells

In order to fluorescently label mitochondrial membranes in living HeLa cells and fibroblasts the cell permeable compound MitoTracker Orange (ThermoFisher) was used. Cells were seeded on glass-bottom cell culture dishes (WillCo-Dish, 40 mm; WillCo Wells B.V.) 20 h prior to the experiment. On the next day cells were washed in Opti-MEM (ThermoFisher) and incubated with 2 ml of a 5 nM MitoTracker Orange solution diluted in Opti-MEM for 20 min at 37 °C, 5 % CO₂. Cells were washed again with Opti-MEM to get rid of excess staining solution and covered with Opti-MEM for subsequent fluorescence live cell imaging (method written as presented in Kollmar, Welz, Straub et al., 2019).

In addition, the cell-permeable dye tetramethylrhodamine-methylester (TMRM; ThermoFisher) was used to stain specifically functional mitochondria. In this context, the staining procedure was done to the manufacturer's protocol. In the present thesis, mitochondria are stained with 100 nM TMRM.

2.7.5 Transfection of eukaryotic cells using Lipofectamine2000 reagent

Transfections with plasmid DNA were performed using Lipofectamine2000 reagent (ThermoFisher) according to manufacturer's recommendation. In case of low transfection rates, the plasmid concentration and / or the amount of Lipofectamine2000 reagent was adjusted.

2.8 Colocalization studies

The extent of colocalization from SPIRE1 with SPIRE1-E9, mitoSPIRE1 or SPIRE2, respectively, at vesicle surfaces or of mitoSPIRE1 or isolated exon 13 with MYO5, formins or MitoTracker at mitochondrial membranes as well as the extent of all other colocalization studies was analyzed using the ImageJ (V2.0.0) plug-in Coloc2 (National Institute of Health, Bethesda, USA). Here, the colocalization rate is indicated by the Pearson's Correlation Coefficient (PCC) as a statistical measure to unravel a linear correlation between the intensity of different fluorescent signals. A PCC value of 1 indicates a perfect colocalization, 0 indicates a random colocalization and a PCC value of -1 indicates a mutually exclusive localization of the analyzed signals. To take the noise of each image into account and to gain an objective evaluation of PCC significance, a Costes significance test was performed. To do so, the pixels in one image were scrambled randomly and the correlation with the other (unscrambled) image was measured. Significance regarding correlation was observed when at least 95 % of randomized images show a PCC less than that of the original image, meaning that the probability for the measured correlation of two colors is significantly greater than the correlation of random overlap (Costes et al., 2004; Pompey et al., 2013). PCC values > 0.2 which failed Costes significance test (Costes p-value < 0.95) were excluded from the belonging experiment and not used for further statistical analysis (method written as presented in Pylypenko, Welz et al., 2016).

2.9 Immunostaining

HeLa cells were seeded on microscope cover glasses and transfected to transiently express fluorescently tagged SPIRE, FMN, INF2 and MYO5 proteins as well as Myc-epitope tagged SPIRE1 proteins, respectively. Cells were fixed with paraformaldehyde (3.7 % in 1x PBS; Carl Roth) for 20 min at 4 °C and subsequently permeabilized using 0.2 % Triton X-100 (in 1x PBS; Sigma-Aldrich) for 3.5 min, room temperature. In one experiment 20 µM Digitonin (ThermoFisher) for 3 min, room temperature, was used to permeabilize only the cell membrane.

Digitonin is a mild permeabilizer which specifically targets cholesterol-rich membranes such as the plasma membrane, whereas the mitochondria membranes are not affected due to their low concentration of cholesterol. Respective cells were incubated with anti-c-Myc (9E10, sc-40, 2 µg/ml, mouse monoclonal; Santa Cruz Biotechnology, Dallas, USA), anti-cytochrome C (33-8200, 5 µg/ml, mouse monoclonal, ThermoFisher) and anti-SPIRE1 (SA-2133, 50 µg/ml, rabbit polyclonal; Schumacher et al., 2004) antibodies, respectively, for 1 hour at room temperature, and conjugated anti-mouse TRITC (715-025-151, 9.75 µg/ml, from donkey; Dianova, Hamburg, Germany) and anti-rabbit Cy5 (711-175-152, 9.75 µg/ml, from donkey, Dianova) secondary antibodies, respectively, for 1 h at room temperature avoiding exposure to light. Finally, cells were mounted on microscope slides with Mowiol (Merck, Darmstadt, Germany), dried at room temperature in the dark and stored at 4 °C.

2.10 Microscopy

2.10.1 Microscopy of *in situ* hybridization experiments

Brain slices from *in situ* hybridization experiments were analyzed with a Leica DMR microscope, equipped with a Leica PL Fluotar 10x/0.30 objective and a Leica DFC320 digital camera (2,088 × 1,550 pixels (~ 3.3 MP); 3.45 µm × 3.45 µm pixel size; all from Leica, Wetzlar, Germany). Images were recorded using the Leica LASX software and further processed with Adobe Illustrator.

2.10.2 Fluorescence microscopy of fixed and immunostained cells

Fixed cells were analyzed with a Leica AF6000LX fluorescence microscope, equipped with a Leica HCX PL APO 63x/1.3 GLYC objective and a Leica DFC7000 GT digital camera (1,920 × 1,440 pixel (~ 2.8 MP); 4.54 µm × 4.54 µm pixel size; all from Leica). 3D stacks were recorded and processed with the Leica deconvolution software module. Images were recorded using the Leica LASX software and further processed with Adobe Illustrator.

2.10.3 Fluorescence microscopy of viable cells

Live cell imaging for the analysis of moving mitochondria was done with a Leica AM total internal reflection fluorescence (TIRF) MC microscope equipped with a Leica HCX PL APO 100x/1.47 oil objective (all from Leica) and a Hamamatsu EM-CCD C9100-02 digital camera

(1000 × 1000 pixel (~ 4.2 MP); 8 μm × 8 μm pixel size; Hamamatsu Photonics, Herrsching am Ammersee, Germany). For experiments in this thesis only the epifluorescence mode of the TIRF microscope was used. Movies were recorded using the Leica LASX software and further processed and analyzed with the IMARIS software (Bitplane, Zürich, Switzerland).

2.11 Quantification of mitochondrial length using microscopy and ImageJ

Mitochondria of primary mouse embryonic fibroblasts (pMEFs) from wild type, *SPIRE1* mutant and mitoSPIRE1 knockout mice were stained as described above with MitoTracker Orange. In fluorescence live cell microscopy, cells with stained mitochondria were recorded using the Leica AM TIRF MC microscope equipped with a Leica HCX PL APO 100x/1.47 oil objective (all from Leica) and a Hamamatsu EM-CCD C9100-02 digital camera (1000 × 1000 pixel (~ 4.2 MP); 8 μm × 8 μm pixel size; Hamamatsu Photonics). In this context, a randomly chosen section including ~ 10 cells was imaged to record cells with all kinds of mitochondria sizes, which reduced a bias caused by unconscious picking single cells with a specific mitochondrial length by the experimenter. Images were then transferred to ImageJ (National Institute of Health) and the scale was set. The maximal length of each mitochondrion was traced with the tool *freehand line*, followed by length measurement of the drawn line, which therefore represented the length of the mitochondrion. For comparison all measured mitochondrial lengths of a specific genotype were taken together and the mean was calculated. Evaluated means were blotted in a graph and statistics was done. Imaging and analysis of mitochondrial length was blinded.

2.12 Quantification of mitochondrial motility

Mitochondrial motility of primary mouse embryonic fibroblasts (pMEFs) from wild type, *SPIRE1* mutant and mitoSPIRE1 knockout mice was evaluated with IMARIS (Bitplane). First mitochondria were stained with MitoTracker Orange as described above and recorded in a live cell imaging with a Leica AM TIRF MC microscope equipped with a Leica HCX PL APO 100x/1.47 oil objective (all from Leica) and a Hamamatsu EM-CCD C9100-02 digital camera (1000 × 1000 pixel (~ 4.2 MP); 8 μm × 8 μm pixel size; Hamamatsu Photonics). Imaged cells were picked randomly and mitochondria movement from these cells was recorded for 20 sec (1 image/500 ms). Movies of motile mitochondria were transferred as Leica project files to IMARIS and movies were processed with the integrated Matlab background subtraction (The

MathWorks, Natick, USA). In the following step mitochondria were tracked with the surface tool (Max Distance: 1.5 μm ; Max Gap Size: 3 μm) of IMARIS. Mitochondria movement was difficult to track automatically, because mitochondria crossed each other and sometimes moved fast, because of which IMARIS lost tracks or generated incorrect tracks. For this reason, automatically tracked mitochondria by the surface tool of IMARIS were checked manually and in case of missing or wrong tracks, tracks were corrected manually. Based on the measured tracks IMARIS calculated parameters like track length, maximal track length or maximal velocity of mitochondria and these results were exported and saved as Excel-files. Data were used to determine the percentage of moving, wiggling and stationary mitochondria in pMEFs from wild type, *SPIRE1* mutant and mitoSPIRE1 knockout mice. Here, moving mitochondria were determined as mitochondria which had a track length $> 4 \mu\text{m}/20 \text{ sec}$, while wiggling mitochondria had a track length of 1.5 - 4 $\mu\text{m}/20 \text{ sec}$, and stationary mitochondria moved less than 1.5 $\mu\text{m}/20 \text{ sec}$. The calculated parameters from IMARIS were defined as follows; 'Track length' describes the covered distance of moving mitochondria per time interval. 'Maximal track length' defines the largest covered distance by a moving mitochondrion of a cell per time interval. 'Maximal velocity' determines the highest speed reached by moving mitochondria while transportation. Each parameter was calculated for all moving mitochondria of a cell. Data were summarized in Excel (Microsoft Corporation, Albuquerque, USA) and further processed to generate means of parameters per cell. For the presentation of parameters in a bar diagram, the average of all mean values calculated per cell was evaluated. The same procedure was used to measure mitochondrial motility when mitoSPIRE1 was transiently overexpressed in pMEFs. Transiently overexpression of AcGFP1 was used as a control and all transfections were performed as described above. Results were finally summarized in graphs and statistics were determined.

2.13 Analysis of MYO5A positive mitochondria and mitochondrial sizes using FAMS

Fluorescence-activated mitochondria sorting (FAMS) is based on the principle of a standard fluorescence-activated cell sorting (FACS) machine. FAMS allows to identify mitochondrial surface molecules and to determine size of fluorescent stained mitochondria. For FAMS cultured cells were detached and collected by centrifugation ($300 \times g$ for 5 minutes). The cell pellet was resuspended in FACS buffer (1x PBS pH 7.2, 0.5 % BSA, 2 mM EDTA) at a cell density of 1×10^6 cells/ml. Cells were incubated with 100 nM MitoTracker Red CMXRos

(MTR; ThermoFisher) at 37 °C, 5 % CO₂ for 15 minutes. Cell suspensions were pelleted at 300 × g and resuspended in 1 ml of ice-cold hypo-osmotic buffer (RSB Hypo Buffer, Cold Spring Harbor Protocols; 10 mM NaCl, 1.5 mM MgCl₂, 10 mM Tris-HCl (pH 7.6)). Following a ten-minute swelling period at 4 °C, samples were subjected to 35 strokes of dounce homogenization. Cell lysates were centrifuged at 12,000 × g for 5 minutes at 4 °C. Supernatant was aspirated, and pellets were resuspended in blocking buffer (0.2 % BSA and 2 % fetal bovine serum in 1x PBS) and incubated at room temperature for 20 minutes. Samples were centrifuged at 12,000 × g for 5 minutes and then incubated with anti-myosin 5A antibody (G-4, sc-365986, 0.75 µg/ml, mouse monoclonal, Santa Cruz Biotechnology) conjugated to PE-Cy7 (Abcam, Cambridge, UK). Samples were pelleted at 12,000 × g and resuspended in buffered blood bank saline (0.85 % (w/v) isotonic solution; ThermoFisher) for analysis via nanoscale flow cytometry as described in MacDonald et al., 2019. Briefly, assessment of mitochondria was performed using a special ordered BD FACS Aria III, fitted with a photomultiplier tube detector for forward light scatter of a 488 nm laser. Mitochondria were identified by size and positive fluorescence using mitochondrial-specific dye (MTR) in comparison to unstained negative control samples, allowing up to 0.5 % false positive events versus controls. Spectral overlap from MTR in PE-Cy7 channel was corrected manually using single color samples. For each sample, 50,000 events in total were analyzed. Data were acquired using BD FACSDiva software (version 8.0.2; Becton Dickinson, Franklin Lakes, USA) and analysis performed using FlowJo (version 10; FlowJo LLC, Ashland, USA). Method was described and performed in collaboration with Hannah (Sheehan) Alberico and Prof. Dr. Dori Woods at Northeastern University.

2.14 Software

2.14.1 Statistical analysis

For all statistical analysis the software SPSS (IBM, Armonk, USA) or SigmaPlot (Systat Software GmbH, Erkrath, Germany) was used. To compare more than two groups on one level a One-way analysis of variance (ANOVA) was performed, while the comparison of more than two groups on two levels was employed by a Two-way ANOVA. If ANOVA revealed a significant difference and data are distributed normally a Tukey-Kramer test was used as post-hoc analysis, while for data which failed normality test a Mann-Whitney-U-test was performed. Statistical analysis between two groups was performed if normality test was passed by t-test and if normality test failed by Mann-Whitney-U-test. A difference between groups was

determined as significant if the alpha level of post-hoc analysis was < 0.05 . For groups with $n > 25$ the effect size was determined as well. In this context, for One-way ANOVA analysis eta squared (η^2) was calculated to determine the effect size ($\eta^2 > 0.01 - 0.06$, describes a small effect size; $\eta^2 > 0.06 - 0.14$, describes a medium effect size; $\eta^2 > 0.14$ describes a large effect size). For Two-way ANOVA analysis partial eta squared (η^2_p) was calculated to determine the effect size ($\eta^2_p > 0.1 - 0.3$, describes a small effect size; $\eta^2_p > 0.3 - 0.5$, describes a medium effect size; $\eta^2_p > 0.5$ describes a large effect size).

2.14.2 Graphs and cartoons

In general, diagrams were generated in SigmaPlot (Systat Software GmbH, Erkrath, Germany), while FAMS graphs were employed in FlowJo (FlowJo LLC). The online tool Protein Homology / analogY Recognition Engine V 2.0 (PHYRE; Structural Bioinformatics Group, London, UK) was used to predict the secondary protein structure of the alternatively spliced exon 13 from the *SPIRE1* gene and the resulting raw structure was further processed in PyMOL (Schrödinger LLC, New York, USA). Diagrams and graphs from all software mentioned above were further processed in Adobe Illustrator (Adobe Inc., San José, USA). In addition, all cartoons in the present thesis were designed with Adobe Illustrator and Adobe Illustrator was finally used to organize colors, lettering and layout of figures.

2.14.3 Written work

The present thesis and all other written work during my PhD such as progress reports were performed with Microsoft Word (Microsoft Corporation).

2.14.4 Identification of protein domains

The online tool ‘Simple Modular Architecture Research Tool’ (SMART; <http://smart.embl-heidelberg.de>) allows the identification of domain organizations and the belonging amino acid boundaries from specific amino acid sequences. These informations were used to draw proteins with their belonging domains in the here presented cartoons in scale. The amino acid sequence from the protein of interest was analyzed using the *normal* SMART tool.

2.14.5 DNA and cDNA sequences

Respective DNA / cDNA sequences were obtained from the NCBI Gene database (<https://www.ncbi.nlm.nih.gov>). The Serial Cloner software was used to translate cDNA in amino acid sequences.

2.15 Mitochondrial respiration

The mitochondrial respiration of primary mouse embryonic fibroblasts (pMEFs) from wild type and *SPIRE1* mutant mice was studied by analyzing the oxygen consumption rate (OCR) using the *Seahorse Flux Analyzer* (Agilent Technologies, Santa Clara, USA). 25×10^3 wild type or *SPIRE1* mutant pMEFs were grown for 24 hours in XFp 8 well miniplates (Agilent Technologies) at 37 °C, 5 % CO₂. Cartridges were prepared according to manufacturer's recommendation and the OCR from different metabolic stages of mitochondria was analyzed using the XFp Cell Mito Stress Kit (Agilent Technologies) containing the mitochondrial stress compounds oligomycin (1 μM), carbonilcyanide p-triflouromethoxyphenylhydrazone (FCCP; 2 μM) and antimycin A / rotenone (1 μM). The OCR was measured by means of a XFp *Seahorse Flux Analyzer* (Agilent Technologies).

2.16 Isolation of pMEFs from mouse embryos

For successful isolation of primary mouse embryonic fibroblasts (pMEFs) from homozygous mitoSPIRE1 knockout and wild type embryos heterozygous mitoSPIRE1 knockout mice were crossbred. Furthermore, heterozygous *SPIRE1* mutant mice were crossbred to isolate pMEFs from homozygous *SPIRE1* mutant and wild type embryos. In this thesis only pMEFs from mother mice which gave birth to heterozygous and to both homozygous genetic possibilities were used. At embryonic day 14.5 pregnant mice were killed by cervical dislocation. The uterus was removed from the mouse, embryos were isolated and stored in a petri dish with cold sterile 1x PBS. Two limbs of each embryo were collected and used for following genotyping of the embryos by PCR. Each embryo was handled individually and within 60 minutes after death of the mother animal. After removing all red organs from the embryo, the belonging embryonal body was washed with 1x PBS to remove as much blood as possible. In the next step the embryo was sliced into fine pieces with the help of two scalpels (Megro, Wesel, Germany) and transferred into a 15 ml conical tube containing 3 ml of ice-cold 0.05 % Trypsin-EDTA solution (ThermoFisher). Conical tubes were stored over night at 4 °C to allow the trypsin to diffuse

into the tissue. Between preparation of different embryos scissors (Megro), forceps (Dumont, Montignez, Switzerland) and scalpels were washed with 70 % ethanol and water to avoid cross-contamination between different genotypes. At the next day the Trypsin-EDTA supernatant was discarded and the tubes containing the embryonal tissue were incubated for 15 min at 37 °C in a water bath. Adding 3 ml *Full Medium* to each embryo inactivated Trypsin-EDTA and facilitated a gentle homogenization of tissue clumps by pipetting gently up and down with a 1000 µl pipette tip (Axygen, Corning, USA) and a 200 µl pipette tip (Sarstedt). The cell suspension of each embryo contained pMEFs and was finally transferred into four 10 cm tissue culture plates containing 10 ml of *Full Medium*. pMEFs were cultured at 37 °C, 5 % CO₂, 95 % humidity and were passaged regularly at 80 % confluency. pMEFs were frozen for long-term storage and thawed as required for experiments. All experiments with pMEFs were done with cells not older than passage five, because proliferation rate of pMEFs in culture decreases dramatically after five passages (method written as described in the standard protocol of the Kerkhoff laboratory).

2.17 *In situ* hybridization

In situ hybridization allows to visualize the distribution of specific nucleic acid sequences in cells within a tissue section or in an entire organ. The mentioned technique is based on the principle that two complementary strands of nucleic acids bind to each other. In this thesis we visualized the abundance of *SPIRE1* and *mitoSPIRE1* mRNA in the mouse brain. In this context, we used a Digoxigenin (DIG)-labeled single stranded RNA probe to detect expression of the *SPIRE* splice variants of interest in paraffin embedded sections.

For mouse brain paraffin embedded block preparation wild type and *mitoSPIRE1* knockout mice were euthanized by cervical dislocation and intracardially perfused with first 20 ml of 1x PBS and then with 20 ml of 3.7 % paraformaldehyde. Immediately after perfusion mouse brains were dissected, rinsed in 1x PBS and post fixed over night at 4 °C in 3.7 % paraformaldehyde. At the next day the fixed mouse brain tissue was washed for 60 minutes in 1x PBS and as described below embedded in a paraffin block. After washing with 1x PBS the brain tissue was dehydrated with 50 %, 70 %, 80 %, 96 % and pure ethanol. The dehydrated mouse brain tissues were then immersed for 90 min in acetone / ethanol (1:1) and for 60 min in acetone at room temperature. Finally, the prepared brain tissues were embedded in prewarmed paraffin (63 °C) for 3 hours and cooled at room temperature.

Paraffin sections later used for *in situ* hybridization were prepared by cutting brain paraffin embedded block with a microtome at a thickness of 6 μm . Paraffined brain sections were placed on Poly-L-lysine (Sigma-Aldrich) covered slides. Slides were deparaffinized in a vertical position by incubation at 68 °C for 45 min and Xylol (Carl Roth; 2 times for 10 min) treatment. The brain sections were then rehydrated in a decreasing concentration of ethanol. Here we used a pure ethanol bath for 2 min (2 times) and a single 100 %, 95 %, 70 %, 50 % ethanol bath each for 1 min, followed by two DEPC-H₂O water baths (30 seconds each).

For prehybridization rehydrated brain sections were then incubated first with 1x PBS / DEPC (pH 7.4; 2 times for 5 min) and successively two times for 5 min with 1x PBS / DEPC containing 100 mM Glycine. Sections were then incubated with 1x PBS / DEPC containing 0.3 % Triton X-100 for 15 min. After washing the brain sections two times with 1x PBS / DEPC brain sections are incubated for antigen retrieval in TE-Buffer containing 20 $\mu\text{g}/\text{ml}$ proteinase K for 30 min at 37 °C. After treatment with 1x PBS / DEPC containing 100 mM Glycine (2 times for 5 min) brain sections were washed with 1x PBS / DEPC and post-fixed with 3.7 % PFA in 1x PBS / DEPC for 5 min at room temperature. After washing with 1x PBS / DEPC the brain sections were incubated with prehybridization buffer (50 % deionized formamide, 1x Denhardt's solution, 10 mM DTT, 4x SCC, 10 % Dextran sulfate, 1 mg/ml yeast t-RNA and 1 mg/ml salmon sperm DNA) at 37 °C for 3 hours to block non-specific nucleic acid interactions and reduce background noise. The prehybridization buffer was denaturated at 95 °C for 3 min and chilled on ice before it was added to the brain sections.

For hybridization of brain sections 15 μl of specific DIG-labeled RNA probe was added to prehybridization buffer to obtain a final concentration of 2 ng/ μl and used as hybridization mix. The hybridization mix was denaturated at 95 °C for 3 min and chilled on ice before it was added to the brain sections. With hybridization mix extended covered brain sections were engulfed with parafilm and incubated over night at 60 °C in a humid chamber. DIG-labeled RNA probes for *mitoSPIRE1* and *SPIRE1* were generated by DIG RNA Labeling Kit (Merck) according to manufacturer's recommendation.

During posthybridization it was not necessary to work RNase free. Slides with brain sections were immersed in 2x SSC to remove parafilm and then washed 3 times (each for 20 min) with 2x SSC at room temperature. Subsequently slides were washed 40 min with 0.5x SSC/20 % formamide (Carl Roth) at 50 °C and 20 min with 0.5x SSC/20 % formamide at 37 °C. To digest any single stranded RNAs in the brain section slides were first treated for 15 min with NTE

buffer and then for 30 min with NTE buffer containing 20 µg/ml RNase A (Qiagen) both at 37 °C. Afterwards slides were washed with 0.5x SSC/20 % formamide at 50 °C and subsequently with 2x SSC/20 % formamide at room temperature both for 30 min.

Immunological detection of hybridized DIG-labeled RNA probes was facilitated by an alkaline phosphatase conjugated anti-Digoxigenin antibody (11093274910, 1:5000 \cong 0.1646 units/ml, sheep polyclonal; Merck-Millipore, Darmstadt, Germany). First the brain sections were blocked with blocking buffer for 1 hour at room temperature. Subsequently mentioned antibody was diluted in blocking buffer (1:5000) and sections were incubated over night at 4 °C. At the next day slides were washed four times (each 5 min) with TBST, three times (each 15 min) with TBST, two times (each 10 min) with NTMT buffer and at least for 10 min with NTMT buffer containing 2 mM levamisole, which inhibits the endogenous alkaline phosphatase activity. Finally, alkaline phosphatase activity was visualized by incubating the sections with BM purple (Roche, Basel, Switzerland) for six days at 4 °C in the dark. The BM purple solution on the slides was changed every two days by a fresh one. After color development has finished, slides were washed two times (each 15 min) with NTMT buffer, a single time (10 min) with 1x PBS and for 1 min with Millipore-H₂O. Tissue sections were analyzed and recorded using a Leica DMR microscope (method written as presented in Pleiser, 2012).

2.18 Protein work

The belonging sections (2.18.1 - 2.18.3) of the chapter ‘protein work’ are written as presented in Pylypenko, Welz et al., 2016 and as presented in Welz, 2018.

2.18.1 Recombinant protein expression and purification

Recombinant GST-mm-FMN2-eFSI (GST-FMN2-eFSI) proteins were expressed in *Escherichia coli* Rosetta bacterial cells (Merck Millipore). Bacteria were cultured in LB medium (100 mg/l ampicillin, 34 mg/l chloramphenicol) at 37 °C until an OD_{600nm} of 0.6 - 0.8. Protein expression was induced by 0.2 mM Isopropyl-β-D-thiogalactopyranoside (Sigma-Aldrich) and continued at 20 °C for 20 h. Bacteria were harvested and lysed by ultra-sonication. Soluble proteins were purified in two consecutive steps. GSH-Sepharose 4B beads (GE Healthcare Life Sciences) were used first for an affinity-based batch purification process which was followed by size exclusion chromatography using an ÄKTApurifier system

and a High Load 16/60 Superdex 200 SEC column (both GE Healthcare Life Sciences). Proteins were concentrated by ultrafiltration using Amicon Ultra centrifugal filters (Merck Millipore) with 50 kDa cut off. The final protein purity was estimated by SDS-PAGE and Coomassie staining. Purification of GST-FMN2-eFSI was done by Dr. Tobias Welz from the Kerkhoff laboratory.

2.18.2 GST-pulldown from wild type and mitoSPIRE1 knockout fibroblast lysates

For GST-pulldowns eight 10 cm cell culture dishes of primary mouse embryonic fibroblasts (pMEFs) from each, wild type and mitoSPIRE1 knockout mice were cultured. When cells reached a confluency of 80 % cells were lysed in lysis buffer (25 mM Tris-HCl pH 7.4, 150 mM NaCl, 5 mM MgCl₂, 10 % (v/v) glycerol, 0.1 % (v/v) Nonidet P-40, 1 mM PMSF, protease inhibitor cocktail) and centrifuged at 20,000 × g, 4 °C, 20 min to remove insoluble debris. For GST-pulldown assays 40 µg GST-FMN2-eFSI and 20 µg GST protein as control was coupled to GSH-Sepharose 4B beads for 1 hr, 4 °C on a rotating wheel. Beads were washed twice with pulldown buffer (25 mM Tris-HCl pH 7.4, 150 mM NaCl, 5 mM MgCl₂, 10 % (v/v) glycerol, 0.1 % (v/v) Nonidet P-40) and subsequently incubated with the cell lysates for 2 h at 4 °C on a rotating wheel. Beads were washed four times with pulldown buffer and bound proteins were eluted with 1x Laemmli buffer, denatured at 95 °C for 10 min and then analyzed by immunoblotting.

2.18.3 Immunoblotting

Immunoblotting was performed using Sodium dodecyl sulfate polyacrylamide gel electrophoresis (SDS-PAGE) to separate proteins and Western blotting to visualize the presence of specific proteins.

Protein samples were mixed with SDS sample buffer (Laemmli buffer) containing the anionic detergent sodium dodecyl sulfate (SDS) and denatured at 95 °C for 10 min in a heat block. SDS charges the proteins negatively, which allowed in the following process to separate the proteins under voltage solely by their molecular weight in a polyacrylamide gel, regardless of their individual charges. Here we used an 7.5 % SDS gel and separation was done at 50 mA per gel in 1x SDS-PAGE-buffer. Negatively charged proteins move towards the positively charged anode. In this context, in the polyacrylamide gel smaller proteins move faster than larger

proteins towards the positively charged pole, why they were separated from each other. All gel pockets are loaded with the same sample volume.

In the Western blotting technique separated proteins are transferred from the polyacrylamide gel onto a nitrocellulose membrane (Protran Nitrocellulose Transfer Membrane, 0.45 µm pore size; GE Healthcare Life Sciences) by use of the Mini Trans-Blot Cell system (Bio-Rad Laboratories, Inc (Bio-Rad), Hercules, USA) in 1x Transfer buffer (containing 20 % methanol). Proteins are transferred at 150 mA, room temperature for 2 h. Subsequently a Ponceau S staining was performed to confirm a successful protein transfer to the nitrocellulose membrane and to check for equal loading in all lanes. Here, the nitrocellulose membrane was incubated for 5 min in Ponceau S staining solution (Sigma-Aldrich) and then washed with de-ionised water until all background coloring was gone and protein bands were well defined. Finally, the membrane was completely de-stained by repeated washing with 1x PBST.

In the next step proteins on the nitrocellulose membrane were visualized by specific antibodies. In order to prevent unspecific antibody binding, the membrane was blocked in 5 % milk powder solution (Carl Roth) in 1x PBST at 4 °C over night. At the next day the membrane was incubated with an anti-SPIRE1 primary antibody (SA-2133, 0.5 µg/ml, rabbit polyclonal; Schumacher et al., 2004; 1x PBST, 3 h, room temperature) and a horse-radish-peroxidase (HRP) linked anti-rabbit secondary antibody (NA934-1ML, 1:5000, from donkey, GE Healthcare Life Sciences; 1.6 % milk, 1 h, room temperature). The protein signal was detected by chemiluminescence (Luminata Forte Western HRP substrate; Merck Millipore) and recorded with an Image Quant LAS4000 system (GE Healthcare Life Sciences). Recorded images were processed in Adobe Photoshop and assembled in Adobe Illustrator.

2.19 Generation of the mitoSPIRE1 knockout mouse

The mitoSPIRE1 knockout mouse was generated by our collaboration partners Prof. Dr. Cord Brakebusch and Dr. Javier Martín Gonzalez from the University of Copenhagen. After an initial meeting at the University of Copenhagen, they generated the knockout mouse and finally transferred it 18 months later to our laboratory in Regensburg. Here we confirmed by PCR and RT-PCR the successful knockout of the alternatively spliced *exon 13* from the *SPIRE1* gene (chapter 3.7). By means of GST-pulldown assays we further confirmed that SPIRE proteins from the *SPIRE1* gene are still expressed (chapter 3.7). The following method sections

(2.19.1 - 2.19.6) were written by our collaboration partners who did the experimental procedures for the generation of the knockout mouse.

2.19.1 Overview of generating the mitoSPIRE1 knockout mouse

We have generated the mitoSPIRE1 knockout mice through the use of CRISPR / Cas9 gene editing technology. In here we have designed two targeting constructs (pX458-gRNA-1 and pX458-gRNA-2) that each express both the gRNA (guide RNA) and the Cas9 nuclease protein. Upon expression of these two components in the cells, the gRNA directs the Cas9 nuclease to the genomic regions of interest which, upon its interaction with the genome, results in a double strand break that is then repaired by the cell DNA repair mechanism.

Both gRNAs used here targeted Cas9 nuclease to two distinct locations that lay right before and after the *exon 13* of the *SPIRE1* gene. Upon nuclease activity a DNA sequence of approximately 179 bp is deleted. Figure 8 shows a schematic representation of the targeting strategy that was used to generate the mitoSPIRE1 knockout mouse model.

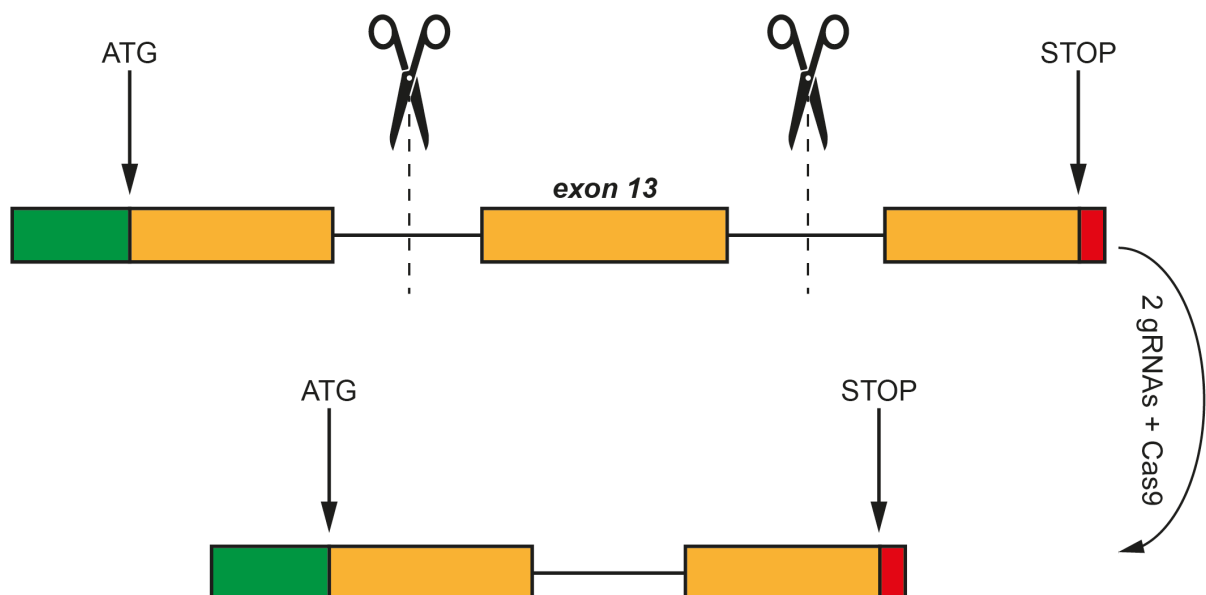


Figure 8 - Schematic representation of the CRISPR / Cas9 targeting strategy used to generate the mitoSPIRE1 knockout mouse model. For simplicity purposes, here are represented only 3 exons from the *SPIRE1* gene. Both gRNAs flank *exon 13*; upon expression of these two gRNAs in the cell, Cas9 protein is directed to the sequences of interest where it introduces a double strand break on either side of the *exon 13*. The cell DNA repair mechanism excises the *exon 13* and ligates both free ends of the DNA back together in a process called Non-homologous end joining.

2.19.2 Guide selection and cloning of CRISPR constructs

Potential gRNAs were screened using CRISPOR tool (www.crispor.tefor.net) and two of them were selected according to the following parameters: cutting site proximity to the location of interest, off target score and Doench score (Doench et al., 2016). The analysis resulted in two gRNAs (gRNA-1: TAGGAACCTGAACAATGGAAGGG and gRNA-2: CAGCAGGTGGAAACCCTCAAAGG; protospacer adjacent motif (PAM) sequence underlined) that were satisfactory to our requirements. These particular gRNAs have a Specificity Score of 66 and 79 which is a value that ranges from 0 to 100 and measures the uniqueness of a gRNA in the genome. Any gRNA with a specificity value above 50 is generally considered to be good (Hsu et al., 2013). Both gRNAs were individually cloned into the pX458 plasmid (Addgene, Watertown, USA), as described in Ran et al., 2013.

2.19.3 Embryonic Stem Cell targeting

F1.129S2; C57BL/6N embryonic stem cells (ES cells) were transfected with the above mentioned gRNAs and donor templates, following the protocol described in Yang et al., 2014. 1×10^6 ES cells were plated in two 10 cm petri dishes coated with gelatine and cultured in N2B27+2i+LIF medium. 4 hours later the cell culture was transfected with a mixture of 5 μ g pX458-gRNA-1 + 5 μ g pX458-gRNA-2 + 15 μ l FuGene following the vendor's instructions. 48 h later, GFP-positive cells were sorted by FACS and re-plated in gelatine-coated 10 cm Petri dishes (25,000 cells / dish). After one week in culture, 192 individual ES cell colonies were picked manually, disaggregated and plated on a feeder cell layer in 96-well plates. This clone set was split in triplicates: two of the copies were frozen and the third was expanded up to confluent 24-well plate wells for DNA extraction and genotyping.

2.19.4 Genotyping and targeting efficiency

ES cell clones were genotyped by PCR reaction using the following primers: *genomito SPIRE1*-FW: TCCCTCCAACCAAAAATGTC and *genomito SPIRE1*-REV: TCAGCAGTCAAAAGCAAAGTG. Electrophoresis analysis showed a band size of 749 bp corresponding to the wild type allele while the mutated allele shows a band size of 570 bp. The total number of ES cell clones genotyped was 96, of which 28 showed a band size that could correspond to the mutated allele. From those 28 positive clones, the first 10 were sent for sequencing where 5 of them clearly show the mutation of interest, where the others were

inconclusive due to the amount of sequencing background noise. Those 5 clones that were validated for a homozygous knockout by sequencing were: # 4, # 8, # 26, # 27 and # 28.

2.19.5 Off target screening

Off target sites were not screened. However, the gRNA-1 shows a total of 225 off targets where 204 of them have 4 mismatches, 19 have 3 mismatches and 2 have 2 mismatches. The gRNA-2 shows a total of 159 off target sites where 144 of them have 4 mismatches, 14 have 3 mismatches and 1 has 2 mismatches. Regarding the mismatches location, whether in the seed region of the gRNA (seed region is the proximal region to the PAM sequence where the presence of mismatches more significantly reduces the likelihood of targeting), the gRNA-1 has a total of 8 potential off target sites where 2 have 3 mismatches and the other 6 have 4 mismatches; whether the gRNA-2 has a total of 6 potential off target sites where 3 have 3 mismatches and the other 3 have 4 mismatched. None of the most likely 3 off target sites for each gRNA are located in the same chromosome of *SPIRE1*, which means that even in the unlikely event of off targeting those mutations will be diluted in the breeding generations.

2.19.6 Chimeric mice generation and breeding

Once the ES cell clones carrying the deletion were identified by PCR, one of the two frozen clone-set replicas were thawed and the selected clones were put in culture on a feeder cell layer in 96-well plates with N2B27+2i+LIF medium. Subsequently, these clones were then expanded in the same culture conditions transferred to 6-well plate wells. Cells were disaggregated to single cell suspension and microinjected into morula stage C57BL6/N embryos, at a ratio of 3 - 5 cells per morula. The injected embryos were transferred to pseudo-pregnant recipient CD1 females to be carried to term.

ES cell clones # 4 and # 27 were injected, each of them into 36 morulas. Clone # 4 gave rise to 8 newborns, but 3 of them died after birth; all of the other five turned out to be chimeric. Clone # 27 resulted in 10 newborns, but only 6 survived; out of those, 5 were chimeras. The contribution of the ES cells to the embryo was very high as all of the 10 chimeric pups generated (5 + 5) turned out to be male and 100 % ES cell-derived, assessed by coat color.

3. Results

A variety of eukaryotic expression vectors encoding fluorescent tagged SPIRE, MYO5, FMN and INF2 proteins were used to analyze the cellular functions and localization of mitoSPIRE1. To provide an orientation among constructs throughout the results section, all proteins encoded by expression vectors used are shown in Figure 9 and Figure 10. Detailed information regarding each expression vector is listed in the supplement.

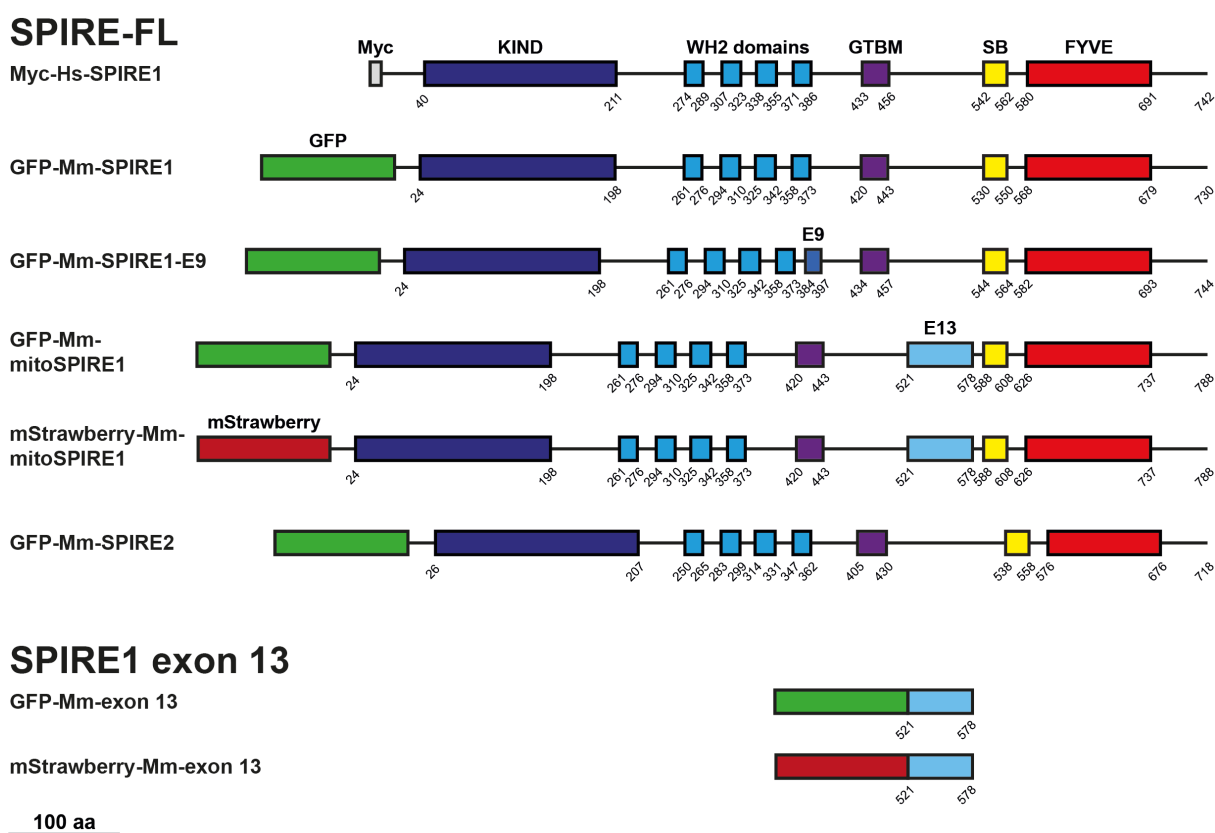


Figure 9 - Schematic overview of used SPIRE proteins encoded by expression vectors. Shown fluorescent tagged proteins encoded by expression vectors were used for single or multiple experiments. For a better overview, fluorescence tags (GFP and mStrawberry) are visualized in half of their amino acid size. Numbers indicate amino acids. *KIND*, kinase non-catalytic C-lobe domain; *WH2*, Wiskott-Aldrich-Syndrome protein homology 2; *E9*, exon 9; *GTBM*, globular tail domain binding motif; *E13*, exon 13; *SB*, SPIRE-box; *FYVE*, FYVE-type zinc-finger; *GFP*, green fluorescent protein; *FL*, full-length; *Hs*, Homo sapiens; *Mm*, Mus musculus; *aa*, amino acids.

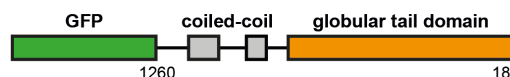
GFP

GFP (AcGFP1)

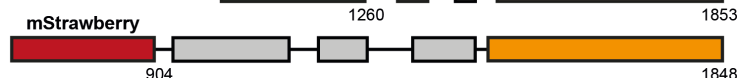


MYO5

GFP-Mm-MYO5A-CC-GTD

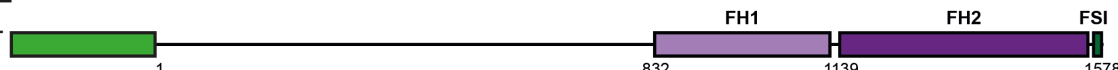


mStrawberry-Hs-MYO5B-CC-GTD



FMN2

GFP-Mm-FMN2-FL



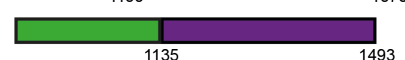
GFP-Mm-FMN2-FH2-FSI



GFP-Mm-FMN2-FH2-FSI-K1571A

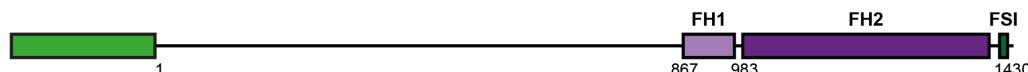


GFP-Mm-FMN2-FH2-C1493

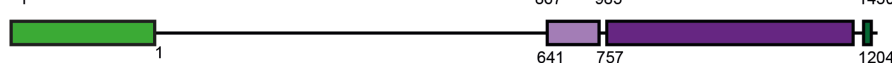


FMN1

GFP-Mm-FMN1A-FL



GFP-Mm-FMN1C-FL



INF2

GFP-Hs-INF2-FL-CAAX



GFP-Hs-INF2-FL-NonCAAX

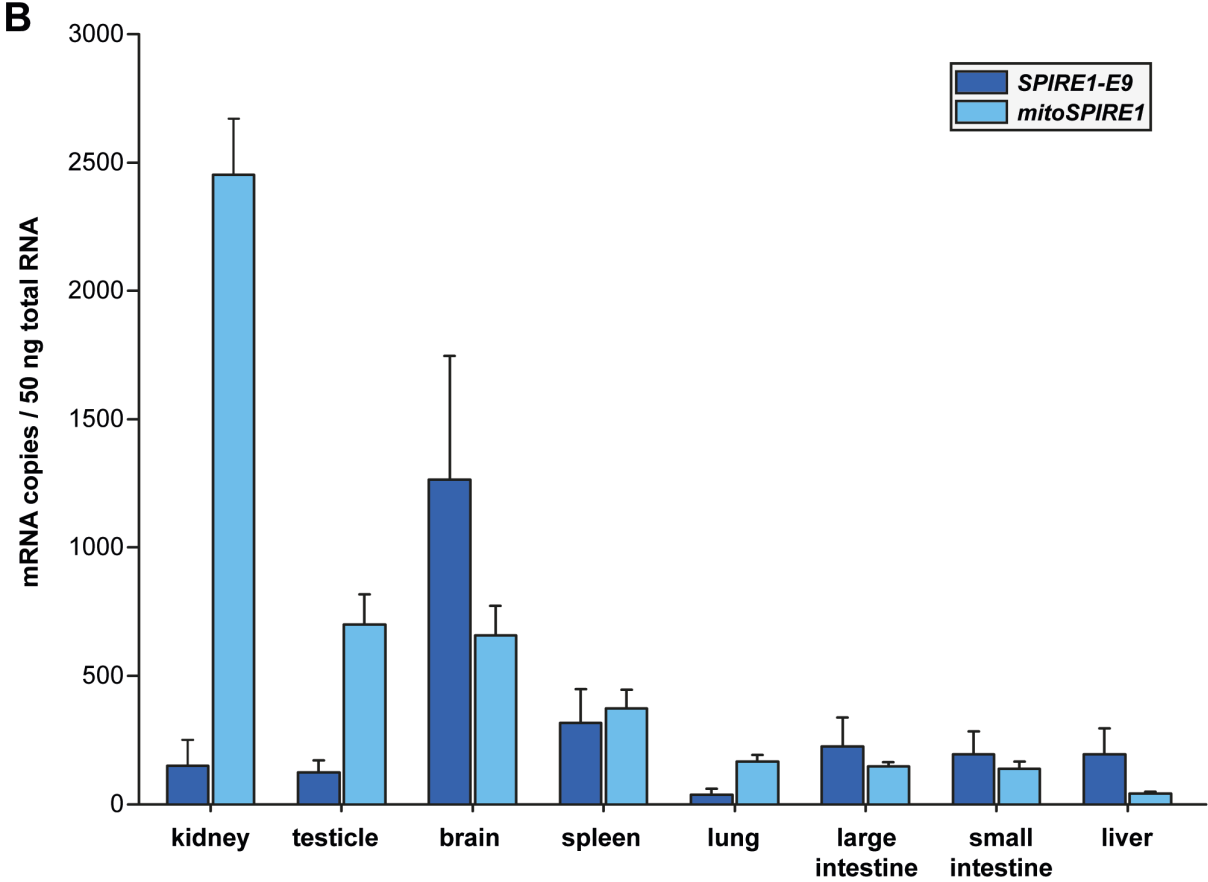
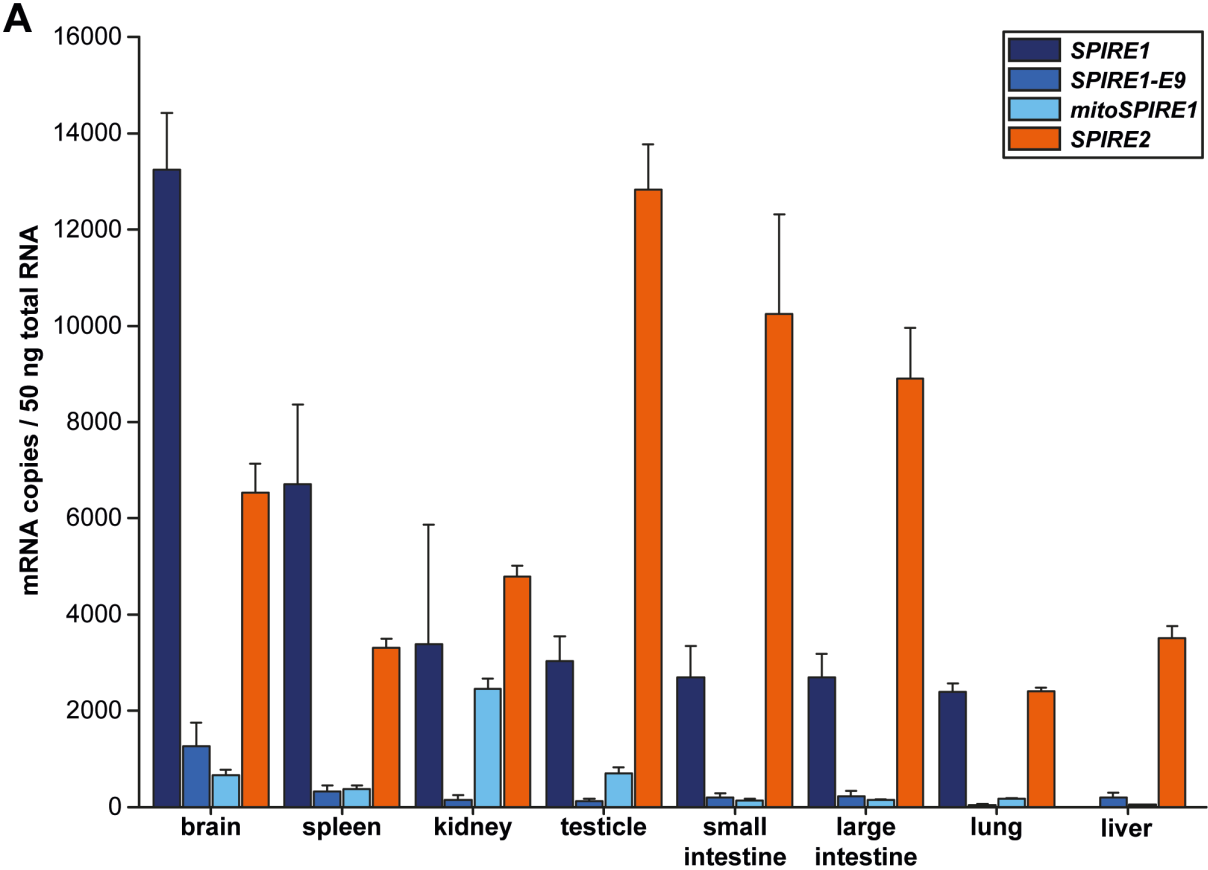


100 aa

Figure 10 - Schematic overview of used MYO5, FMN and INF2 proteins encoded by expression vectors. Shown fluorescent tagged proteins encoded by expression vectors were used for single or multiple experiments. Numbers indicate amino acids. *FH1*, formin homology domain 1; *FH2*, formin homology domain 2; *FSI*, formin-SPIRE Interaction; *GBD*, GTPase-binding domain; *FH3*, formin homology domain 3; *WH2*, Wiskott-Aldrich-Syndrome protein homology 2; *GFP*, green fluorescent protein; *FL*, full-length; *Hs*, Homo sapiens; *Mm*, Mus musculus; *aa*, amino acids.

3.1 Expression of *SPIRE* splice variants in mouse tissues

The mammalian genome encodes two *SPIRE* actin nucleator genes. In addition, the *SPIRE1* gene contains two alternatively spliced exons (*exon 9* and *exon 13*). As a result, the two *SPIRE* genes encode for four different proteins, *SPIRE1*, *SPIRE1-E9*, *mitoSPIRE1* and *SPIRE2*. A *SPIRE* protein which contains both the *exon 9* and the *exon 13* is not expressed (Figure 2; Kollmar, Welz, Straub et al., 2019). The existence of four distinct mouse *SPIRE* proteins which are very similar, but not identical, allows us to speculate that each protein might have a specific function, and that the expression might differ in tissues of distinct functions. Individual expression patterns of *SPIRE* splice variants provide the first insight into the role of these proteins in specific tissues. For this reason, the first step of this work was to unravel the mRNA expression patterns of all *SPIRE* splice variants in distinct mouse tissues by using quantitative real time PCR (qPCR). The highly sensitive qPCR method enables us to determine the absolute mRNA copy numbers, by using a known concentration of a corresponding reference plasmid encoding identical cDNA sequences. The expression levels of the four splice variants showed considerable differences in all tested tissues, with highest *SPIRE* copy numbers in the brain (21692 mRNA copies / 50 ng total RNA; Figure 11). The brain is not only the organ with the highest overall *SPIRE* expression, it is also the main expression tissue for *SPIRE1*. However, the expression of *SPIRE2* in brain (6528 mRNA copies / 50 ng total RNA) was remarkably lower than that of *SPIRE1* (13242 mRNA copies / 50 ng total RNA). Interestingly, the intestine, testicle and the liver showed an overall higher expression of *SPIRE2* compared to the total number of all *SPIRE1* splice variants. The highest amount of *SPIRE2* was measured in testis (12832 mRNA copies / 50 ng total RNA). The liver was the only organ analyzed which does not express *SPIRE1*. All investigated tissues except the kidney and the liver displayed a prominent decrease in *SPIRE1-E9* (1.4 - 8.4 % of total mRNA copies from the *SPIRE1* gene) and *mitoSPIRE1* (4.3 - 18.2 % of total mRNA copies from the *SPIRE1* gene) expression compared to the corresponding amount of *SPIRE1* (78.6 - 92.2 % of total mRNA copies from the *SPIRE1* gene) copy numbers. *mitoSPIRE1* was most highly expressed in the kidney (2453 mRNA copies / 50 ng total RNA, 41 % of total mRNA copies from the *SPIRE1* gene), whereas *SPIRE1-E9* has its expression hot spot in the brain (1266 mRNA copies / 50 ng total RNA, 8.4 % of total mRNA copies from the *SPIRE1* gene). Compared to the expression of *SPIRE1* and *SPIRE2*, we identified only very low expression of *SPIRE1-E9* and the mitochondria associated *mitoSPIRE1* in most organs. In summary, we found *SPIRE1* most highly expressed in the brain, whereas *SPIRE2* shows a high expression in the digestive tract and testis.



C

	<i>SPIRE1</i>	<i>SPIRE1-E9</i>	<i>mitoSPIRE1</i>	<i>SPIRE2</i>
brain	13242 ± 1179 (87.3%)	1266 ± 482 (8.4%)	656 ± 116 (4.3%)	6528 ± 600
spleen	6709 ± 1650 (90.7%)	317 ± 132 (4.3%)	373 ± 74 (5.0%)	3310 ± 185
kidney	3385 ± 2479 (56.5%)	150 ± 102 (2.5%)	2453 ± 218 (41.0%)	4791 ± 224
testis	3028 ± 523 (78.6%)	124 ± 46 (3.2%)	700 ± 118 (18.2%)	12832 ± 937
small intestine	2690 ± 652 (89.0%)	195 ± 89 (6.4%)	139 ± 27 (4.6%)	10246 ± 2074
lung	2390 ± 181 (92.2%)	37 ± 24 (1.4%)	166 ± 26 (6.4%)	2412 ± 62
large intestine	2689 ± 501 (87.9%)	224 ± 113 (7.3%)	147 ± 17 (4.8%)	8897 ± 1062
liver	0 (0%)	194 ± 101 (82.1%)	42 ± 5 (17.9%)	3510 ± 254

Figure 11 - Tissue specific *SPIRE* gene expression. (A) Absolute *SPIRE* mRNA copy numbers in various mouse tissues were determined by quantitative real time PCR employing cDNA preparations from total RNA isolations and presented in a bar diagram. Each bar represents mean mRNA copy numbers of three independent experiments. Cloned cDNAs corresponding to respective genes were used as copy number standards for absolute quantification. *Error bars* represent SEM. n = 3 experimental repeats. (B) Absolute quantification of tissue specific *SPIRE1-E9* and *mitoSPIRE1* mRNA copy numbers is shown in a bar diagram to improve visualization of expression differences. *Error bars* represent SEM. n = 3 experimental repeats. (C) Amount of determined *SPIRE* copy numbers in distinct tissues is shown and the percental distribution of splice variant expression from the *SPIRE1* gene is noted in brackets. Expression analysis of *SPIRE1*, *SPIRE1-E9* was already done in the master thesis. Graph is complemented by the expression pattern of *SPIRE2* and *mitoSPIRE1*. qPCR for *mitoSPIRE1* was done in the master thesis as well, but was repeated here, because the specific *mitoSPIRE1* primer pair used in the master thesis was laying on the same exon. Parts of Figure 11 were already published in Kollmar, Welz, Straub et al., 2019.

3.2 Similar expression patterns of *SPIRE1* and *mitoSPIRE1* in the mouse brain

The previous expression analysis revealed that the actin nucleator *SPIRE* is highest expressed in cells of the brain. In this context, the reported phenotype in fear conditioning experiments of *SPIRE1* mutant mice is most likely associated with neuronal dysfunctions (Pleiser et al., 2014). *MitoSPIRE1* is only expressed at low levels in the mouse brain, but even a low number of *mitoSPIRE1* proteins could significantly influence neuronal functions and neuronal processing of *SPIRE1* mutant mice. For this reason, it is important to know which brain areas (anatomical overview of mouse brains is shown in Figure 12, A) express the *SPIRE1* gene, especially if fear related brain areas express the *mitoSPIRE1* splice variant. *SPIRE1* mRNA was already detected by *in situ* hybridizations in the hippocampus, the dentate gyrus, and the cerebellum (Schumacher et al., 2004; Pleiser et al., 2010). Here we used a *mitoSPIRE1* specific probe (*exon 13* of *SPIRE1*) to localize regions of *mitoSPIRE1* expression by *in situ* hybridization in the mouse brain. A pronounced expression of *mitoSPIRE1* was detected in the hippocampal formation (Figure 12, B). Additional areas, including the cortex, amygdala, and the

hypothalamus, showed weak expression of *mitoSPIRE1* (results not shown). However, because of limited mouse brains and brain slice numbers, these data are very preliminary and await further investigations.

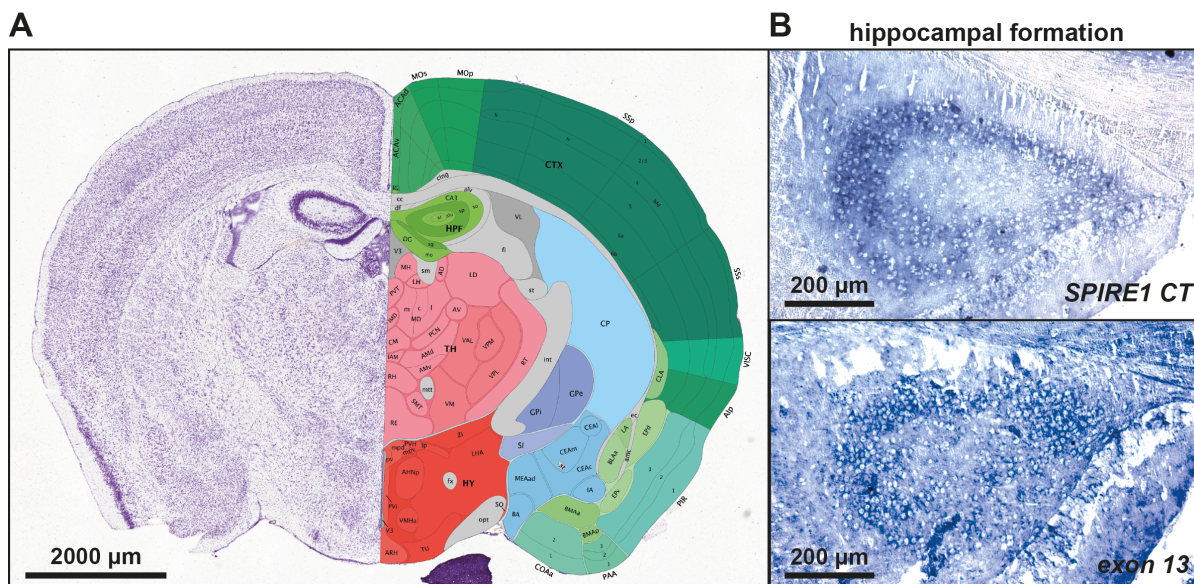


Figure 12 - Brain specific *in situ* hybridization of *mitoSPIRE1*. *SPIRE1* and *mitoSPIRE1* mRNA detection on coronal adult mouse brain sections by *in situ* hybridization using an antisense *SPIRE1 CT* or *mitoSPIRE1* (exon 13) riboprobe. **(A)** Anatomical overview of adult mouse brains visualized by a coronal brain section from the *Allen Mouse Brain Atlas* (The *Allen Mouse Brain Atlas* contains *in situ* hybridization data for approximately 20,000 distinct mouse genes; Mouse, P56, Coronal, image 65 of 132; CTX, cerebral cortex; HPF, hippocampal formation; TH, thalamus; HY, Hypothalamus). Scale bar represents 2000 μm . **(B)** A high hybridization signal for *SPIRE1 CT* (upper panel) and *mitoSPIRE1* (lower panel) was detected in the hippocampal formation. The *SPIRE1 CT* riboprobe detects all *SPIRE1* splice variants and was therefore used as a positive control for specific *mitoSPIRE1* visualization by the *mitoSPIRE1* (exon 13) riboprobe. Scale bar represents 200 μm .

3.3 Subcellular localization of SPIRE proteins

Based on the knowledge that expression of SPIRE isoforms differs in distinct tissues, it was analyzed whether the protein products of each splice variant have specific subcellular localizations as well. It is well characterized that SPIRE proteins are targeted to intracellular membrane structures by the FYVE-type zinc-finger, and that the SPIRE1 and the SPIRE2 protein are located on vesicle membranes (Kerkhoff et al., 2001; Dietrich et al., 2013; Tittel et al., 2015). In addition, a mitochondria-specific localization for mitoSPIRE1 was already described in 2015. The alternatively spliced exon 13 targets the mitoSPIRE1 protein to the outer mitochondrial membrane (Manor et al., 2015). In contrast, a role for the alternatively spliced exon 9 in protein function or subcellular localization has not been described thus far.

Considering the very low expression levels of all four SPIRE isoforms, it is challenging to analyze the intracellular protein localization at endogenous expression levels by staining with specific antibodies. For this reason, subcellular localization and potential colocalizations of all four SPIRE proteins were investigated by transient co-expression of plasmids encoding c-Myc-epitope or GFP tagged SPIRE proteins in HeLa cells. The colocalization of the different SPIRE proteins was analyzed by fluorescence microscopy, and subsequently quantified by determining the Pearson's correlation coefficient (PCC) of the two proteins co-expressed. The PCC indicates the colocalization rate as a statistical measure to unravel a linear correlation between the intensity of different fluorescent signals. Our studies revealed a high correlation for colocalization of SPIRE1 to SPIRE1-E9 and SPIRE2 at vesicular membranes (Figure 13, A). The unique 14 amino acids spanning alternatively spliced exon 9 do not target the splice variant to a specific subcellular localization different from that of SPIRE1. On the contrary, the mitoSPIRE1 protein does not colocalize with vesicular SPIRE1, but does colocalize with mitochondria; as indicated by MitoTracker co-staining (Figure 13, A). The colocalization of tagged proteins was quantified for the indicated co-expressions by determining their PCC using ImageJ as shown in a bar diagram (Figure 13, B). The PCC between SPIRE1 and SPIRE1-E9 or SPIRE2 is significantly higher ($PCC > 0.75$) than the PCC of SPIRE1 / mitoSPIRE1 colocalization (PCC 0.1). Furthermore, valued colocalization between MitoTracker and mitoSPIRE1 (PCC 0.7) has the same tendency as the PCC of SPIRE1 to SPIRE1-E9 or SPIRE2 (PCC 0.75 - 0.9; Figure 13, B).

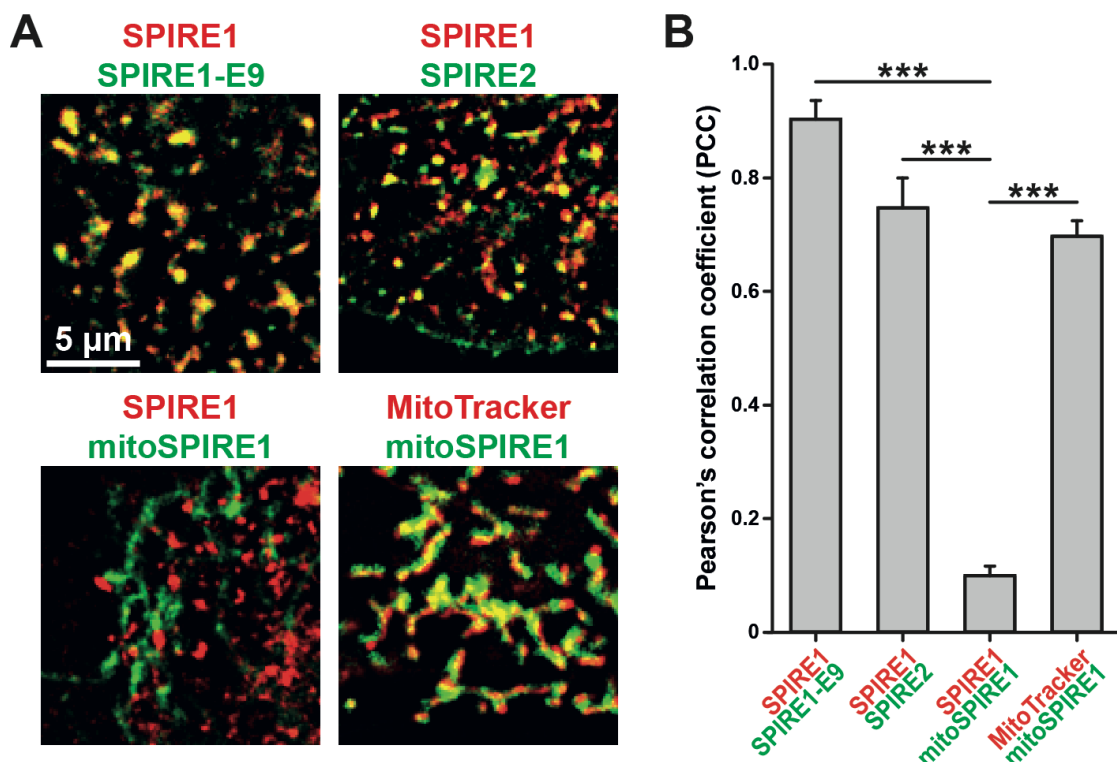


Figure 13 - SPIRE splice variants show different subcellular localization. (A) Myc-epitope (SPIRE1; red) and GFP (AcGFP1; SPIRE1-E9, mitoSPIRE1, SPIRE2; green) tagged SPIRE proteins are transiently co-expressed in HeLa cells. Deconvoluted images show the localization of SPIRE1, SPIRE1-E9 and SPIRE2 at vesicular membranes. mitoSPIRE1 is localized at mitochondria membranes as indicated by the colocalization with a mitochondrial stain (MitoTracker Orange; MitoTracker; red). Colocalization is indicated by overlapping punctae (yellow). Scale bar represents 5 μm . At least 3 cells were recorded for each condition and the channel overlap of one representative cell is presented here. (B) The colocalization of tagged proteins and MitoTracker, respectively, as described in (A) was quantified for the indicated conditions by determining its Pearson's correlation coefficient (PCC) and shown in a bar diagram. Each bar represents the mean PCC value for at least 3 cells analyzed. Error bars represent SEM. One-way ANOVA has been performed; Tukey-Kramer test has been performed as post-hoc analysis: *** = $p < 0.001$. Figure 13 was already published in Kollmar, Welz, Straub et al., 2019.

3.4 Interaction of mitoSPIRE1 with the outer mitochondrial membrane

It is published (Manor et al., 2015) and confirmed by the previous experiment that the unique 58 amino acid spanning alternatively spliced exon 13 of mitoSPIRE1 targets the protein to mitochondria. In the original manuscript of the discovery of mitoSPIRE1, the N-terminus of the mitochondria-localized mitoSPIRE1 protein is described to remain in the cytosol, where it could directly interact with formins to facilitate the actin nucleation processes. On the other hand, published data suggest that the C-terminal end of mitoSPIRE1 reaches into the mitochondrial intermembrane space (IMS) and does not face the cytosol. However, these

experiments are only preliminary (Manor et al., 2015), and as such, it remains unclear if the C-terminal end of mitoSPIRE1 is located in the IMS of mitochondria (Figure 14, A). To identify the localization of the mitoSPIRE1 C-terminus, the following experiment was designed. As a first step, we had a closer look at the predicted secondary protein structure of the alternatively spliced exon 13, analyzed by the online tool PHYRE (<http://www.sbg.bio.ic.ac.uk/phyre2/html/page.cgi?id=index>). The exon 13 is predicted to have two alpha helices separated by a loop structure and could therefore form a hairpin structure which would allow the mitoSPIRE1 C-terminus to be located in the cytosol (Figure 15, A). These findings are only based on a prediction model and do not show reliable structural data. To address the localization of the C-terminal end of mitoSPIRE1, a specific antibody (SA-2133, rabbit polyclonal, Schumacher et al., 2004) against the C-terminal end of SPIRE1 was used (Figure 14, A). As SPIRE proteins are expressed at low levels, it is not possible to specifically stain endogenous SPIRE proteins with this antibody. That is why a GFP tagged mitoSPIRE1 protein in HeLa cells was transiently expressed. Following fixation, HeLa cells were treated with either Triton X-100 or Digitonin to permeabilize membranes for subsequent antibody staining. The unspecific permeabilizer Triton X-100 permeabilizes all membranes of a cell. In contrast, Digitonin specifically targets cholesterol-rich membranes such as the plasma membrane, whereas the mitochondria membranes are not affected due to their low concentration of cholesterol (Figure 14, B and C). A staining of mitoSPIRE1 with the antibody SA-2133 in Digitonin treated cells therefore would indicate that the C-terminal end of mitoSPIRE1 is localized in the cytosol. To be sure that the outer mitochondrial membrane (OMM) is not permeabilized by Digitonin, which would allow the entry of the antibody into the IMS, an antibody staining for cytochrome C was used. The antibody used against cytochrome C targets a part of the cytochrome C protein, which is located in the IMS. Therefore, only if the OMM is permeabilized an antibody staining of cytochrome C is possible. In the experiment, both, Triton X-100- and Digitonin-treated cells show a bright signal for the expressed GFP-mitoSPIRE1, cytochrome C, and the anti-SPIRE1 (SA-2133) antibody staining (Figure 15, B). Triton X-100 and Digitonin permeabilized cells show a high colocalization of GFP tagged mitoSPIRE1 to the anti-SPIRE1 (SA-2133) antibody staining, resulting in the same PCC value (PCC 0.94; Figure 15, B, C (i)). However, Digitonin permeabilized cells show a cytochrome C antibody staining which has a significantly lower colocalization to mitoSPIRE1 (PCC 0.25) than cells treated with Triton X-100 (PCC 0.82; Figure 15, B, C (ii)), which could indicate that the OMM of Digitonin treated cells is still intact. In summary, this experiment

indicates that the C-terminus of mitoSPIRE1 is likely in the cytosol and not in the IMS or the matrix of mitochondria.

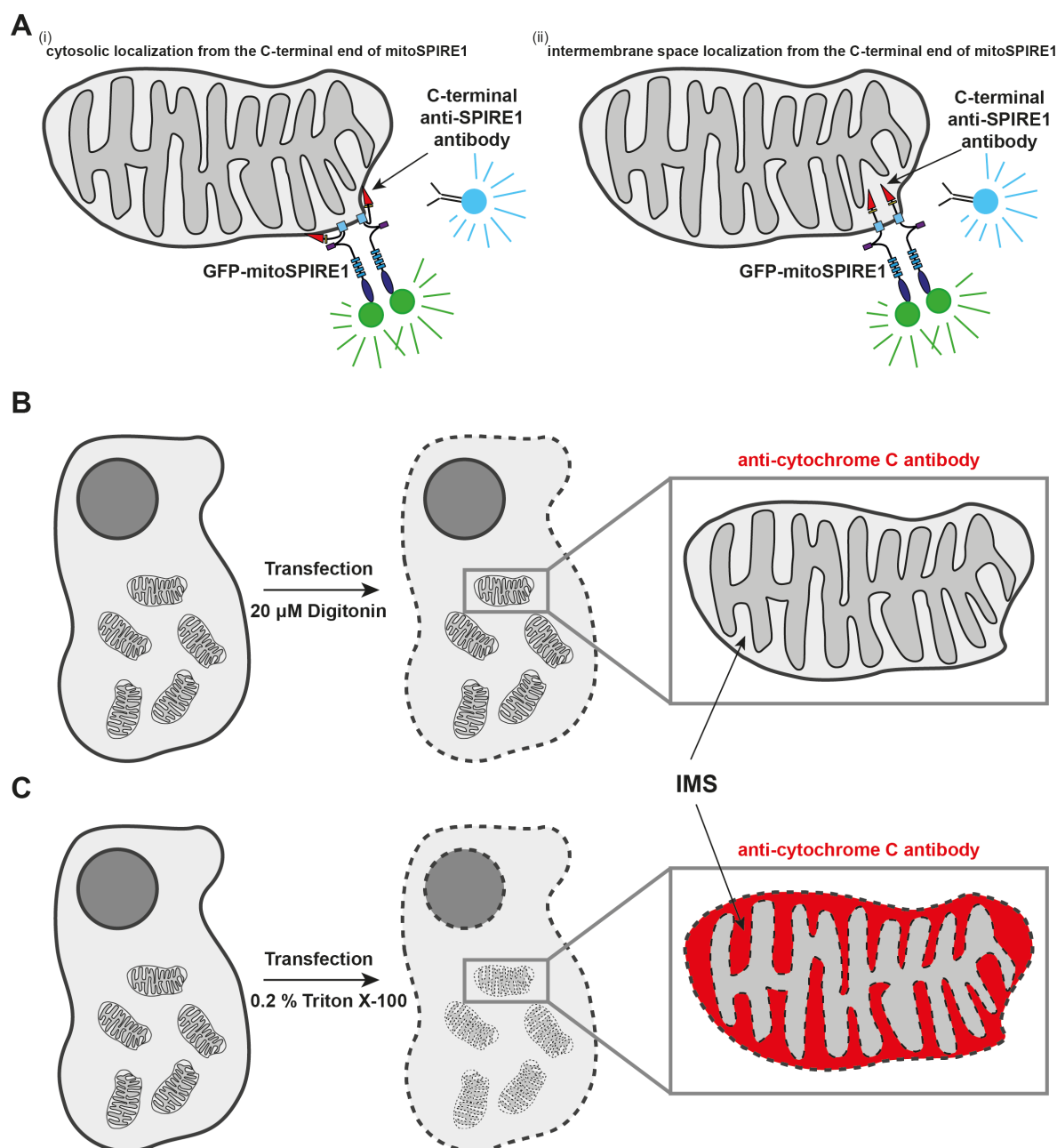


Figure 14 - Experimental setup to determine the localization of the C-terminal end from mitoSPIRE1. To clarify the question if the C-terminal end from mitoSPIRE1 faces the cytosol or localizes in mitochondria an experiment using two different permeabilizers was performed. In this experiment, Digitonin is used after cell fixation to permeabilize cell membrane but not the outer mitochondrial membrane, while Triton X-100 is used to permeabilize the cell membrane and organelle membranes as well. An antibody staining of mitochondrial intermembrane space (IMS) located proteins is therefore only possible when Triton X-100 is used. (A) The C-terminal end of mitoSPIRE1 might localizes in the cytosol (A (i)) or in the mitochondrial IMS (A (ii)). A specific anti-SPIRE1 antibody (C-terminal anti-SPIRE1 antibody, highlighted in *cyan*) is used to report the C-terminal end of expressed GFP tagged mitoSPIRE1 (mitoSPIRE1 has an N-terminal GFP tag (GFP-mitoSPIRE1), highlighted in

green). **(B)** Antibody staining of mitochondria located cytochrome C was used as a control that outer mitochondrial membrane is still intact after Digitonin treatment (mitochondrial outer membrane stays intact after Digitonin treatment and inhibits the entry of antibodies in the IMS, while a staining of IMS located proteins fail, indicated by the light grey color of the IMS). The antibody used against cytochrome C targets a part of the cytochrome C protein, which is located in the IMS. **(C)** In contrast, Triton X-100 treated cells show permeabilized mitochondrial membranes and allow therefore an antibody staining of cytochrome C proteins (indicated by the red color of the IMS). *IMS*, intermembrane space.

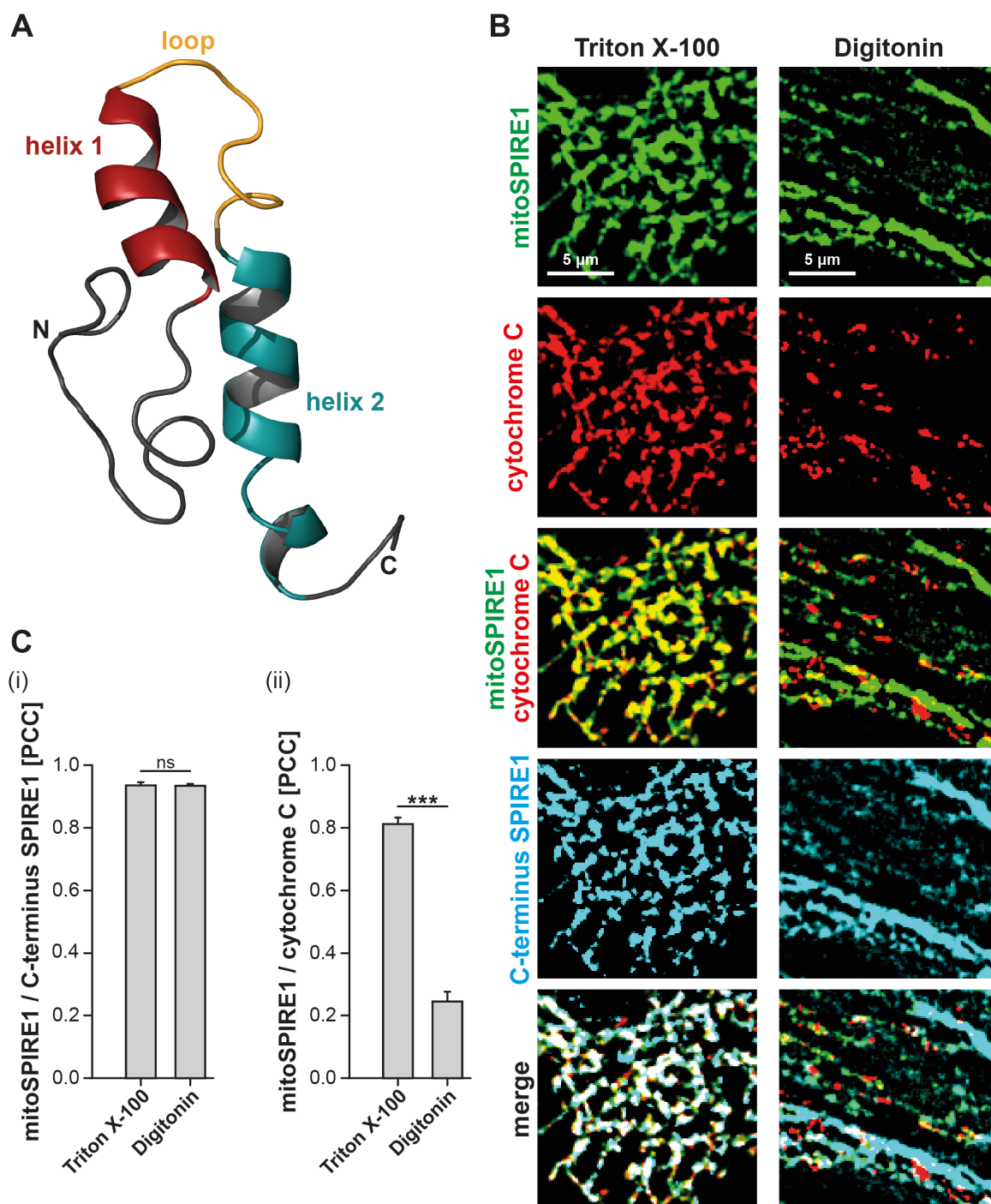


Figure 15 - The C-terminal end of mitoSPIRE1 might be located in the cytosol. Predicted secondary protein structure of the alternatively spliced exon 13 from the *SPIRE1* gene and

specific antibody staining were analyzed to evaluate localization from the C-terminal end of mitoSPIRE1. **(A)** Predicted secondary protein structure of the *SPIRE1* alternatively spliced exon 13. The sequence of 58 amino acids of the alternatively spliced exon 13 from mouse *SPIRE1* was analyzed by the secondary protein structure prediction software PHYRE. The exon 13 is predicted to form two alpha helices (helix 1 highlighted in *red* and helix 2 highlighted in *cyan*) separated by a loop structure (highlighted in *yellow*) and therefore should be able to build a hairpin structure with two transmembrane domains in the mitochondrial outer membrane. N-terminal (N) and C-terminal (C) end of the exon 13 are distinguished. Sequence for exon 13 isolated from XM_006526204.3 (aa: 521 - 578). **(B)** GFP (AcGFP1; mitoSPIRE1, *green*) tagged mitoSPIRE1 proteins are transiently expressed in HeLa cells. Deconvoluted images show the localization of transiently expressed mitoSPIRE1 proteins (*green*) at mitochondria. In addition, the deconvoluted images show an antibody staining of the C-terminal end of mitoSPIRE1 visualized by SA-2133 C-terminal anti-SPIRE1 antibody (*cyan*) and an IMS antibody staining of cytochrome C (*red*; antibody used against cytochrome C targets a part of the cytochrome C protein, which is located in the IMS). Fixed cells were permeabilized for antibody staining by Triton X-100 or by the mild permeabilizer Digitonin. Both, Digitonin and Triton X-100 permeabilized cells show a bright fluorescence signal of mitoSPIRE1 (*green*), cytochrome C (*red*) and the SA-2133 antibody (*cyan*). Comparison of merge pictures from mitoSPIRE1 (*green*) and cytochrome C (*red*) shows colocalization differences between cytochrome C and mitoSPIRE1 within groups of Digitonin and Triton X-100 treated cells. At least 10 cells were recorded for each condition and the channel overlap of one representative cell is presented here. *Scale bar* represents 5 μm . **(C)** The colocalization of GFP tagged mitoSPIRE1 proteins to stained cytochrome C or C-terminal stained SPIRE1 (SA-2133), respectively, as described in (B) was quantified by determining its Pearson's correlation coefficient (PCC) and shown in a bar diagram. Each bar represents the mean PCC value for at least six cells analyzed. **(i)** The PCC for mitoSPIRE1 (*green*) to C-terminal stained SPIRE1 (SA-2133; *cyan*) does not differ between Triton X-100 and Digitonin permeabilized cells. Mann-Whitney-U-test has been performed as post-hoc analysis: ns = not significant. *Error bars* represent SEM. **(ii)** In contrast, Digitonin permeabilized cells show a significantly lower colocalization of cytochrome C (*red*) to mitoSPIRE1 (*green*) than cells permeabilized by Triton X-100. T-test has been performed as post-hoc analysis: *** = $p < 0.001$. *Error bars* represent SEM. These experiments indicate that the C-terminal end of mitoSPIRE1 might localize in the cytosol.

3.5 mitoSPIRE1 targets FMN subfamily formin proteins towards mitochondria

A functional actin nucleator complex on vesicle membranes facilitates microtubule-independent long-range transport of exocytic vesicles (Schuh et al., 2011). In this transport mechanism, the actin nucleator complex is formed by SPIRE1 or SPIRE2 proteins interacting strongly with FMN1 and FMN2 subfamily formins (Pechlivanis et al., 2009; Schuh et al., 2011). The functional complex of SPIRE and FMN benefits from its ability to nucleate and elongate actin filaments (Quinlan and Kerkhoff, 2008; Kerkhoff, 2011). A direct interaction of SPIRE and FMN proteins is mediated by an acid cluster in the N-terminal KIND domain of SPIRE and a basic cluster in the C-terminal FSI sequence of FMN proteins (Pechlivanis et al.,

2009; Zeth et al., 2011). Interestingly, these functional actin nucleator complexes have never been described for mitoSPIRE1 and FMN subfamily proteins.

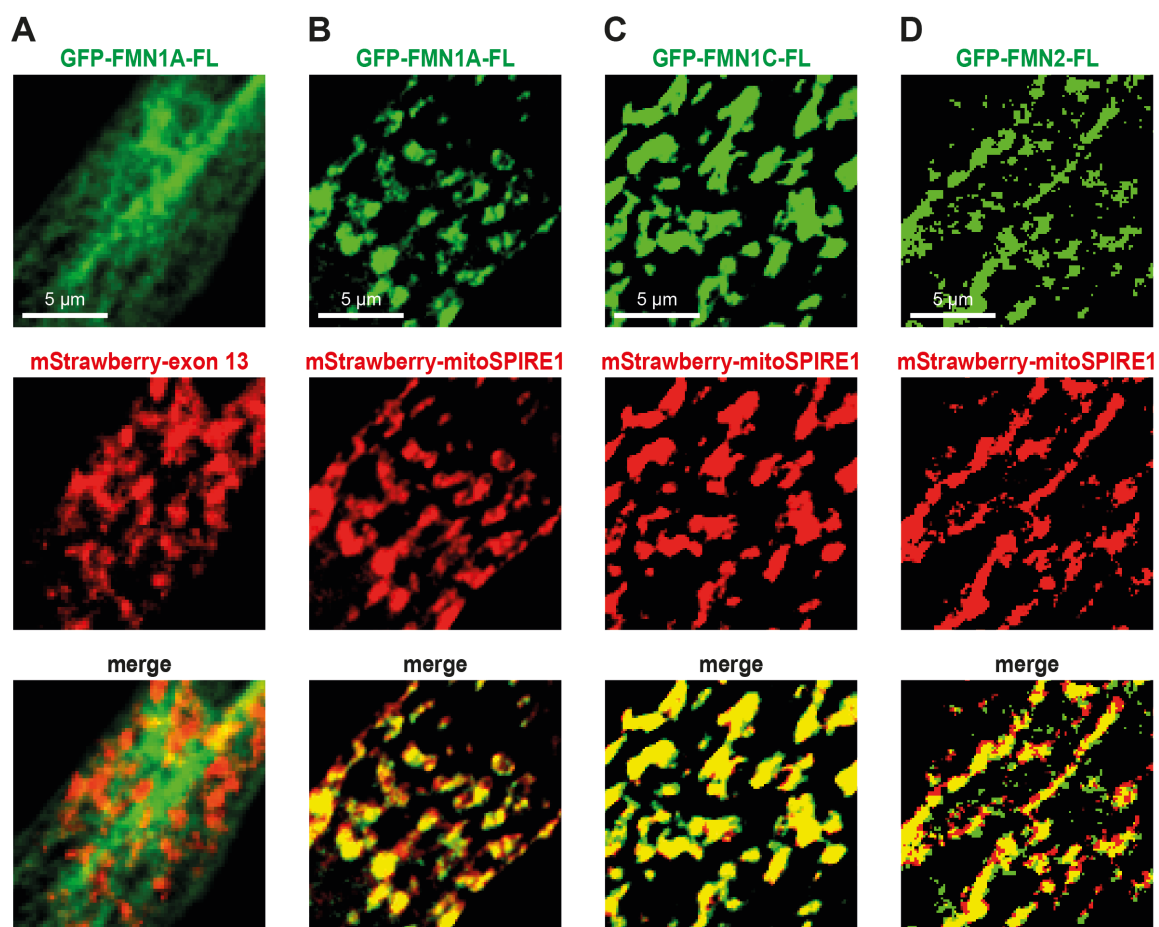
In the following experiments, the potential colocalization of mitoSPIRE1 and formins, including different point and deletion mutants of formins was investigated. Positive colocalization between mitoSPIRE1 and formins at mitochondria would point towards the formation of a functional actin nucleator complex at mitochondrial membranes. Fluorescent protein tagged mitoSPIRE1 (mStrawberry-mitoSPIRE1), SPIRE1 exon 13 (mStrawberry-exon 13), FMN1 (GFP-FMN1A-FL, GFP-FMN1C-FL), FMN2 (GFP-FMN2-FL, GFP-FMN2-FH2-FSI, GFP-FMN2-FH2-C1493, GFP-FMN2-FH2-FSI-K1571A) and Inverted formin 2 (INF2; GFP-INF2-FL-CAAX, GFP-INF2-FL-NonCAAX) proteins are transiently co-expressed in HeLa cells and analyzed by fluorescence microscopy (Figure 16, A-H). The extend of colocalization from co-expressed proteins was quantified by determining the respective Pearson's correlation coefficient (PCC; Figure 16, I-K). Single expression of fluorescent protein tagged FMN1, FMN2 and INF2 proteins each show a distinct subcellular or cytoplasmic localization, but do not localize at mitochondria (results are not shown). Single expression of mStrawberry tagged mitoSPIRE1 and SPIRE1 exon 13 show localization in mitochondria (results are not shown).

All tested FMN1 proteins showed a similar high colocalization with mitoSPIRE1 (PCC 0.9 - 0.91; Figure 16, B, C, I) as GFP-FMN2 proteins containing the FSI (PCC 0.82 - 0.84; Figure 16, D, E, I, K). The transiently co-expressed mStrawberry tagged exon 13 of *SPIRE1* is a mitochondrial marker and does not colocalize with GFP-FMN1A-FL; indicated by a PCC of 0.31 (Figure 16, A, J). In contrast, the mStrawberry tagged mitoSPIRE1 protein has a significantly higher colocalization to co-expressed GFP-FMN1A-FL (PCC 0.9; Figure 16, B, J), which shows that the mitoSPIRE1 protein translocates the GFP-FMN1A-FL towards mitochondria.

The N-terminal fluorescence tagged FMN2-FL or FMN2-FH2-FSI proteins highly colocalize with mitoSPIRE1 at mitochondrial membranes and show a PCC of 0.82 - 0.84 (Figure 16, D, E, I, K). A loss of the functional FSI peptide either by mutation (FMN2-FH2-FSI-K1571A) or truncation (FMN2-FH2-C1493) leads to a rather random colocalization of the affected FMN2 proteins with mitoSPIRE1 (PCC 0.12 - 0.13), and therefore to a significant difference in PCC values to FSI containing FMN2 proteins (Figure 16, E, F, K).

INF2 proteins generally showed a low rate of colocalization with mitoSPIRE1 (PCC 0.18 - 0.29); independent of whether they include the CAAX motif or not (Figure 16, G-I). In this context, the CAAX motif determines the subcellular localization of INF, because the CAAX motif contains a C-terminal prenyl group and is therefore stably bound to the endoplasmic reticulum membrane. The INF2 splice variant without the CAAX motif displays a web-like cytoplasmic appearance that is distinct from the endoplasmic reticulum (Ramabhadran et al., 2011).

In summary, FMN full-length proteins colocalize with mStrawberry-mitoSPIRE1 at mitochondria (PCC 0.84 - 0.91), while FMN2 proteins without a functional FSI motif and INF2 proteins only showed a significantly lower colocalization with mitoSPIRE1 (PCC 0.12 - 0.29; Figure 16).



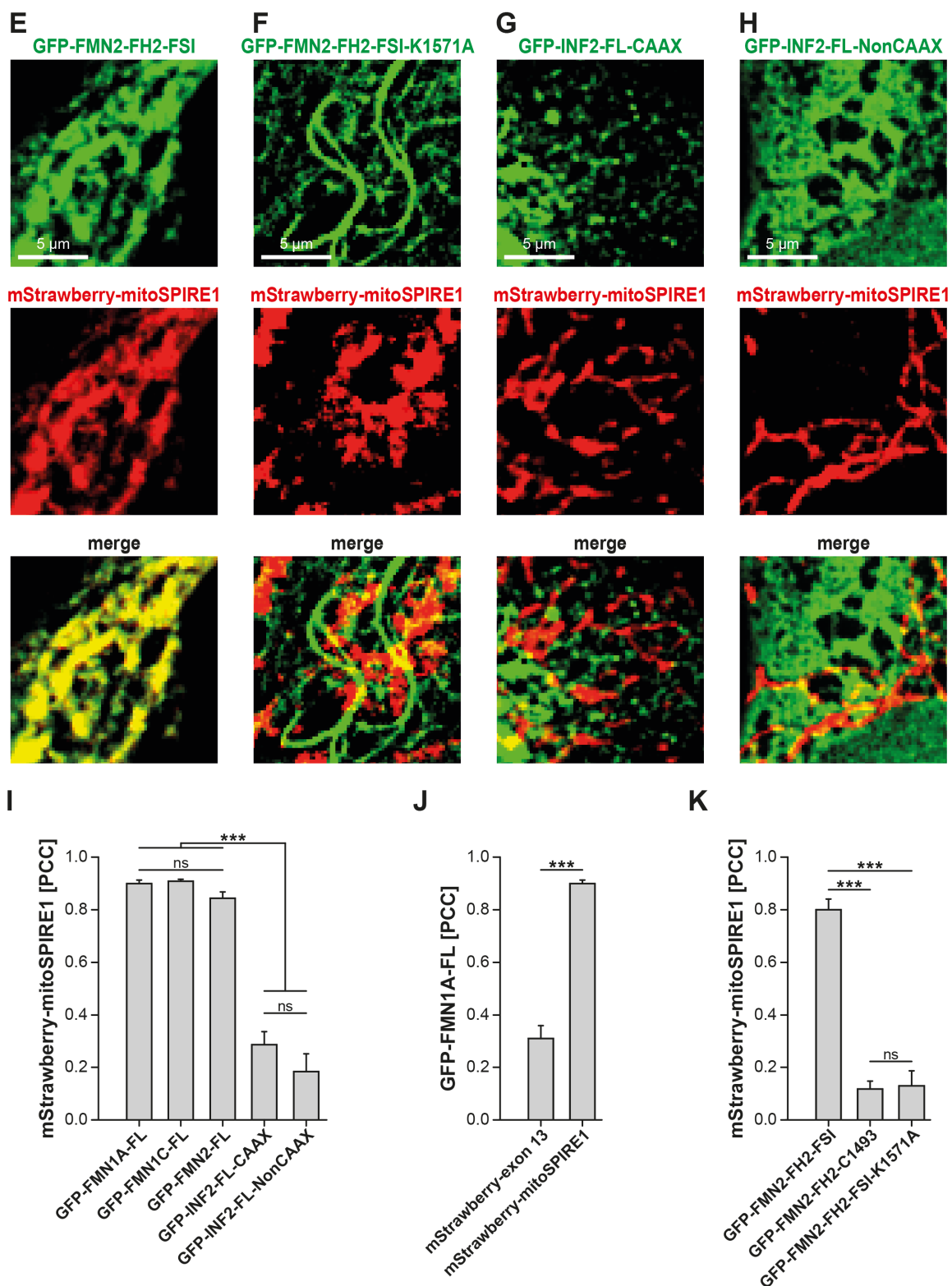


Figure 16 - mitoSPIRE1 colocalizes with formin proteins at mitochondrial membranes. Fluorescent protein tagged mitoSPIRE1 (mStrawberry-mitoSPIRE1), SPIRE1 exon 13 (mStrawberry-exon 13), FMN1 (GFP-FMN1A-FL, GFP-FMN1C-FL), FMN2 (GFP-FMN2-FL, GFP-FMN2-FH2-FSI, GFP-FMN2-FH2-C1493, GFP-FMN2-FH2-FSI-K1571A) and INF2 (GFP-INF2-FL-CAAX, GFP-INF2-FL-NonCAAX) proteins are transiently expressed as well as co-expressed in HeLa cells and analyzed by fluorescence microscopy. (A-H) Deconvoluted images of co-expressed proteins show

representative colocalization of full-length FMN1, FMN2 and INF2 proteins to full-length mitoSPIRE1 (mStrawberry-mitoSPIRE1, *red*) or SPIRE1 exon 13 (mStrawberry-exon 13, *red*). GFP tagged FMN1 (GFP-FMN1A-FL, *green*; GFP-FMN1C-FL, *green*) and GFP tagged FMN2 (GFP-FMN2-FL, *green*) proteins show considerable overlap with mitochondrial mitoSPIRE1 (mStrawberry-mitoSPIRE1, *red*), whereas endoplasmic reticulum and cytoplasmic AcGFP1 tagged INF2 (GFP-INF2-FL-CAAX, *green*; GFP-INF2-FL-NonCAAX, *green*) proteins are almost exclusively localized from mitoSPIRE1. GFP tagged FMN1A (GFP-FMN1A-FL, *green*) does not colocalize with SPIRE1 exon 13 (mStrawberry-exon 13, *red*). *Scale bars* represent 5 μ m; *FL*, full-length. **(I-J)** The colocalization of tagged proteins as described in (A-H) was quantified for the indicated co-expressions by determining their Pearson's correlation coefficient (PCC) as shown in a bar diagram. Each bar represents mean PCC values for at least six cells analyzed, *error bars* represent SEM. **(I)** All FMN full-length (FL) proteins show a significant higher PCC (0.84 - 0.91) to mitoSPIRE1 than INF2 FL proteins (PCC 0.18 - 0.29). **(J)** GFP-FMN1A-FL shows a significant higher colocalization with mitoSPIRE1 than with the exon 13 of *SPIRE1*, which indicates that mitoSPIRE1 translocates GFP-FMN1A-FL towards mitochondria. **(K)** mStrawberry-mitoSPIRE1 was transiently co-expressed with GFP-FMN2-FH2-FSI, GFP-FMN2-FH2-C1493 or GFP-FMN2-FH2-FSI-K1571A and colocalization of tagged proteins was quantified for the indicated co-expressions by determining their Pearson's correlation coefficient (PCC) as shown in a bar diagram. GFP tagged FMN2-FH2-FSI proteins containing the FSI motif show a significant higher PCC (0.82) than FMN2 proteins affected by a loss of the functional FSI peptide either by mutation (FMN2-FH2-FSI-K1571A; PCC 0.13) or truncation (FMN2-FH2-C1493; PCC 0.12), indicating that the FSI motif is necessary for colocalization between mitoSPIRE1 and FMN2 proteins. For I - K One-way ANOVA has been performed; Tukey-Kramer test has been performed as post-hoc analysis: ns = not significant, *** = $p < 0.001$.

3.6 mitoSPIRE1 targets MYO5 actin motor proteins towards mitochondria

Motility of mitochondria is mediated by motor and adapter proteins, which facilitate mitochondrial transport along cytoskeletal components (Hollenbeck and Saxton, 2005). In contrast to mitochondrial transport along microtubules, the molecular transport mechanism mediated by actin filaments and myosin motor proteins has been poorly understood until now. In this respect, it is still unclear how myosin motor proteins are translocated towards mitochondria, and how they influence mitochondrial motility. In 2016, it was reported that SPIRE proteins contain the conserved globular tail domain binding motif (GTBM) which directly interacts with the globular tail domain of myosin 5 (MYO5) motor proteins (Pylypenko, Welz et al., 2016). Since all SPIRE1 proteins contain the GTBM, mitoSPIRE1 could contribute to targeting MYO5 function towards mitochondria. In an initial colocalization study, we co-expressed a GFP tagged C-terminal MYO5A or an mStrawberry tagged MYO5B protein containing coiled-coil regions and a globular tail domain (MYO5A-CC-GTD, MYO5B-CC-GTD) with GFP or mStrawberry tagged isolated SPIRE1 exon 13 or full-length

mitoSPIRE1, respectively. The truncated MYO5 proteins were used, because the expression of MYO5 full-length proteins is only hardly tolerated by cells due to the actin filament binding of the myosin motor domain. The isolated SPIRE1 exon 13 showed a localization at mitochondria but did not show a notable colocalization with MYO5A-CC-GTD (PCC 0.14; Figure 18, A). In contrast, mitoSPIRE1 localized at mitochondria as well and showed a remarkable colocalization with MYO5A-CC-GTD (PCC 0.71; Figure 18, A). MYO5B-CC-GTD colocalized, as did MYO5A, with mitoSPIRE1 but not with the isolated exon 13. In this context, the PCC of MYO5B / mitoSPIRE1 is significantly different from the PCC of MYO5B / exon 13 (results are not shown).

In collaboration with Prof. Dr. Dori Woods and Hannah (Sheehan) Alberico from Northeastern University of Boston, MA, USA, we further analyzed the presence of endogenous MYO5A proteins at the surface of mitochondria from immortalized mouse embryonic fibroblasts by a novel technique called fluorescence-activated mitochondria sorting (FAMS). FAMS is an innovative technique based on the principles of a fluorescence-activated cell sorting (FACS) machine that allows the operator to sort and analyze small organelles like mitochondria. Briefly, a modified FACS cytometer, including a ‘hybrid’ dual-forward scatter mechanism consisting of a photomultiplier tube and a diode, enables the user to distinguish between small particles, debris, and background instrument noise (MacDonald et al., 2019). In our experiment, mitochondria were stained by MitoTracker Red CMXRos (MTR), which enables the identification of mitochondria via flow cytometry by size and positive fluorescence staining. In summary, FAMS facilitates the sorting of mitochondria, in order to analyze mitochondrial size, and to determine the presence of mitochondrial surface molecules by the use of specific fluorophore-conjugated antibodies (Figure 17; MacDonald et al., 2019). Using FAMS with a PE-Cy7 conjugated antibody against MYO5A, we measured the number of MYO5A positive mitochondria from *SPIRE1* mutant and wild type mice. Here, we used immortalized mouse embryonic fibroblasts (iMEFs) of *SPIRE1* mutant mice, which means that iMEFs lack the expression of all functional *SPIRE1* including mitoSPIRE1 proteins, and iMEFs from wild type mice as a control. In this context, iMEFs were generated by immortalization of pMEFs using the SV40 large T-antigen (Andrichke et al., 2016). *SPIRE1* lacking iMEFs of *SPIRE1* mutant mice showed 12.06 % MYO5A positive mitochondria, whereas wild type iMEFs have a significantly higher number of MYO5A positive mitochondria (30.23 % MYO5A positive mitochondria; Figure 18, B (i)). In the corresponding FAMS histogram, PE-Cy7 intensity (horizontal axis) is plotted against the number of mitochondria (vertical axis; Figure 18, B (ii)).

It shows that iMEFs from *SPIRE1* mutant mice have fewer mitochondria with a high PE-Cy7 fluorescence intensity compared to mitochondria from wild type iMEFs. This indicates a function of *SPIRE1* proteins in mitochondrial targeting of MYO5A motor protein function.

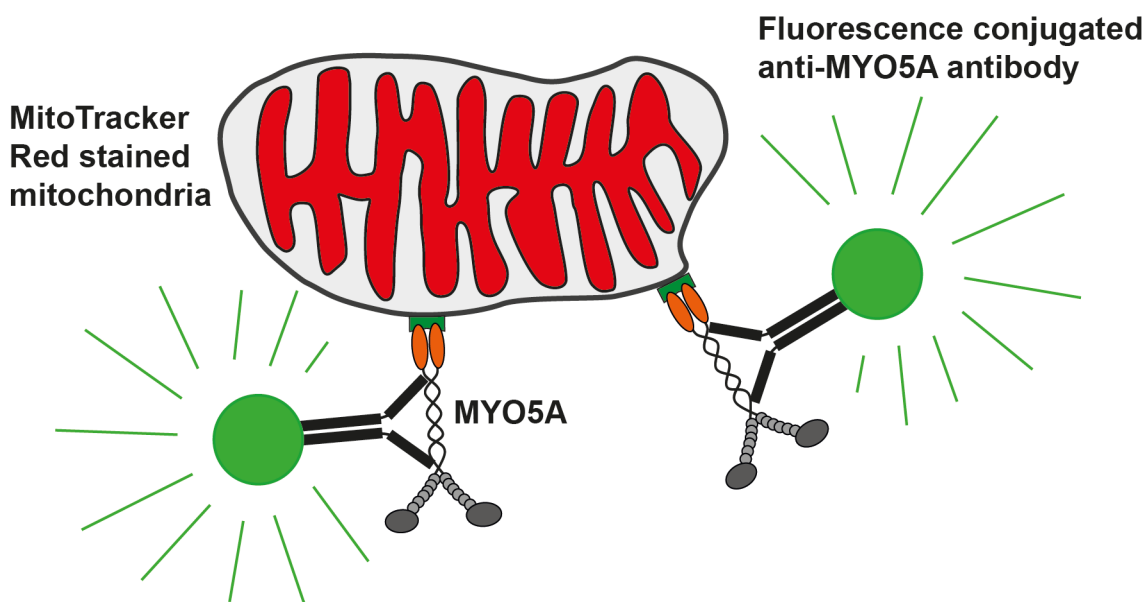


Figure 17 - Number of MYO5A positive mitochondria can be determined by fluorescence conjugated anti-MYO5A antibodies in FAMS. Fluorescence-activated mitochondria sorting (FAMS) is basically used to sort mitochondria, to analyze mitochondrial size and to determine the presence of mitochondrial surface molecules. For these analyzes, a modified fluorescence-activated cell sorting (FACS) machine is used, which is able to distinguish between fluorescence colored organelles and unstained organelles. In addition, the modified FACS machine recognizes surface molecules on fluorescent mitochondria, which are visualized by specific fluorophore conjugated antibodies. In the here presented cartoon mitochondria are stained *red* by MitoTracker Red and MYO5A proteins are visualized by a specific anti-MYO5A antibody conjugated to a *green* fluorescent dye (we used in our experiment PE-Cy7, *deep red*). In this case, the FACS machine enables both to differentiate between mitochondria (*red* signal) and all other unstained organelles and to differentiate between MYO5A positive (*red* and *green* signal) and MYO5A negative (*red* signal only) mitochondria.

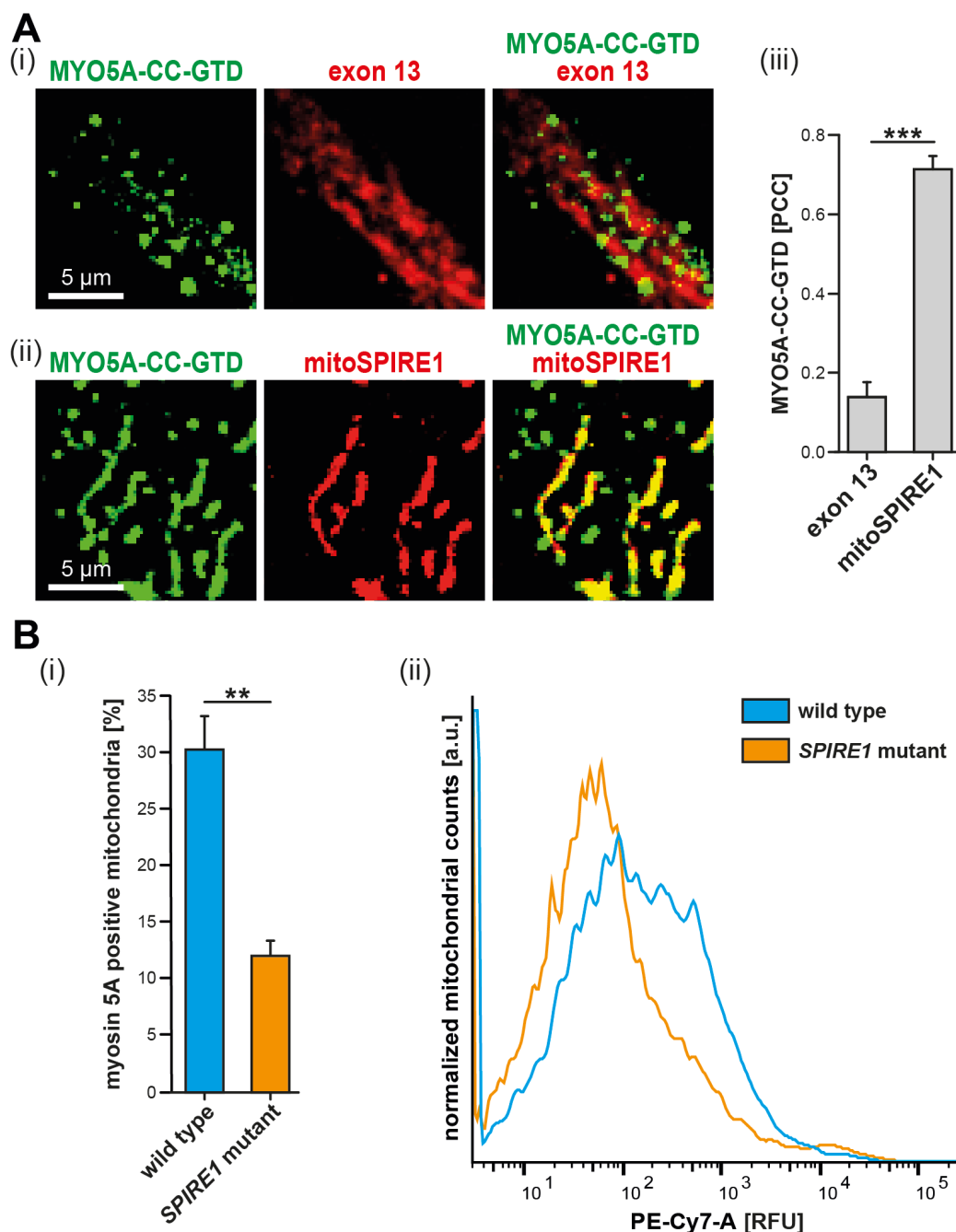


Figure 18 - mitoSPIRE1 targets MYO5 proteins towards mitochondrial membranes. (A) Fluorescently tagged mitoSPIRE1 (mStrawberry-mitoSPIRE1), exon 13 of mitoSPIRE1 (mStrawberry-exon 13) and C-terminal MYO5A (GFP-MYO5A-CC-GTD) proteins are transiently co-expressed in HeLa cells. (i) mStrawberry tagged isolated exon 13 sequences (exon 13, *red*) shows mitochondrial localization as was shown by fluorescence microscopy. In contrast, GFP tagged C-terminal MYO5A proteins containing coiled-coil regions and globular tail domain (MYO5A-CC-GTD, *green*) show a typical vesicular localization as expected and which is distinct from mitochondria. (ii) Co-expression of mStrawberry tagged full-length mitoSPIRE1 (mitoSPIRE1, *red*) and GFP tagged MYO5A-CC-GTD (*green*) proteins show mitochondrial localization of mitoSPIRE1, as expected, and targeting of MYO5A-CC-GTD to mitochondrial membranes in contrast to (i). (iii) The extent of colocalization of MYO5A-CC-GTD with isolated exon 13 and full-length mitoSPIRE1 proteins, respectively, was further quantified by determining the Pearson's correlation coefficient (PCC) as shown in a bar diagram. Each bar represents the mean PCC values for each co-expression, *error bars*

indicate SEM. At least 6 cells were analyzed per condition. T-test has been performed as post-hoc analysis: *** = $p < 0.001$. **(B, (i))** The percentage of myosin 5A positive mitochondria was determined in wild type and *SPIRE1* mutant immortalized mouse embryonic fibroblasts (iMEFs) by fluorescence-activated mitochondria sorting (FAMS). *SPIRE1* mutant iMEFs show significantly fewer MYO5A positive mitochondria compared to mitochondria isolated from wild type iMEFs. MYO5A proteins at the mitochondria surface were marked by staining with specific antibodies which are fluorescently tagged with PE-Cy7. T-test as post-hoc analysis: ** = $p < 0.01$. **(ii)** PE-Cy7 intensity (horizontal axis) against normalized mitochondrial counts (vertical axis) from iMEFs of *SPIRE1* mutant (orange) and wild type (*blue*) mice of the FAMS experiment (B (i)) is plotted in a histogram. The histogram shows that iMEFs from *SPIRE1* mutant mice have fewer mitochondria with a high PE-Cy7 fluorescence intensity compared to mitochondria from wild type iMEFs. This indicates that a reduced number of mitochondria from *SPIRE1* mutant iMEFs have MYO5A on their surface compared to wild type mitochondria. Data are normalized and K-S probability $> 99.9\%$. *RFU*, relative fluorescence units; *a.u.*, arbitrary units.

3.7 Generation of a mitoSPIRE1 knockout mouse model

The previous experiments have shown that mitoSPIRE1 is able to target FMN subfamily formins and MYO5 proteins towards mitochondrial membranes. A complex at vesicle membranes formed by RAB11, MYO5B, SPIRE1, 2 and FMN2 proteins coordinates actin filament nucleation and myosin 5 dependent force generation in vesicle transport processes in mouse oocytes (Schuh et al., 2011; Pylypenko, Welz et al., 2016). Thus, it was intriguing to speculate that a similar protein complex initiated by mitoSPIRE1 might be formed at mitochondrial membranes which could influence mitochondrial dynamics, including mitochondrial transport processes. To address the function of mitoSPIRE1 in more detail at the cellular level, but also at the behavioral level, we looked for an adequate model to study mitoSPIRE1 function. We decided that a knockout mouse model would be the best choice. Previously, in 2014, a murine *SPIRE1* mutant model was generated. Unfortunately, given the gene-trap approach in this mouse knockout model, there is no specific deletion of the mitoSPIRE1 protein, but the expression of all functional SPIRE proteins from the *SPIRE1* gene is inhibited (Pleiser et al., 2014). In this system, it is hard to investigate the specific function of mitoSPIRE1, because a potential effect in *SPIRE1* mutant mice could always be caused by the absence of other vesicular SPIRE isoforms. The *SPIRE1* mutant mouse model is therefore not sufficient to specifically unravel mechanisms of mitoSPIRE1. For this reason, and in collaboration with Prof. Dr. Cord Brakebusch and Dr. Javier Martín Gonzalez from the University of Copenhagen, we generated a mouse model that specifically lacks the expression of mitoSPIRE1 without affecting the expression of SPIRE1 and SPIRE1-E9 - the mitoSPIRE1 knockout mouse. The mitoSPIRE1 knockout mouse was generated in embryonal stem cells of

a C57BL/6N mouse background by the use of the CRISPR / Cas9 gene editing technology. Two targeting constructs have been designed to knockout the *exon 13* of the *SPIRE1* gene, each containing a *SPIRE1 exon 13* flanking guide RNA (gRNA) and the Cas9 nuclease protein. The two flanking gRNAs are highlighted in *red* of Figure 19, and direct the nuclease Cas9 to two distinct locations that are located directly before and after *exon 13* of the *SPIRE1* gene. Cas9 activity results in a double strand break at the gRNA defined regions and results consequently in the loss of the genomic *SPIRE1 exon 13* sequence (Figure 19). The DNA double-strand breaks are fixed by the DNA repair mechanisms of the cell. We confirmed the loss of *exon 13*, both at the genomic DNA level and at the mRNA level, using specific primer pairs (Figure 19, B (i) and (ii)). In detail, we used a primer pair starting in the *SPIRE1 intron 12* and ending in the belonging *intron 13* sequence to confirm the absence of genomic *SPIRE1 exon 13*. If *exon 13* is included in the *SPIRE1* gene, the mentioned primer pair, when used in a PCR reaction and analyzed by gel electrophoresis, a band of 749 base pairs is generated, as was shown for the homozygous and heterozygous wild type controls (Figure 19, B (i)). In contrast, the specific primer pairs generate a 575 base pair DNA fragment when *exon 13* is absent, like it is shown for the mitoSPIRE1 knockout and the heterozygous wild type control (Figure 19, B (i)). The absence of SPIRE1 exon 13 encoding mRNA was confirmed by two specific primer pairs. The first primer pair binds specifically to *exon 8* and *exon 13* of *SPIRE1* and generates only a 687 base pair PCR fragment from cDNA preparations if the *exon 13* exists, as is shown for wild type controls (Figure 19, B (ii)). The second primer flanks the *exon 13* of *SPIRE1* by specifically binding to *exon 12* and *exon 14*. A PCR product band from cDNA preparations is therefore generated in both the absence and presence of *exon 13*, but the PCR products differ in size. Here, the presence of *exon 13* generates a 295 base pair fragment, while the absence of *exon 13* produces a shorter 121 base pair long PCR-product. Our gene expression analysis confirmed a specific loss of the *exon 13* transcript in mitoSPIRE1 knockout mice (Figure 19, B (ii)). We were not able to test whether the mitoSPIRE1 protein is absent, as there is no specific mitoSPIRE1 antibody to distinguish between the different SPIRE isoforms from the *SPIRE1* gene. However, by means of GST-pulldown assays from primary mouse embryonic fibroblasts using a mouse GST tagged FMN2-eFSI peptide (GST-FMN2-eFSI) and GST as control, we confirmed that SPIRE proteins from the *SPIRE1* gene are still translated in mitoSPIRE1 knockout mice at similar levels compared to wild type mice (Figure 19, B (iii)).

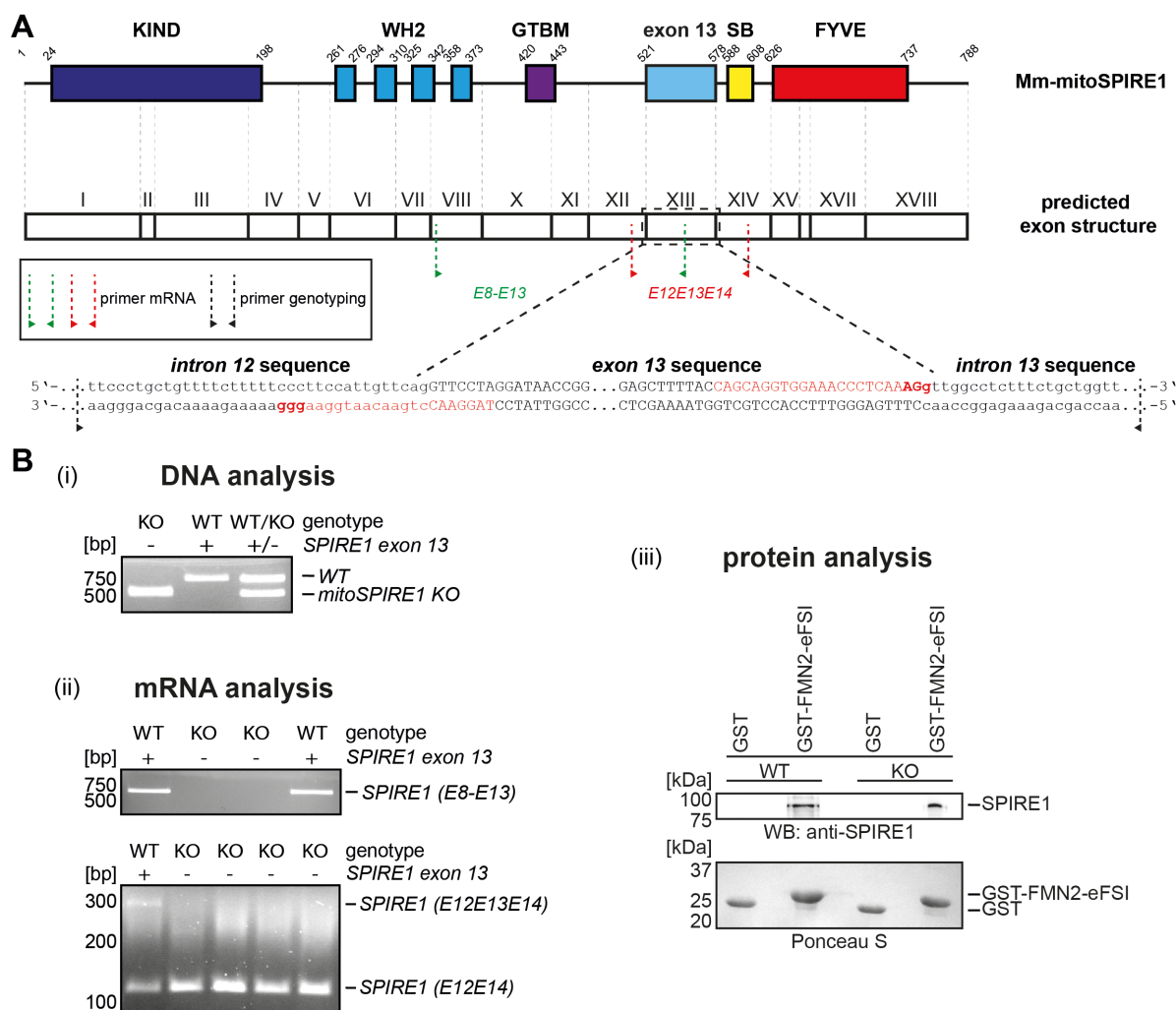


Figure 19 - Generation of the mitoSPIRE1 knockout mouse. (A) Schematic representation of the mouse mitoSPIRE1 protein domains and the respective predicted exon structure. Numbers on the protein structure indicate amino acid boundaries. The genomic *exon 13* DNA sequence is shown (capital letters) as well as the surrounding intron sequences (lowercase letters). We have generated the mitoSPIRE1 knockout (mitoSPIRE1 KO) mice by using the CRISPR / Cas9 gene editing technology. Selected guide RNAs to direct the Cas9 nuclease to the genomic region of interest are highlighted in red. Primer which are used to verify the exclusion of *exon 13* at DNA and mRNA level are illustrated as dotted arrows (DNA primer = black, mRNA primer = green and red). *KIND*, kinase non-catalytic C-lobe domain; *WH2*, Wiskott-Aldrich-Syndrome protein homology 2; *GTBM*, globular tail domain binding motif; *SB*, SPIRE-box; *FYVE*, FYVE-type zinc-finger; *Mm*, Mus musculus. (B) Analysis of genomic *SPIRE1* *exon 13* presence as well as mRNA and protein expression in mitoSPIRE1 KO mice. (i) Absence of genomic *SPIRE1* *exon 13* in mitoSPIRE1 KO mice was confirmed by PCR analysis using genotyping primer (black dotted arrow, (A)). DNA of wild type mice was used as a control. (ii) PCR analysis of cDNA preparations from wild type and mitoSPIRE1 KO primary embryonic fibroblasts (pMEFs) reveals the absence of the alternatively spliced *exon 13* at mRNA levels. Two different primer pairs were used (red and green dotted arrows as in (A) for PCR fragments *SPIRE1* (E8-E13) and *SPIRE1* (E12E13E14), respectively). (iii) The expression of SPIRE proteins from the *SPIRE1* gene in wild type and mitoSPIRE1 KO pMEFs was confirmed by a GST-pulldown assay with purified GST-mm-FMN2-eFSI (GST-FMN2-eFSI) from pMEF cell lysates. mitoSPIRE1 KO pMEFs specifically lack the expression of alternatively spliced *SPIRE1* *exon 13* but still express SPIRE proteins from the

SPIRE1 gene. GST was used as control and Ponceau S staining shows equal amounts of GST tagged proteins. *WT*, wild type; *KO*, mitoSPIRE1 knockout; *WB*, Western blotting.

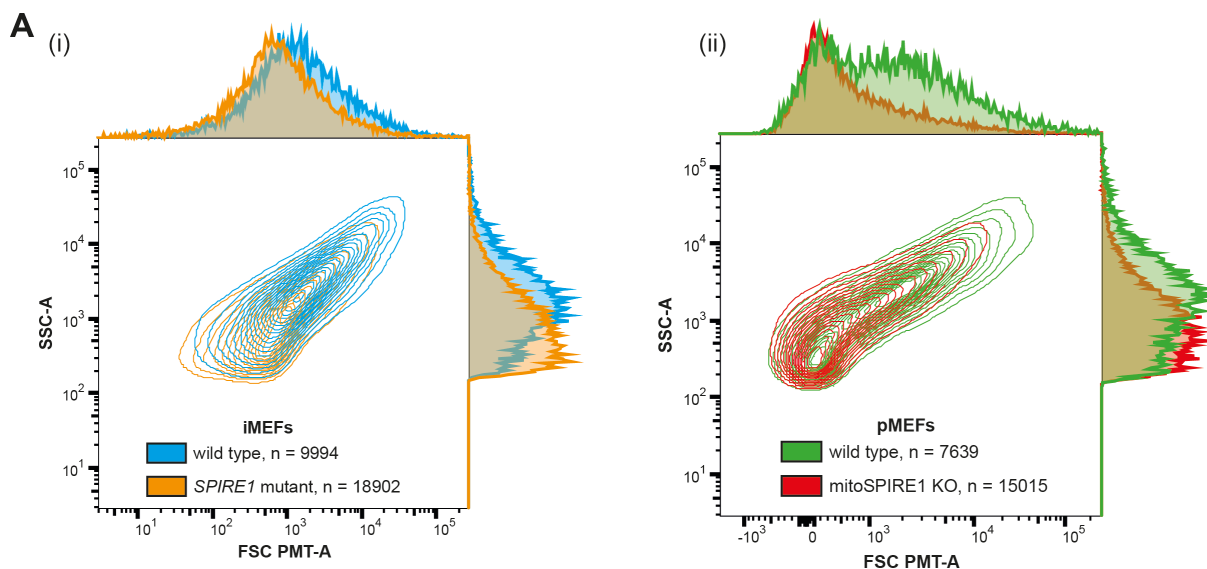
3.8 Mitochondria integrity in mouse SPIRE knockout models

In general, mitochondria are highly dynamic organelles which divide, fuse and move to distinct intracellular regions where they provide energy in the form of ATP. The dynamics and the function of these highly complex organelles are regulated and affected by a multitude of different intra- and extracellular factors (Chen and Chan, 2009; Sheng, 2014). In this respect, a huge number of proteins are known to affect mitochondrial dynamics. One of these proteins is the actin nucleator protein mitoSPIRE1 which is located at the mitochondrial outer membrane and influences mitochondrial dynamics (Manor et al., 2015). By the use of our novel mitoSPIRE1 knockout mouse model, we investigated the influence of the absence of mitoSPIRE1 on mitochondrial integrity, including mitochondrial morphology, functionality, and motility.

3.8.1 Influence of SPIRE absence on mitochondrial morphology

Mitochondrial morphology is mainly regulated by the balance between the dynamic processes of mitochondrial fission and fusion. An unbalanced number of fission and fusion events causes fragmented or elongated mitochondria and can therefore influence the functional integrity of these organelles. Dysfunctional mitochondria often lead to cellular dysfunctions and can cause severe consequences for the whole organism (Chen and Chan, 2009; van der Blik et al., 2013). It is reported that fission processes are not only dependent on several regulatory proteins, but also from the actin cytoskeleton (Korobova et al., 2013, 2014; Hatch et al., 2014; Li et al., 2015). As a consequence, we asked if mitoSPIRE1 serves as an actin nucleator in mitochondrial fission processes, and if mitochondrial morphology is changed as a result of mitoSPIRE1 absence. We therefore had a closer examination of the mitochondrial morphology. In the following experiments, we determined mitochondrial morphology of wild type, *SPIRE1* mutant and mitoSPIRE1 knockout mouse embryonic fibroblasts by fluorescence-activated mitochondria sorting (FAMS) and live cell fluorescence microscopy (Figure 20). Mitochondria morphology was measured in a 3-dimensional approach by forward scatter photomultiplier tube (FSC PMT) and side scatter (SSC) by FAMS and was done in collaboration with Prof. Dr. Dori Woods and Hannah (Sheehan) Alberico at Northeastern University in Boston. The flow

cytometry approach allowed us to analyze a high number of mitochondria from wild type and *SPIRE1* mutant immortalized mouse embryonic fibroblasts (iMEFs). These data showed that iMEFs without SPIRE proteins from the *SPIRE1* gene had an overall higher number of small mitochondria, and a lower number of large mitochondria compared to the wild type cells (Figure 20, A (i)). The same morphological phenotype was detected for mitochondria of mitoSPIRE1 knockout primary mouse embryonic fibroblasts (pMEFs) compared to control mitochondria from wild type pMEFs (Figure 20, A (ii)). In addition, the average length measured from 2-dimensional fluorescence microscopy pictures of MitoTracker Orange stained mitochondria from *SPIRE1* mutant and mitoSPIRE1 knockout pMEFs revealed a significant difference compared to the length of wild type mitochondria. In this context, wild type mitochondria show an average length of 3.07 μm , while the length of *SPIRE1* mutant (1.89 μm) and mitoSPIRE1 knockout mitochondria (1.62 μm) is significantly reduced (Figure 20, B). Interestingly, cells of all investigated mouse lines contain elongated, normal and fragmented mitochondria (Figure 20, C).



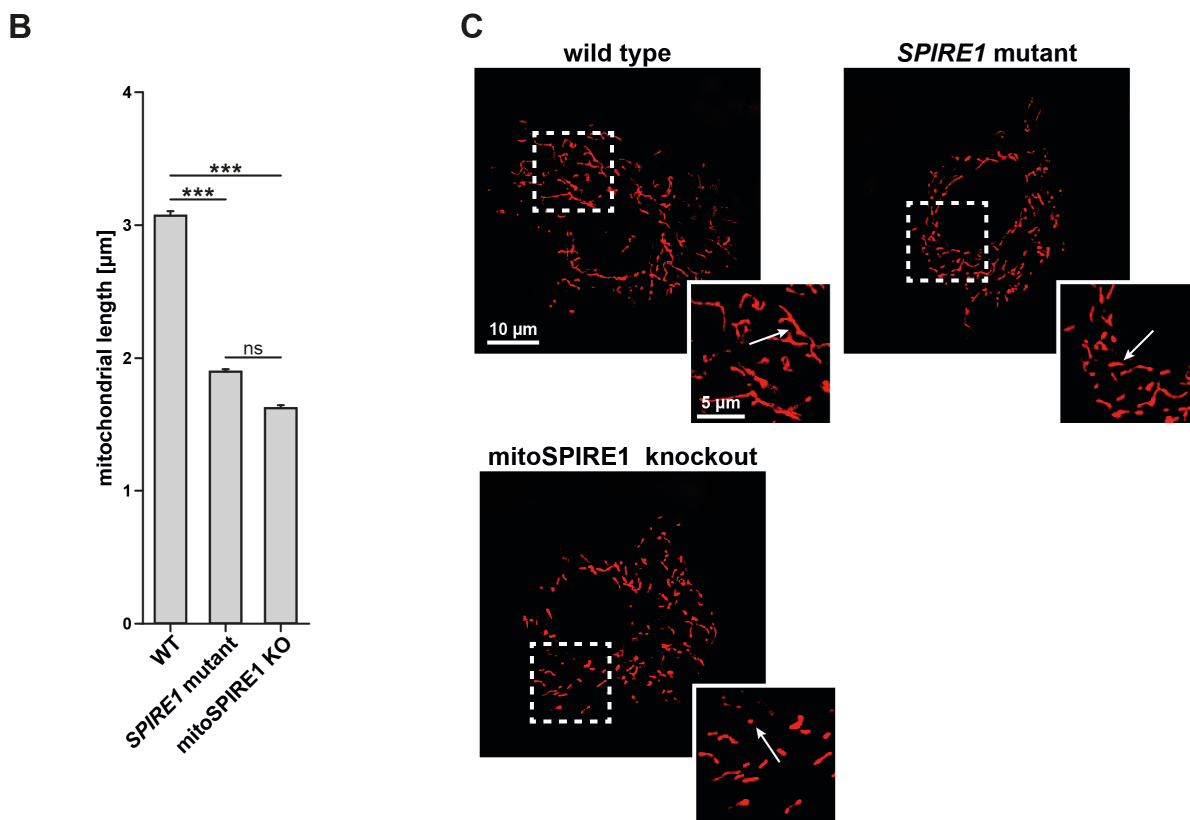


Figure 20 - mitoSPIRE1 regulates mitochondria size in mouse fibroblasts. (A) Size analysis of MitoTracker Red CMXRos stained mitochondria by fluorescence-activated mitochondria sorting (FAMS) of immortalized mouse embryonic fibroblasts (iMEFs; (i)) and primary mouse embryonic fibroblasts (pMEFs; (ii)). Fibroblasts are isolated from wild type mice, *SPIRE1* mutant mice lacking both, expression of vesicular and mitochondrial SPIRE1 proteins and mitoSPIRE1 knockout mice lacking only mitochondrial mitoSPIRE1. Forward scatter photomultiplier tube area (FSC PMT-A) and the more sensitive side scatter area (SSC-A) are used to determine mitochondria size. Both, *SPIRE1* mutant iMEFs (*orange*) (i) and mitoSPIRE1 KO pMEFs (*red*) (ii) show a higher number of small mitochondria and a lower number of large mitochondria than cell specific wild type controls (*blue* and *green*). Data shown represent one out of three experimental repeats (results of experimental repeats were similar). *n* indicates number of sorted mitochondria. **(B)** The length of MitoTracker Orange stained mitochondria was quantified for living pMEFs isolated from wild type ($n = 85$), *SPIRE1* mutant ($n = 160$) and mitoSPIRE1 KO ($n = 18$) mice. The mean mitochondrial length is shown in a bar diagram. Error bars represent SEM. One-way ANOVA has been performed; a significant difference between species was detected; proofed effect size ($\eta^2 = 0.056$); Mann-Whitney-U-test has been performed as post-hoc analysis: ns = not significant, *** = $p < 0.001$. **(C)** Representative pMEF cells with MitoTracker Orange stained mitochondria reveal differences in mitochondrial length between wild type, *SPIRE1* mutant and mitoSPIRE1 KO pMEFs as including long (arrow first panel), short (arrow second panel) and fragmented (arrow third panel) mitochondria as shown by fluorescence microscopy.

3.8.2 Influence of *SPIRE1* absence on mitochondrial respiration

As already described above, the functional integrity of mitochondria is essential for cellular homeostasis, and therefore, mitochondrial dysfunction can cause severe diseases (Chen and Chan, 2009). For this reason, we investigated the mitochondrial functionality of *SPIRE1* mutant cells by staining mitochondria with the cell-permeable dye tetramethylrhodamine-methylester (TMRM). TMRM accumulates in active mitochondria with an intact membrane potential and thus, shows a bright signal in healthy cells with functional mitochondria. In contrast, non-functional mitochondria often have a loss of their membrane potential, and therefore TMRM accumulation is inhibited leading to a decreased or abolished fluorescence signal. Mitochondria of both *SPIRE1* mutant cells and wild type pMEFs showed a bright TMRM signal. The TMRM staining was shown to be independent of mitochondrial morphology and was thus observed in both fragmented and tubular mitochondria of *SPIRE1* mutant and wild type pMEFs (Figure 21, A). In order to obtain additional information about the mitochondrial function in *SPIRE1* lacking cells, we analyzed these organelles in a specific stress test. For this purpose, we used a *Seahorse Mito Stress Test* assay in which mitochondria are treated with different bioenergetic modulators to trigger functional mitochondrial reactions. The induced mitochondrial reactions consume a specific amount of oxygen which can be measured as oxygen consumption rate (OCR) by the *Seahorse Analyzer*. In the mentioned *Mito Stress Test* assay pMEFs of *SPIRE1* mutant and wild type mice were successively treated with oligomycin, carbonilcyanide p-triflouromethoxyphenylhydrazone (FCCP) and antimycin A / rotenone. Oligomycin blocks the proton channel of the ATP synthase, thus the mitochondrial proton gradient cannot be degraded. As a consequence of oligomycin treatment the mitochondrial ATP production-related OCR can be determined. In contrast, FCCP uncouples the oxidative phosphorylation (OXPHOS) by collapsing the mitochondrial proton gradient resulting in a maximal OCR of complex IV. The bioenergetic modulators antimycin A and rotenone shut down the OXPHOS by blocking complex III (blocked by antimycin A) and complex I (blocked by rotenone) of the electron transport chain. The treatment of mitochondria with the mentioned bioenergetic modulators determined the OCR of mitochondrial basal respiration, ATP-linked respiration, maximal respiration and further parameters. None of the treatments resulted in a significant difference of OCR between wild type and *SPIRE1* mutant mitochondria (Figure 21, B).

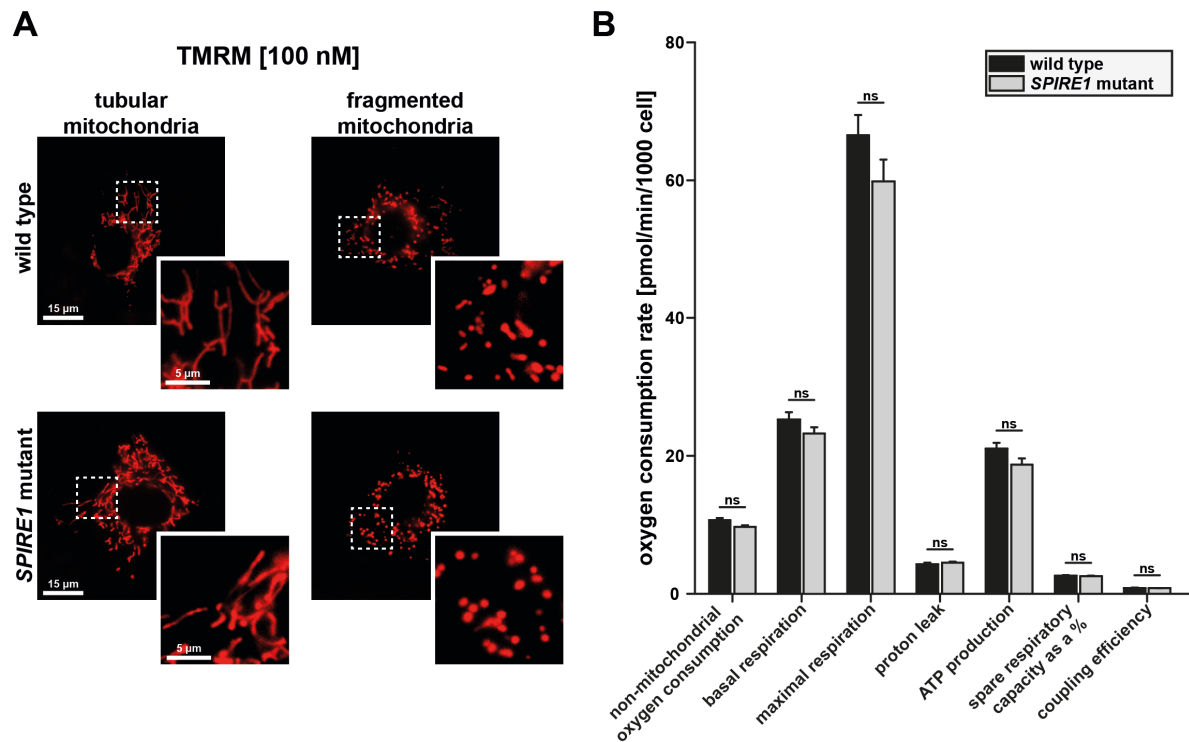


Figure 21 - Absence of mitoSPIRE1 does not influence mitochondrial respiration rate in response to bioenergetic modulators. (A) Tetramethylrhodamine-methylester (TMRM) stained mitochondria of wild type and *SPIRE1* mutant pMEFs are shown. TMRM accumulates in active mitochondria with intact membrane potentials and indicates healthy mitochondria. There was no detectable difference between stained mitochondria of wild type and *SPIRE1* mutant pMEFs. Both cell types contain both, tubular and fragmented mitochondria, which are both active and intact. *Scale bar* represents 15 µm and 5 µm (insets). (B) A bar diagram shows the oxygen consumption rate (OCR) which was measured using a *Seahorse XFp Flux Analyzer* with the Mito Stress Test kit under following conditions: Primary MEFs (pMEFs) from wild type and *SPIRE1* mutant mice were successively treated with oligomycin, carbonyl cyanide-p-trifluoromethoxyphenylhydrazone (FCCP) and antimycin A / rotenone. Oligomycin inhibits oxygen consumption rate of mitochondria by blocking the ATP synthase, while FCCP stimulates mitochondrial respiration to its maximum by uncoupling the electron transport chain. Antimycin A and rotenone are shutting down oxidative phosphorylation completely by blocking complex III and complex I of the electron transport chain. None of the treatments resulted in a significant difference in OCR between wild type and *SPIRE1* mutant mitochondria. The non-mitochondrial oxygen consumption didn't show any differences between groups as well. Each bar represents mean values, *error bars* represent SEM. with $n = 4$ experimental repeats. One-way ANOVA has been performed, no significant differences were found, ns = not significant.

3.8.3 Function of mitoSPIRE1 in mitochondrial motility

Intracellular trafficking of different cargo is an essential mechanism to establish cell function, morphology and polarization, as well as for the sophisticated communication within animal cells. Dysfunctions in specific intracellular transport systems can cause severe diseases like

spastic paraplegia (mutated KIF5A; Chevalier-Larsen and Holzbaur, 2006), or the Griscelli syndrome (Huizing et al., 2008). In general, the movement of cargo in animal cells is organized along microtubules and actin filament tracks, and driven by distinct motor proteins (Rogers et al., 2000). In mouse oocytes, SPIRE proteins are recruited to RAB11 vesicles and interact with the FMN2 subfamily formin in nucleating actin filaments at the surface of RAB11 vesicle membranes in order to generate an oocytic actin meshwork. This actin meshwork is used by MYO5B actin motor proteins to drive an actin dependent long-range transport of RAB11 vesicles towards the oocyte cortex (Schuh et al., 2011). In a similar mechanism, RAB27A is reported to recruit SPIRE1 to melanosomes in melanocytes to organize an actin nucleator complex with FMN1. The resulting cytoplasmic actin mesh subsequently facilitates an MYO5A dependent peripheral melanosome transport in mouse melanocytes (Alzahofi, Robinson, Welz et al., 2018).

SPIRE, myosin 5, and FMN proteins interact and regulate local actin / myosin networks at vesicle membranes. Based on the previous experiments, we know that mitoSPIRE1 is able to colocalize with FMN formins and with MYO5 motor proteins at the outer mitochondrial membrane. As a consequence, we asked if the cooperation of SPIRE / MYO5 / FMN proteins at membranes is a conserved mechanism, and mitoSPIRE1 influences the transport of mitochondria. We therefore analyzed the motility of mitochondria in primary mouse embryonic fibroblasts (pMEFs) of *SPIRE1* mutant, mitoSPIRE1 knockout and wild type mice by live cell fluorescence microscopy. To measure distinct parameters of single mitochondrial movements, we used IMARIS software with a custom particle tracking-mask. IMARIS tracked the motility of each MitoTracker Orange stained mitochondrion over time and analyzed associated track parameters (Figure 22, B). We defined *moving mitochondria* as mitochondria which cover a distance greater than 4 μm per 20 seconds. Figure 22, A presents that pMEFs of wild type mice showed a significantly lower number of moving mitochondria per 20 seconds compared to mitochondria without mitoSPIRE1. In more detail, wild type pMEFs showed 1.56 %, *SPIRE1* mutant pMEFs 3.12 % and mitoSPIRE1 knockout 3.38 % moving mitochondria per time interval (Figure 22, A (i)). In addition, wild type mitochondria showed shorter average track lengths of moving mitochondria (5.42 μm) than mitoSPIRE1 deficient mitochondria (6.09 - 6.12 μm ; Figure 22, A (ii)). Furthermore, the maximal track length of mitoSPIRE1 deficient motile mitochondria (10.89 - 12.46 μm) was significantly higher compared to the wild type, with a maximal track length of 7.36 μm (Figure 22, A (iii)). In line with this, the mitoSPIRE1 deficient mitochondria showed a significant increase in the maximal velocity

(0.96 - 1.04 $\mu\text{m/s}$) compared to mitochondria from wild type pMEFs (0.85 $\mu\text{m/s}$; Figure 22, A (iv)). As a summary, mitoSPIRE1 deficient pMEFs of *SPIRE1* mutant and mitoSPIRE1 knockout mice do not show any significant differences in measured parameters of mitochondria motility between each other, but they show in all measured parameters mitochondria with increased motility compared to the wild type control (Figure 22).

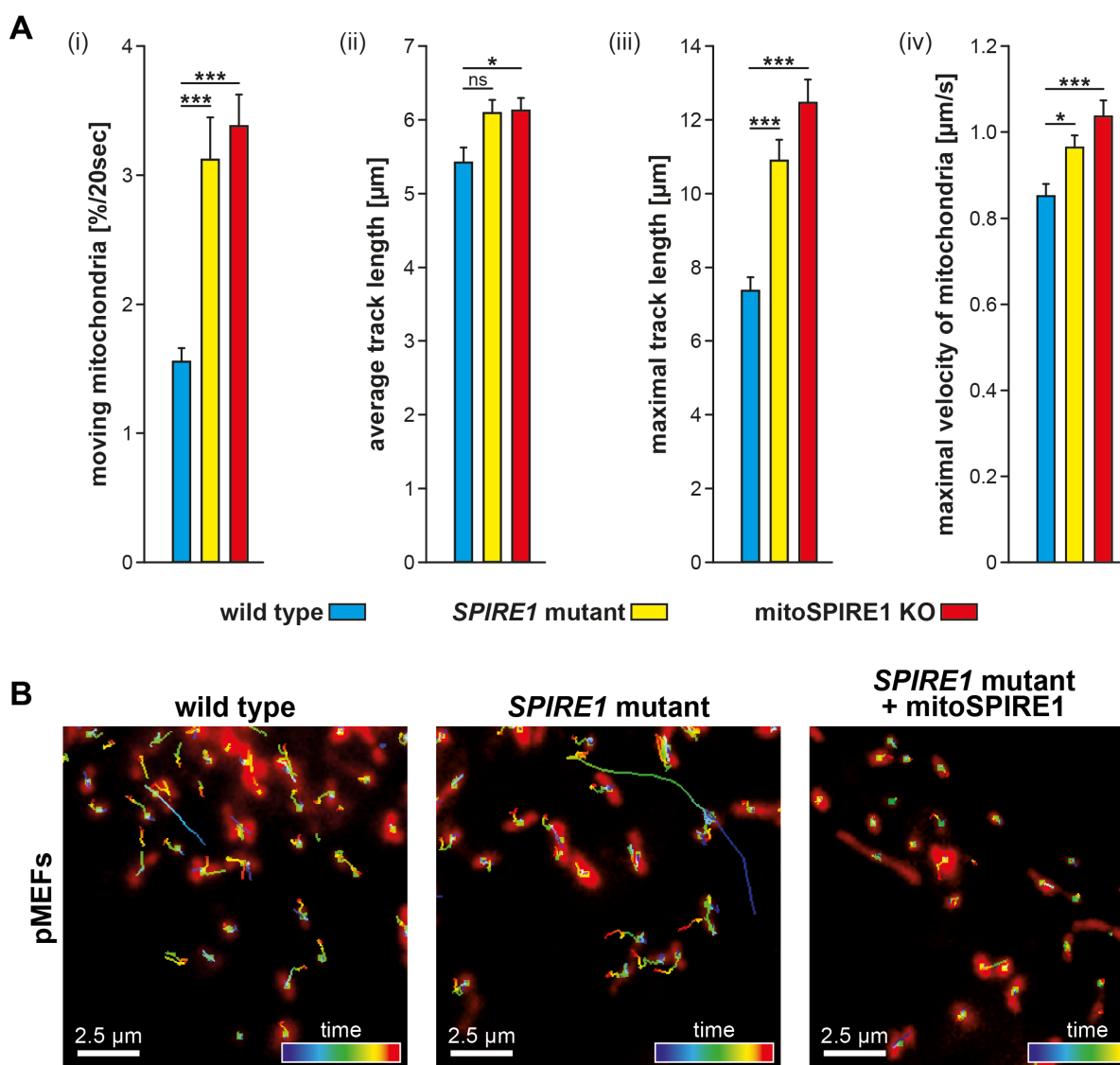


Figure 22 - mitoSPIRE1 influences mitochondria motility. Motility of mitochondria was measured in a time range of 20 seconds in wild type, *SPIRE1* mutant and mitoSPIRE1 KO primary mouse embryonic fibroblasts (pMEFs), respective migratory tracks were detected and analyzed via a custom tracking-mask by IMARIS software. Motility of mitochondria was grouped according to the measured track length into three different classifications: *fixed*, *wiggle* and *moving* mitochondria. Only *moving* mitochondria were used for further motility analysis. (A) The absence of mitoSPIRE1 increases the motility of mitochondria in pMEFs. (i) pMEFs without the mitoSPIRE1 protein showed a significantly increased number of moving mitochondria. (ii) The average mitochondria track length and (iii) the maximal track length of moving mitochondria in pMEFs of *SPIRE1* mutant and mitoSPIRE1 KO mice was increased compared to wild type. (iv) Furthermore, in absence of mitoSPIRE1, the maximal transport

velocity of moving mitochondria was significantly increased. Each bar represents respective mean values, *error bars* represent SEM. The numbers of cells and embryos used are shown in Table 4. One-way ANOVA has been performed; for each parameter a significant difference between species was detected; proofed effect size [(i): $\eta^2 = 0.249$; (ii): $\eta^2 = 0.054$; (iii): $\eta^2 = 0.279$; (iv): $\eta^2 = 0.112$]; Tukey-Kramer test has been performed as post-hoc analysis: ns = not significant, * = $p < 0.05$, *** = $p < 0.001$. None of the investigated parameters showed a significant difference between *SPIRE1* mutant and mitoSPIRE1 knockout pMEFs. **(B)** Representative cells with MitoTracker Orange stained mitochondria including individual mitochondrial motility tracks for wild type (left panel), *SPIRE1* mutant (middle panel) and *SPIRE1* mutant pMEFs overexpressing mitoSPIRE1 protein (right panel) are shown. Track color code represents timepoints of mitochondrial movement. Mitochondria of *SPIRE1* mutant cells show a higher maximal track length compared to wild type mitochondria. Overexpression of mitoSPIRE1 leads to a significant reduction in mitochondrial motility.

3.8.4 Overexpression of mitoSPIRE1 influences mitochondrial motility

The previous experiments revealed that the absence of mitoSPIRE1 causes an increase in mitochondrial motility in pMEFs. Based on that, we repeated the experimental set up trying to rescue the motility phenotype by transient expression of AcGFP1 tagged mitoSPIRE1 proteins. Transient expression of AcGFP1 served as a control. In all tested cell lines, the mitochondrial motility was significantly reversed for all measured parameters by transient overexpression of mitoSPIRE1 (Figure 23). In more detail, the expression of mitoSPIRE1 in *SPIRE1* mutant and mitoSPIRE1 knockout pMEFs reduced the number of moving mitochondria significantly to 0.53 - 0.93 % compared to the native state control (3.12 - 3.38 % of moving mitochondria; Figure 23, A and 22, B). The transient expression of mitoSPIRE1 in wild type pMEFs showed a significantly lower number of moving mitochondria (0.41 %) than the belonging native state control (1.56 %; Figure 23, A). Furthermore, the average track length in both mitoSPIRE1 deficient cell lines was reduced significantly to 3.1 - 3.41 μm in comparison with the native state control (6.09 - 6.12 μm ; Figure 23, B). In addition, the average track length of wild type mitochondria was significantly reduced to 2.23 μm after transient overexpression of mitoSPIRE1 compared to the native state control (5.42 μm ; Figure 23, B). The maximal track length is reduced by transient expression of mitoSPIRE1 in all three cell lines significantly (transient overexpression of mitoSPIRE1: wild type: 2.32 μm ; *SPIRE1* mutant: 3.18 μm ; mitoSPIRE1 knockout: 3.77 μm ; Figure 23, C) compared to the belonging native state (untransfected native state: wild type: 7.36 μm ; *SPIRE1* mutant: 10.89 μm ; mitoSPIRE1 knockout: 12.46 μm ; Figure 23, C). In line with that, the maximum velocity of mitochondria from all cell lines was reduced to 0.61 - 0.71 $\mu\text{m/s}$ compared to native state control groups (0.85 - 1.04 $\mu\text{m/s}$; Figure 23, D). The transient expression of AcGFP1 did not significantly

affect the motility of mitochondria in any cell line. In summary, the transient overexpression of mitoSPIRE1 reverses all measured parameters significantly, independent from the genotype and therefore impairs mitochondrial motility.

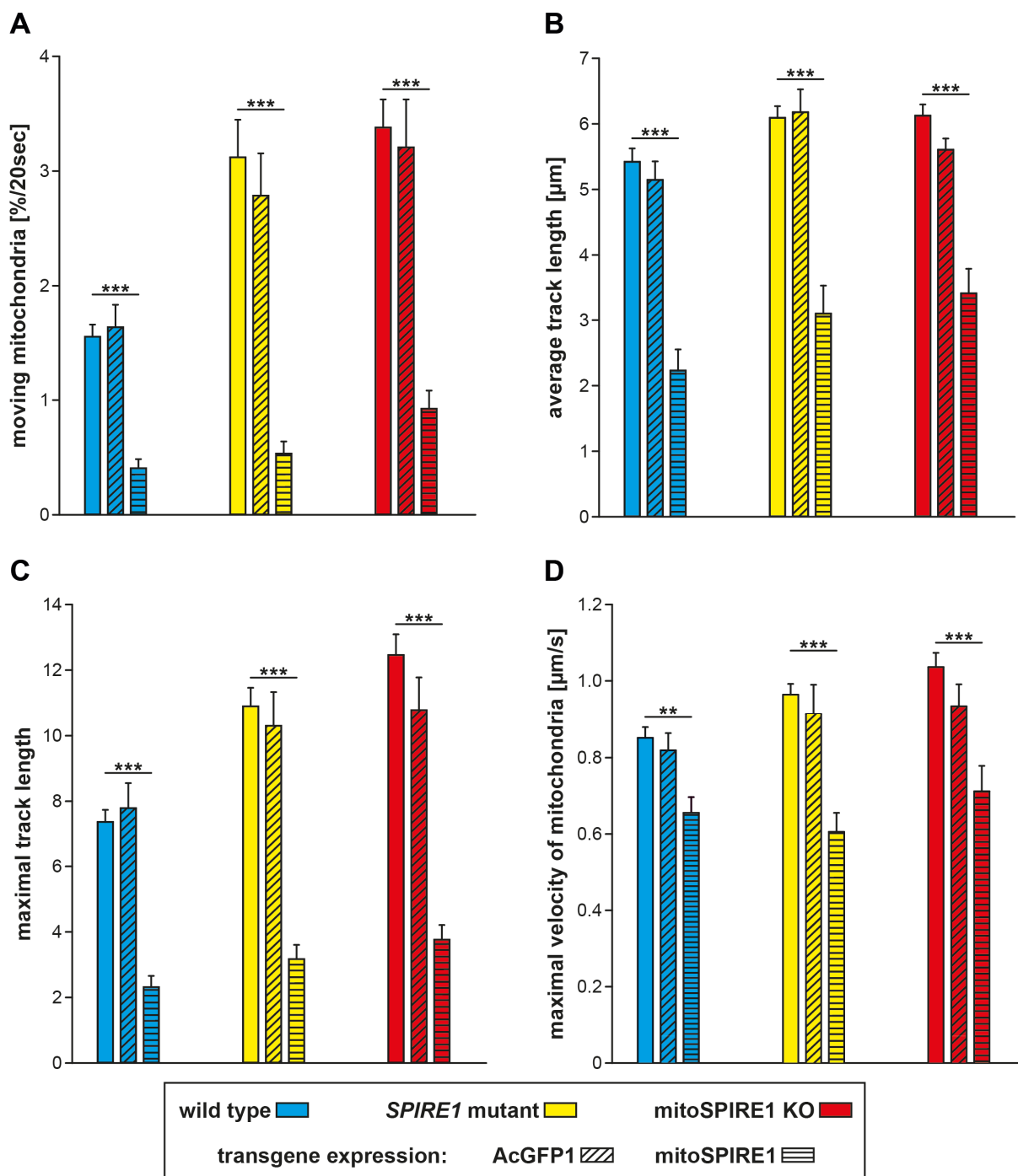


Figure 23 - Overexpression of mitoSPIRE1 influences mitochondria motility in pMEFs. Motility of mitochondria was measured in a time range of 20 seconds in wild type, *SPIRE1* mutant and mitoSPIRE1 KO primary mouse embryonic fibroblasts (pMEFs) following respective transfections, mitochondria tracks were detected and analyzed by IMARIS software with a custom tracking-mask. Motility of mitochondria was grouped according to the measured track length into three different classifications: *fixed*, *wiggle* and *moving* mitochondria. Only

moving mitochondria were used for further motility analysis. **(A)** The number, **(B)** the average track length, **(C)** the maximal track length and **(D)** the maximal velocity of *moving* mitochondria are shown in bar diagrams for pMEFs isolated from wild type (*blue*), *SPIRE1* mutant (*yellow*) and mitoSPIRE1 KO (*red*) mice. For each cell type analysis data are presented for the native state (untransfected control) and following overexpression of AcGFP1 or full-length mitoSPIRE1 proteins, respectively (refer to transgene expression). The transient overexpression of mitoSPIRE1 reverses all measured parameters significantly, independent from the genotype and therefore impairs mitochondrial motility. Between native states and following transient overexpression of AcGFP1 for none cell type a significant difference was detected. Each bar represents mean values, *error bars* represent SEM. The number of cells and embryos used are shown in Table 4. Two-way ANOVA with 1 factor species 3 levels and 1 factor expression 3 levels has been performed; in all cases of expression a significant difference was detected; proofed effect size ($\eta^2_p > 0.9$); Tukey-Kramer test has been performed as post-hoc analysis: ** = $p < 0.01$, *** = $p < 0.001$. For all cell types, only differences in the native state (untransfected controls) and following overexpression of full-length mitoSPIRE1 proteins are shown in bar diagrams.

Expression	wild type		<i>SPIRE1</i> mutant		mitoSPIRE1 knockout	
Non-transfected control (native state)	72	6	39	3	49	4
AcGFP1	29	5	12	2	15	3
mitoSPIRE1	47	6	26	3	26	4

number of cells
 number of embryos

Table 4 - Number of cells (*ocher*) and embryos (*blue*) used in experiments of Figure 22 / 23.

4. Discussion

Mitochondria contribute to a multitude of intracellular processes, where they, for example, function as Ca^{2+} storage for neurotransmission (Medler and Gleason, 2002) or produce precursors for macromolecules (Spinelli and Haigis, 2018), but their major task is to provide energy in the form of ATP. The intracellular energy supply requires a sophisticated spatial and temporal regulation, which is facilitated by different aspects of mitochondrial dynamics in order to adjust to diverse intracellular situations. Thus misregulated mitochondrial dynamics including fission, fusion and motility are associated with severe neurodegenerative diseases like the peripheral neuropathy Charcot-Marie-Tooth type 2A (Chen and Chan, 2009).

Mitochondrial motility is mediated by a complex intracellular transport system (Hollenbeck and Saxton, 2005), in which mitochondria are specifically transported to distinct cellular compartments. Until recently, mainly the microtubule transport of mitochondria via kinesin and dynein motor proteins was analyzed (Hollenbeck and Saxton, 2005; Chen and Chan, 2009; Sheng, 2014), but in the last years accumulating evidence was generated for a potential role of actin filaments in mitochondria motility as well (Pathak et al., 2010; Gutnick et al., 2019; Rangaraju et al., 2019). The mitochondrial transport machinery is highly complex, and it is still unknown how actin filaments affect mitochondrial motility, and how this process is regulated at the molecular level. The present thesis identified the actin nucleation factor mitoSPIRE1 as an adapter between mitochondrial membranes and FMN subfamily formins as well as myosin 5 (MYO5) actin motor proteins. Consistently, the present thesis shows that mitoSPIRE1 influences mitochondrial movement. These findings open the possibility that mitoSPIRE1 cooperates with FMN subfamily formins to build a functional actin nucleator complex and to generate a local actin meshwork at mitochondrial surfaces, which can subsequently be used by MYO5 motors to anchor mitochondria at certain intracellular positions (Figure 24).

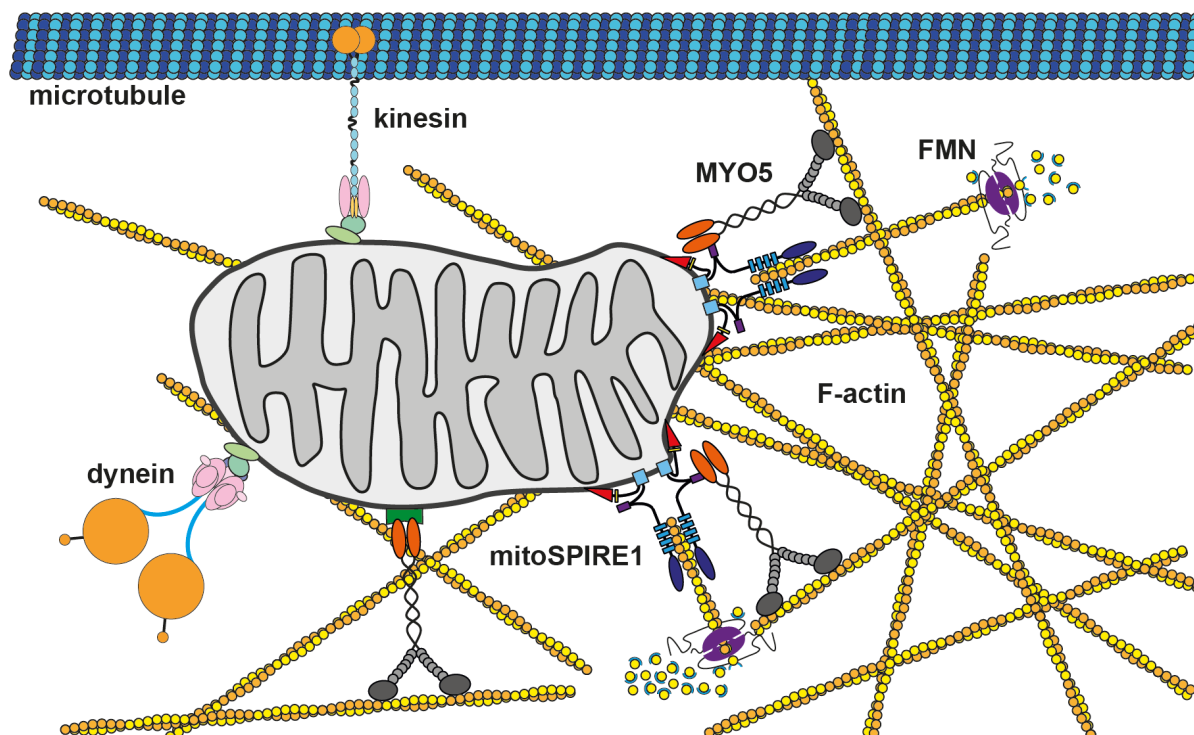


Figure 24 - Model for mitoSPIRE1 function in mitochondria transport. Mitochondria are transported along microtubules over long distances via kinesin and dynein motor proteins. In contrast, myosin 5 (MYO5) actin motor proteins might drive short-range local mitochondria transport along actin networks. In addition, MYO5 could influence the processivity of microtubule-based long-range transport of mitochondria. In the here presented model, exon 13 drives localization of mitoSPIRE1 to the outer mitochondrial membrane which facilitates translocation of MYO5 and FMN subfamily formin proteins towards mitochondria. Moreover, based on the known SPIRE-KIND / FMN-FSI interaction a mitochondrion associated mitoSPIRE1 / FMN protein complex might be able to generate actin filaments directly at the mitochondrial surface. In summary, a protein complex, including mitoSPIRE1, FMN subfamily members and MYO5 actin motors, could generate a local mitochondrial actin network, which could ultimately be used by MYO5 to anchor mitochondria at actin filaments. The here described mitochondrial anchor system driven by mitoSPIRE1, FMN subfamily formins and MYO5 proteins could therefore influence mitochondria motility.

4.1 Expression of *SPIRE* splice variants in mouse tissues

Nearly two decades ago studies revealed that the mammalian genome encodes for two *SPIRE* genes (Schumacher et al., 2004). To understand the role of SPIRE proteins in distinct tissues and organs, several experiments specified the expression of these two genes in the following years. In this context, *in situ* hybridizations showed that the *SPIRE1* gene is mainly expressed in the developing central nervous system and in specific brain regions in adult mice (Schumacher et al., 2004; Pleiser et al., 2010). In addition, Northern blot analyzes also revealed high *SPIRE1* expression in the adult mouse brain and these experiments detected a weak expression of *SPIRE1* in spleen and kidney (Schumacher et al., 2004; Pleiser et al., 2010). Using

the same method *SPIRE2* was mainly detected in tissues of the digestive tract, the brain and in testis (Pleiser et al., 2010). Subsequently, the expression of *SPIRE1* and *SPIRE2* genes was analyzed in more detail by means of quantitative real time PCR (qPCR) which possesses much higher sensitivity. *SPIRE1* was most highly expressed in oocytes, brain and in testis, whereas *SPIRE2* was highly expressed in the same tissues as *SPIRE1* but showed additionally a high expression in the digestive tract (Pfender et al., 2011; Pleiser, 2012).

More recently, two additional *SPIRE1* isoforms were described; which result from alternative splicing. The mammalian *SPIRE1* gene carries two alternatively spliced exons, and therefore encodes, in summary, for three different *SPIRE1* proteins, namely SPIRE1, SPIRE1-E9 and mitoSPIRE1. The SPIRE1-E9 protein contains 14 unique amino acids encoded by exon 9, whereas the mitoSPIRE1 protein contains a sequence of 58 amino acids encoded by the alternatively spliced exon 13. To get an overview of the expression of all known *SPIRE1* splice variants, a quantitative real time PCR of mouse tissues was performed in the present thesis in order to obtain absolute mRNA copy numbers. The use of specific primer pairs for each *SPIRE* splice variant revealed a distinct expression pattern for *SPIRE* mRNAs. Absolute quantification by qPCR of *SPIRE1* and *SPIRE1-E9* was already done in my master thesis and the respective results are presented in the same graph (Figure 11).

All tested organs show expression of at least two *SPIRE1* splice variants and *SPIRE2*. The highest expression of *SPIRE1* was detected in the brain, whereas a high expression of *SPIRE2* was found in testicle as well as in the small and large intestine. Those results are in line with previous data from Northern blot analysis (Schumacher et al., 2004; Pleiser et al., 2010). However, qPCR analysis in the present thesis showed *SPIRE* expression in tissues, which was not detected by Northern blot analysis previously (Schumacher et al., 2004; Pleiser et al., 2010). This is likely due to a sensitivity difference of the methods. Anyhow, absolute quantification by qPCR shows results with a similar tendency as analysis of *SPIRE1* and *SPIRE2* expression with relative quantification by qPCR (Pfender et al., 2011; Pleiser, 2012).

Relative quantification of *SPIRE1* and *SPIRE2* revealed already in 2011 that *SPIRE* genes are only expressed at low levels (Pfender et al., 2011; Pleiser, 2012). The measured expression of *SPIRE1-E9* and *mitoSPIRE1* in the present thesis was even lower than the expression of the already minimally expressed *SPIRE1* and *SPIRE2* mRNAs. Given the low mRNA expression levels, we should be critical about the importance of SPIRE1-E9 and mitoSPIRE1 proteins at endogenous levels in intracellular processes. Nevertheless, based on the expression data,

mitoSPIRE1 might have a role in kidney, testicle and in the brain, whereas SPIRE1-E9 could have a role in the brain. However, these experiments show that *SPIRE* splice variants are generally expressed at low mRNA levels, but do not allow conclusions about protein concentrations. For this reason, the mRNA expression data do not describe the number of SPIRE proteins in the cell, which could be higher or lower than the indicated mRNA level by the belonging *SPIRE* splice variant due to different protein translation and stability. The presented expression pattern shows that *SPIRE2* is preferentially expressed in the testicle and the large and small intestine, while *SPIRE1* splice variants are mainly expressed in the brain, pointing that the splice variants have distinct importance in tissues. The mitochondrial *mitoSPIRE1* is mainly expressed in the kidney, which could be explained by the high energy consumption of the organ in filtration processes.

4.2 Similar expression patterns of *SPIRE1* and *mitoSPIRE1* in the mouse brain

SPIRE1 mutant mice lack the expression of any functional *SPIRE1* protein and show an increased fear-related behavior in contextual and cued fear conditioning experiments compared to wild type mice (Pleiser et al. 2014). One explanation for the altered fear behavior might be the loss of mitoSPIRE1 proteins particularly in the brain, in which we found *mitoSPIRE1* expression (Figure 11). In this respect, especially the absence of mitoSPIRE1 in brain areas involved in fear learning could influence the mouse behavior. The expression of the *SPIRE1* gene was already detected by *in situ* hybridizations in the hippocampus, dentate gyrus and in the cerebellum of mice (Schumacher et al., 2004; Pleiser et al., 2010). The *in situ* data of the present thesis confirm the expression of the *SPIRE1* gene in the hippocampal formation. Furthermore, a strong positive signal for *mitoSPIRE1* could be detected in the hippocampal formation as well (Figure 12). The expression of mitoSPIRE1 in the hippocampal formation seems to be important, because the hippocampus may be involved in contextual fear learning (Gewirtz et al., 2000). In addition, a low level of *mitoSPIRE1* expression was detected in the cortex, hypothalamus and the amygdala (data not shown). Interestingly, amygdala lesions in both humans and rodents influencing the recognition of fearful stimuli (Janak and Tye, 2015). The absence of mitoSPIRE1 in the hippocampus and the amygdala could induce an organ dysfunction and influence fear related behavior. However, as the brain is a very complex organ with a multitude of interconnected regions, it might well be that neuronal dysfunctions in cells of any brain area could finally influence animal behavior. In summary, the *in situ* hybridization

data shown here are very preliminary, because of limited brain slice numbers and therefore those experiments need to be repeated.

4.3 Subcellular localization of SPIRE proteins

SPIRE proteins contain highly conserved domains each serving specific functions. The FYVE-type zinc-finger interacts with negatively charged membranes and targets the protein towards intracellular membrane structures (Kerckhoff et al., 2001; Tittel et al., 2015). As a consequence, the subcellular localization targets SPIRE function directly to distinct organelles.

SPIRE proteins facilitate the generation of actin filaments, and are able to recruit both MYO5 actin motors and FMN subfamily formins (Pechlivanis et al., 2009; Pylypenko, Welz et al., 2016; Alzahofi, Robinson, Welz et al., 2018). The resulting protein complex of SPIRE / MYO5 / FMN was shown to mediate the motility of RAB11 vesicles in oocytes and melanosome transport in melanocytes (Schuh, 2011; Alzahofi, Robinson, Welz et al., 2018). The subcellular localization of SPIRE proteins is therefore important for vesicles and organelles, which can be directly influenced by SPIRE and its associated MYO5 / FMN functions. Our results show, in line with the literature, that SPIRE1 and SPIRE2 proteins localize at vesicles and do not show any other subcellular localization (Figure 13; Kerckhoff et al., 2001; Schuh et al., 2011; Dietrich et al., 2013; Tittel et al., 2015). We also confirmed that the mitoSPIRE1 protein does not colocalize with vesicular SPIRE proteins, but instead is localized to mitochondria. The mitochondrial localization of mitoSPIRE1 is mediated by the alternatively spliced exon 13 (Manor et al., 2015). In contrast to exon 13, the 14 amino acid spanning sequence encoded by the alternatively spliced exon 9 does not change the vesicular localization of SPIRE1-E9, as SPIRE1-E9 colocalizes with SPIRE1 proteins (Figure 13). Potentially, the exon 9 encoded sequence is able to interact with yet unknown proteins, but the identification of those proteins requires further investigations. In our experiments, the overexpression of proteins can also cause accumulation effects, which is why it cannot be excluded that SPIRE1-E9 proteins also may have a specific vesicular membrane localization. However, in transient overexpression studies SPIRE1, SPIRE1-E9 and SPIRE2 proteins show a vesicular and mitoSPIRE1 a mitochondrial localization. Thus, SPIRE function is available at vesicular and mitochondrial membranes, and could in general influence the motility of these organelles.

4.4 Interaction of mitoSPIRE1 with the outer mitochondrial membrane

Vesicular SPIRE proteins use the FYVE-type zinc-finger at their C-terminal end to anchor at vesicle membranes. As a consequence, the whole protein except some amino acids of the hydrophobic turret loop from the FYVE-type zinc-finger is located in the cytosol and conserved domains are free to interact with cooperation partners (Kerckhoff, 2011; Tittel et al., 2015). In contrast, the C-terminal end of mitoSPIRE1 was described to be localized in the mitochondrial intermembrane space (IMS). It was reported that the alternatively spliced exon 13 encoded sequences are predicted to integrate directly into the outer mitochondrial membrane to localize the protein to mitochondria, whereas all C-terminal sequences following the exon 13 are localized inside the mitochondrial IMS and do not face the cytosol (Manor et al., 2015). In this predicted localization of mitoSPIRE1, the SPIRE-box and the FYVE-type zinc-finger are located in the IMS of mitochondria and could probably not interact with potential cooperation partners.

However, the experiments performed here, through cell stainings using specific antibodies and cell permeabilization protocols (Figure 14, 15), indicate that the C-terminal end of mitoSPIRE1 is located inside the cytosol and not in the IMS. In this work, the secondary amino acid structure of the alternatively spliced exon 13 encoded sequences was predicted by the PHYRE software (<http://www.sbg.bio.ic.ac.uk/phyre2/html/page.cgi?id=index>) as it was already described by Uri Manor in 2015 (Figure 15, A; Manor et al., 2015). The prediction reveals two α -helices separated by a loop sequence which could form a hairpin structure in the mitochondrial membrane and as a consequence, the C-terminal end might also face the cytosol. Both helices contain hydrophobic amino acids, which could facilitate helix integration in the hydrophobic lipid double layer of the polar membrane. Furthermore, both helices are long enough (15 - 20 residues) to span the mitochondrial outer membrane (Manor et al., 2015). In addition, fluorescence microscopy data of this thesis show evidence that the mitoSPIRE1 C-terminus is located in the cytosol (Figure 15). In this experiment, an antibody staining against an IMS located part of cytochrome C was used as negative control to make sure that the mitochondrial outer membrane is still intact and not permeabilized by the mild permeabilizer Digitonin. Both, Triton X-100- and Digitonin-permeabilized cells show a high colocalization of GFP tagged mitoSPIRE1 proteins to the C-terminal SPIRE1 antibody staining (anti-SPIRE1, SA-2133). In contrast, cells permeabilized by Digitonin show a significantly reduced colocalization of antibody stained cytochrome C to mitochondria-localized GFP-mitoSPIRE1 compared to the same colocalization in Triton X-100-permeabilized cells. This indicates that in the Digitonin

permeabilized cells the antibody is impaired to bind to mitochondria localized cytochrome C. The differences in antibody staining of cytochrome C between Digitonin and Triton X-100 treated cells on one hand, and the identical antibody staining of the mitoSPIRE1 protein by SA-2133 on the other hand, indicate that the C-terminal end of mitoSPIRE1 rather faces the cytosol. Our experiments accumulate evidence that the C-terminal end of mitoSPIRE1 is located in the cytosol, which, however, awaits further confirmation in future experiments.

The cytosolic C-terminal localization could explain how mitoSPIRE1 is anchored in mitochondrial membranes. In this theory, the exon 13 encoded sequences could determine the specific localization at the outer mitochondrial membrane and the FYVE-type zinc-finger could stabilize anchoring of the whole protein at the selected membrane by interaction with negatively charged lipids of the outer mitochondrial membrane. Furthermore, the C-terminal end including the SPIRE-box could interact with mitochondria specific RAB GTPases. Anyhow, there is a chance that a mitoSPIRE1 splice variant is expressed, which is truncated and does not contain the C-terminal end. In this case exon 13 could work as a single membrane anchor.

4.5 mitoSPIRE1 targets FMN subfamily formin proteins towards mitochondria

The present colocalization study of fluorescently tagged mitoSPIRE1 and formin proteins shows that transiently expressed mitoSPIRE1 proteins can specifically translocate FMN subfamily formins but not INF2 proteins towards mitochondrial membranes. In addition, the experiments reveal that FMN subfamily formins need the C-terminal FSI motif to colocalize with mitoSPIRE1 (Figure 16).

SPIRE proteins fail to process profilin-actin monomers, which are used for actin polymerization in cells (Montaville et al., 2014). In a well described model, FMN subfamily formins cooperate with SPIRE proteins to provide free actin monomers, which can be used subsequently by SPIRE WH2 domains to initiate actin filament polymerization (Figure 3). Anyhow, the cooperation between FMN and SPIRE proteins illustrates an efficient machinery to create actin filaments (Pechlivanis et al., 2009; Pfender et al., 2011; Schuh et al., 2011; Alzahofi, Robinson, Welz et al., 2018). The present colocalization study indicates that mitoSPIRE1 might be able to translocate FMN1 and FMN2 towards mitochondria at endogenous levels. A protein complex formation of mitoSPIRE1 and FMN subfamily formins at mitochondria could induce actin filament generation directly at mitochondria surfaces and these newly generated actin filaments could influence mitochondrial dynamics. In this context, it is already reported in the literature

that actin filaments influence mitochondrial fission events (Manor et al., 2015), and mitochondria motility (Gutnick et al., 2019; Rangaraju et al., 2019).

INF2 enriches the amount of actin filaments at mitochondria (Korobova et al., 2013), and was described to interact directly with mitoSPIRE1 (Manor et al., 2015). In this context, INF2 facilitates the translocation of the floppy ER towards mitochondria to finally induce a constriction at mitochondrial fission sites (Manor et al., 2015). The endoplasmic reticulum associated isoform of INF2 - INF2-CAAX, and its cytoplasmic correlate INF2-NonCAAX both do not significantly colocalize with mitoSPIRE1 in our transient expression studies, compared to FMN1 and FMN2 (Figure 16). This indicates that both INF2-CAAX and INF2-NonCAAX do not interact strongly with mitoSPIRE1 at an endogenous level. The reported binding strength for the INF2-CAAX / SPIRE1 KIND interaction is very low (K_d : 25 - 30 μ M; Manor et al., 2015), which in addition to the here presented colocalization study indicates that it is rather unlikely that these two proteins interact at an endogenous protein level. If both proteins would interact strongly, a colocalization would be expected in over-expression studies as it is shown for FMN subtype formins (Figure 16). However, it cannot be excluded despite the weak interaction that INF2 and mitoSPIRE1 both contribute to the formation of a larger multimeric protein complex at mitochondrial surfaces, which finally serves to induce constriction of mitochondrial fission sites.

4.6 mitoSPIRE1 targets MYO5 actin motor proteins towards mitochondria

Myosin proteins are actin-based motor proteins that are involved in many functional processes, such as muscle contraction, cytokinesis, signal transduction and intracellular transport processes of organelles and other components (Hartman and Spudich, 2012). Especially the unconventional class 5 and class 6 myosins are associated with transport mechanisms of distinct organelles (Sellers, 2000; Kneussel and Wagner, 2013). In this regard, class 5 myosins mediate transport towards the actin filament barbed end (plus-end) whereas class 6 myosins move towards the minus end of polarized actin filaments (Wells et al., 1999; Sakamoto et al., 2000).

Our colocalization studies show that C-terminal MYO5A and MYO5B proteins colocalize with full-length mitoSPIRE1 at mitochondria but not with the isolated exon 13 of mitoSPIRE1 (Figure 18, A). In general, the interaction of myosins to their cargo is facilitated by adapter proteins (Yu et al., 2009) or the myosin protein interacts directly with the cytoplasmic portion of transmembrane molecules from its cargo (Fagarasanu et al., 2009). Like all SPIRE proteins,

the used GFP tagged full-length mitoSPIRE1 protein contains the globular tail domain binding motif (GTBM), which allows a direct interaction to the globular tail domain (GTD) of MYO5 motor proteins. The difference of the colocalization between isolated exon 13 encoded sequences and full-length mitoSPIRE1 to the truncated MYO5A or MYO5B protein is therefore most likely caused by the GTBM of SPIRE proteins. The here presented colocalization study shows that, at least under transient over-expression conditions, the mitochondria-localized mitoSPIRE1 is able to translocate MYO5 proteins from vesicles to mitochondria.

A mitochondrial mitoSPIRE1 / MYO5 protein complex is further supported by the fact that fibroblasts having a mutated *SPIRE1* gene and therefore lack all functional *SPIRE1* proteins show a lower number of MYO5A-positive mitochondria compared to wild type fibroblasts in fluorescence-activated mitochondria sorting (FAMS) analysis (Figure 18, B). Furthermore, the FAMS results indicate that MYO5 proteins are also recruited to mitochondrial surfaces by mechanisms different from SPIRE, given the fact that even in *SPIRE1* mutant cells there is still a considerable amount of MYO5A proteins present at mitochondrial membranes. Nevertheless, reduced MYO5A-positive mitochondria of *SPIRE1* mutant fibroblasts can also be caused by the loss of SPIRE1 or SPIRE1-E9, because SPIRE1 and SPIRE1-E9 could be involved in the transport of MYO5A proteins towards mitochondria.

However, the mitoSPIRE1 mediated recruitment of MYO5 to mitochondria could be an important mechanism for the mitochondrial transport machinery. In this context, MYO5 could use mitoSPIRE1 generated actin filaments to drive mitochondrial movement, as it is already described for RAB11 vesicles in oocytes or melanosome transport (Schuh et al., 2011; Pylypenko, Welz, et al. 2016; Alzahofi, Robinson, Welz et al., 2018). In addition, the mitoSPIRE1 generated actin filaments could be used by MYO5 to anchor mitochondria at a certain position in the cell.

4.7 Generation of a mitoSPIRE1 knockout mouse model

Genetically modified mice have become a useful tool for scientists to study the biological role of specific genes, because single genes can be targeted and modified at the genomic level. In this context, knockout models describe mice which are genetically modified by a certain inactivation of an individual gene. The targeting of a specific gene often results in a distinct phenotype, which provides conclusive evidence for the functional role of the gene product (Hall et al., 2009). However, it also happens frequently that the interference with a specific gene does

not induce significant phenotypes or any phenotype at all. By employing CRISPR / Cas9 editing technology the genomic modification of embryonal stem cells (ES cells) works with a high rate of success (Yang et al., 2014). By injection of the modified totipotent ES cells into a mouse blastocyst, the genetically modified ES cells differentiate into all cell subtypes in a chimeric mouse. Final crossbreeding of chimeric mice, which carry the gene modification in their germline, results in mice containing the desired targeted gene modification (Hall et al., 2009).

In the present thesis, a knockout mouse was generated using the CRISPR / Cas9 gene editing technology in ES cells in order to inactivate the alternatively spliced *exon 13* of the *SPIRE1* gene (Figure 19). The inactivation of *exon 13* is expected to result in a mouse model which is able to express SPIRE1 and SPIRE1-E9 but not the mitoSPIRE1 protein. The successful inactivation of *exon 13* was confirmed by DNA analysis checking the absence of *SPIRE1 exon 13* in mitoSPIRE1 knockout mice. In addition, the genetically modified mice did not express mRNAs containing the alternatively spliced *exon 13* of the *SPIRE1* gene (Figure 19). The endogenous protein levels of mitoSPIRE1 are extremely low, and given that a specific mitoSPIRE1 antibody is not available today, it is impossible to confirm the absence of mitoSPIRE1 proteins by immunoblot. However, considering that both the genomic DNA and mRNA *exon 13* sequences are missing in the mitoSPIRE1 knockout mouse we assume that the mice cannot express any mitoSPIRE1 protein. Nevertheless, by means of GST-pulldown assays using GST tagged FMN2-eFSI peptides, we confirmed that mitoSPIRE1 knockout mice still express SPIRE1 (and presumably SPIRE1-E9) proteins. These experiments verify that we have generated a knockout mouse that is specifically lacking the expression of mitoSPIRE1 proteins. The novel mitoSPIRE1 knockout mouse carries the gene modification in every single cell and can therefore be used to analyze the role of mitochondrial mitoSPIRE1 at the subcellular, cellular and organismic level.

Mice which lack the expression of any functional *SPIRE1* splice variant are more fearful in contextual and cued fear conditioning experiments (Pleiser et al., 2014). Until now it is unclear whether the deficiency of a single splice variant of the *SPIRE1* gene is sufficient to cause this phenotype or if the combined absence of all three *SPIRE1* encoded proteins is necessary. In this respect, it would be indispensable to test whether the mitoSPIRE1 knockout mice have a fear related phenotype, which would support a role for mitoSPIRE1 in fear related behavior.

The newly generated mitoSPIRE1 knockout mouse is furthermore a valuable tool to get a deeper insight into the cellular role of the mitoSPIRE1 protein. In future experiments, any type

of cell can be isolated, cultured and analyzed for mitoSPIRE1 dependent alterations. In this context, neuronal cells could be analyzed for neurotransmitter release of oxytocin, which influences fear behavior (Knobloch et al., 2012). In addition, the mitoSPIRE1 knockout mouse could be investigated for abnormalities in mouse behavior experiments.

4.8.1 Influence of SPIRE absence on mitochondrial morphology

The morphology of mitochondria is a result of the precisely regulated balance between mitochondrial fission and fusion processes. As a consequence of these dynamic events, mitochondria have the ability to adjust their size to intracellular alterations, which allows mitochondria to fulfill their functions in an appropriate way for cellular requirements (Chen and Chan, 2009). The importance of dynamic mitochondrial fission and fusion events is highlighted by the fact that failure of these events not only influences the mitochondrial morphology, but also affects function and motility of mitochondria, and can therefore cause severe diseases or even death (Amiott et al., 2008; Ishihara et al., 2009; Chen and Chan, 2009; Lenaers et al., 2012).

By means of employing fluorescence microscopy, the length of mitochondria from fibroblasts isolated from *SPIRE1* mutant mice, which do not express any functional SPIRE protein from the *SPIRE1* gene, mitoSPIRE1 knockout mice and wild type mice was analyzed in this thesis (Figure 20, B). In addition, 3-dimensional measurements of the mitochondria size from fibroblasts were performed for the same genotypes by flow cytometry (fluorescence-activated mitochondria sorting; FAMS) experiments (Figure 20, A). During flow cytometry, the combination of forward scatter photomultiplier tube area (FSC PMT-A) and the more sensitive side scatter area (SSC-A) was used to determine the 3-dimensional mitochondrial size. In this context, SSC-A provides information about the internal complexity of a mitochondrion, while the FSC PMT-A describes the mitochondrial diameter. Both fluorescence microscopy and FAMS experiments show that fibroblasts from all tested genotypes contain large, intermediate and fragmented mitochondria. The quantification of mitochondrial length by 2-dimensional microscopy revealed that mitochondria from primary mouse embryonic fibroblasts (pMEFs) lacking mitoSPIRE1 or all *SPIRE1* proteins, respectively, show a reduced mitochondrial length compared to wild type mitochondria. Furthermore, 3-dimensional size measurements of mitochondria by FAMS show that fibroblasts lacking functional *SPIRE1* proteins or only mitoSPIRE1, respectively, have a higher number of small mitochondria and lower number of

large mitochondria compared to wild type fibroblasts. For the 3-dimensional size analysis, *SPIRE1* mutant mitochondria were analyzed in immortalized mouse embryonic fibroblasts (iMEFs), while mitoSPIRE1 knockout mitochondria were analyzed in pMEFs. In this aspect, the determined mitochondria size by FSC PMT-A of wild type mitochondria from iMEFs and pMEFs differ, which could be explained by the general differences between the two cell lines used. In summary, these results indicate that mitochondria of fibroblasts are smaller in the absence of the mitoSPIRE1 protein compared to wild type mitochondria, which is, however, not in line with the literature (Manor et al., 2015).

In 2015, it was published that mitoSPIRE1 is required for the process of mitochondrial fission. In this context, mitoSPIRE1 was alleged to interact with the ER-localized INF2 protein to mediate mitochondrial constriction at fission sites via actin assembly mechanisms. However, it was reported that a mitoSPIRE1 knockdown increases the length of mitochondria in U2OS cells (Manor et al., 2015). As we know from the present thesis mitoSPIRE1 expression is extremely low. A temporary reduction of mRNA levels by an RNA interference knockdown might be irrelevant for the physiological effect of mitoSPIRE1, because mitoSPIRE1 proteins could be stable and therefore they could be still present in cells affected by the knockdown. However, in the study of 2015, the length of mitochondria was only determined by 2-dimensional microscopy analysis and not more than mitochondria of 25 cells per group were measured. In addition to the low number of investigated mitochondria, microscopy length analysis of organelles can be easily biased for example by the operator, because mostly nice- and healthy-looking cells are recorded. After we found controversial mitochondrial lengths in our SPIRE knockout cell lines by microscopy analysis, we measured in FAMS the size of more than 15,000 mitoSPIRE1 knockout, 18,900 *SPIRE1* mutant and 7600 wild type mitochondria. In this connection, FAMS allows a 3-dimensional unbiased determination of mitochondrial size, because pooled fibroblasts of each cell line are lysed, and mitochondria are selected randomly for size measurements by a fluorescence-activated cell sorting (FACS) machine.

At least it seems that mitoSPIRE1 somehow influences the mitochondrial size. This might be caused by direct or indirect involvement of mitoSPIRE1 in mitochondrial fission or fusion events. A direct influence of mitoSPIRE1 could shift the balance towards either mitochondrial fission or fusion events and could therefore result in a morphological phenotype and severe dysfunction of mitochondria. An indirect influence on the complex processes underlying mitochondrial fission and fusion events might be caused by an alteration of mitochondria motility (Chen and Chan, 2009). In this context, the motility of mitochondria could be modified

by newly generated actin filaments mediated by mitoSPIRE1 in cooperation with FMN subfamily formins at mitochondrial surfaces. However, the morphological phenotype observed at absence of mitoSPIRE1 was not detected in all cells, which indicates that mitoSPIRE1 does not have a severe influence on fission and fusion events. In contrast, a homozygous knockout of the mitochondrial fission-associated protein dynamin-related protein 1 (Drp1) in mice is already lethal at an embryonic stage (Manczak et al., 2012) and embryonic Drp1^{-/-} fibroblasts contain extensive mitochondrial networks, which highlights the importance of Drp1 for mitochondrial fission events (Wakabayashi et al., 2009). To investigate the effects of mitoSPIRE1 on mitochondrial morphology in more detail, further experiments must be done. The frequency of fission and fusion events would be important to quantify in mitoSPIRE1 knockout cells compared to wild type cells in order to consider a potential direct effect from mitoSPIRE1 on mitochondrial morphology.

4.8.2 Influence of *SPIRE1* absence on mitochondrial respiration

Mammalian cells generate energy under physiological conditions mainly by mitochondrial respiration (oxidative phosphorylation; OXPHOS) and only to a small extent by anaerobic glycolysis. The highly efficient mitochondrial respiration processes molecules like NADH or succinate to convert energy into ATP, while using oxygen molecules as a terminal electron acceptor. In summary, during mitochondrial respiration oxygen molecules are consumed and ATP molecules are produced (Bonora et al., 2012; Smolina et al., 2017; Castellanos and Lanning, 2019). However, the highly motile mitochondria are transported to all cell areas in order to provide the whole cell with an adequate amount of energy in the form of ATP (Hollenbeck and Saxton, 2005). The interference with ATP supply is associated to severe diseases like diabetes or heart failure (Mogensen et al., 2007; Ingwall, 2009). Furthermore, the inadequate supply of energy, especially in neuronal cells, can alter the local protein synthesis during synaptic plasticity (Rangaraju et al., 2019) and therefore potentially the behavior of the whole organism. In this regard, limited ATP supply to specific cell areas can be caused by dysfunctions in the mitochondria transport system (Guo et al., 2005), but also by an impaired mitochondria respiration capacity (Smolina et al., 2017). In summary mitochondrial respiration is an irreplaceable process which enables the cell to drive energy consuming processes to finally ensure survival and functioning of mammalian cells.

In the present thesis, we measured the oxygen consumption rate (OCR) from isolated mitochondria of *SPIRE1* mutant and wild type fibroblasts *in vitro* to evaluate mitochondrial functionality (Figure 21, B). In this context, the OCR indicates how much oxygen is required by mitochondria to convert ADP into ATP. The treatment of fibroblasts with different biologically active modulators triggers functional mitochondrial reactions and provides a specific readout of mitochondrial parameters like the OCR for maximal or basal respiration. The results show that mitochondria in cells without having functional *SPIRE1* proteins do not significantly differ in the OCR in induced stress situations compared to mitochondria of wild type cells. For the maximal respiration rate, the OCR tends to be slightly reduced in mitochondria from *SPIRE1* mutant cells, but which is probably not relevant in a physiological environment. These results strongly indicate that proteins encoded by the *SPIRE1* gene do not severely influence mitochondrial respiration, and mitochondria of *SPIRE1* mutant mice are therefore functional and not restricted in OXPHOS. These results are confirmed by a bright mitochondrial TMRM staining of *SPIRE1* mutant fibroblasts (Figure 21, A), because the TMRM dye only accumulates in cells with functional mitochondria. Initially, we suggested that mitochondria of *SPIRE1* mutant cells show also a functional phenotype, as morphological changes of mitochondria often influence mitochondrial function as well (Chen and Chan, 2009). In the present thesis, it was shown that the absence of the mitoSPIRE1 protein induces morphological alterations of mitochondria, which was also reported before (Manor et al., 2015). However, the described morphological changes do not measurably alter mitochondrial respiration.

4.8.3 Function of mitoSPIRE1 in mitochondrial motility

Mitochondrial motility is an important aspect of mitochondrial dynamics. The essential mitochondrial transport system allows the supply of an adequate amount of energy in the form of ATP to all cell areas (Chen and Chan, 2009). The main transport of mitochondria is facilitated by kinesin and dynein motor proteins along rigid and polarized microtubules (Heidemann et al., 1981; Baas et al., 1988, 1989; Sheng, 2014). Our experiments revealed that fibroblasts without the mitochondrial actin nucleator mitoSPIRE1 contain a higher percentage of moving mitochondria compared to wild type fibroblasts. Furthermore, the mitochondria of mitoSPIRE1 deficient fibroblasts move faster and over longer distances than mitochondria from wild type fibroblasts (Figure 22). In our experiments, pMEFs lacking exclusively the mitoSPIRE1 protein present the same motility phenotype as pMEFs of *SPIRE1* mutant mice lacking the expression

of all functional proteins of the *SPIRE1* gene. This indicates that the motility effect is not caused by SPIRE1 or SPIRE1-E9 proteins but by mitoSPIRE1 as pMEFs from both genetically modified mice show an identical mitochondrial phenotype. In summary, we can conclude that mitochondria in pMEFs not expressing the mitoSPIRE1 protein are more motile than mitochondria in wild type cells.

As a proof of concept, the transient overexpression of mitoSPIRE1 reverses the mitochondrial motility phenotype dramatically in all pMEF cell lines investigated (Figure 23). Overexpression of mitoSPIRE1 significantly reduces the number of moving mitochondria and mitochondria are transported slower and over shorter distances than mitochondria from control cells. Significant differences in the experiment indicate that the actin nucleator mitoSPIRE1 might cooperate with MYO5 / FMN at mitochondria surfaces to influence mitochondrial motility.

These experiments clearly show that mitoSPIRE1 is involved in the molecular mechanisms to regulate the motility of mitochondria in pMEFs. As mentioned above, mitochondria are mainly transported along microtubules, but there is also accumulating evidence that actin filaments play an important role in the transport machinery of mitochondria (Hollenbeck and Saxton, 2005; Gutnick et al., 2019; Rangaraju et al., 2019). It is still unclear how mitochondrial transport is influenced by actin filaments. In 2010, it was published that mitochondria of neuronal cells in *Drosophila melanogaster* show higher motility in the absence of MYO5 actin motor proteins (Pathak et al., 2010). Years later it was further reported that mitochondria in axons of mammalian hippocampal neurons show an increased motility following actin filament polymerization is blocked by latrunculin A (Gutnick et al., 2019). Furthermore, a rapid calcium induced actin polymerization at the endoplasmic reticulum by Inverted formin 2 leads to transient immobilization of organelles (Wales et al., 2016). In combination with the knowledge that SPIRE proteins cooperate with FMN subfamily formins to facilitate actin filament polymerization (Quinlan and Kerkhoff, 2008; Dietrich et al., 2013; Alzahofi, Robinson, Welz et al., 2018), it is not surprising that mitoSPIRE1 influences mitochondrial motility. The influence of mitoSPIRE1 on mitochondrial motility might be explained by a local actin network at mitochondria produced by mitoSPIRE1 and FMN subfamily proteins. To understand in detail how these local actin filaments could influence the transport of mitochondria, further investigations are necessary. In addition, the experiments performed in pMEFs to investigate mitochondrial motility have to be repeated in neuronal cells. This would also clarify if we detected a cell specific effect of mitoSPIRE1 or if mitoSPIRE1 might play a much larger systemic role by finally influencing the integrity of neuronal networks.

4.9 Model for mitoSPIRE1 function in mitochondrial transport processes

The transport of mitochondria along cytoskeletal components enables the cell to provide all intracellular compartments with energy in the form of ATP (Hollenbeck and Saxton, 2005). Besides their movement, the target-oriented anchoring of mitochondria at synapses or other cell areas which have a high demand of energy seems to be important as well (Li et al., 2004; Sheng, 2014; van Bergeijk et al., 2016; Ashrafi and Ryan, 2017; Rangaraju et al., 2019).

Transport, replenishment, and reuptake of synaptic vesicles are highly energy consuming processes, which are impaired by an insufficient supply with ATP (Sheng, 2014). However, stationary mitochondria pools at active pre-synaptic boutons in axons facilitate a constant ATP supply, while motile mitochondria passing through the active synapses only provide a temporary ATP supply, which reduces synaptic energy levels. To avoid a depleted ATP supply, motile mitochondria can become stationary (Sheng, 2014). In line with axonal synapses the function of dendritic spines is also dependent on local stationary mitochondria pools. In this context, it was shown that stable mitochondrial compartments fuel local translation during induced neuronal plasticity (Rangaraju et al., 2019). To immobilize mitochondria in axonal compartments the syntaphilin protein anchors the organelle directly at microtubules (Kang et al., 2008; Chen et al., 2009). Not surprisingly, the absence of syntaphilin in hippocampal neurons increases the general axonal mitochondria motility and mitochondria fail to stop at activated pre-synapses. Nevertheless, mitochondria of dendrites are not affected by the loss of syntaphilin and are still recruited to active synapses (Chen and Sheng, 2013). However, it is hypothesized that stationary mitochondria of both dendritic post-synaptic spines and axonal pre-synaptic sites are anchored to actin filaments (Gutnick et al., 2019; Rangaraju et al., 2019). Those facts indicate that the mitochondrial transport system is highly complex and has several mechanisms to stop and anchor motile mitochondria at specific intracellular positions.

From the work presented in this thesis, we conclude that the mitochondrial mitoSPIRE1 protein might be able to cooperate with FMN subfamily formins and MYO5 motor proteins at the mitochondrial surface. Furthermore, the loss of mitoSPIRE1 increases the motility of mitochondria in pMEFs. Based on these results and on the present literature we propose a model in which the mitoSPIRE1 protein interacts with FMN formins to produce a local actin meshwork at mitochondrial membranes (Figure 24). Furthermore, we propose that mitoSPIRE1 translocates the myosin 5 actin motor protein function towards mitochondria to provide anchoring to the actin cytoskeleton by the interaction of myosin motor domains with the actin

network. In our model, the functional protein complex of SPIRE, FMN and MYO5 provides a mitochondrial anchor system, which facilitates mitochondria to be spatially stationary. The mitoSPIRE1 protein might therefore function similarly to its vesicular counterpart in organizing local actin / myosin networks, but the mitoSPIRE1 generated actin meshwork seems to facilitate mitochondria positioning and not mitochondria transport. The number of actin motor proteins on an individual organelle / vesicle might differentiate between motility and anchoring. This model is in line with the observation that the absence of mitoSPIRE1 increases mitochondrial motility in pMEFs.

The model proposed herein for mitochondrial transport describes that mitoSPIRE1 is able to cooperate with FMN subfamily formins to produce a local actin meshwork at mitochondria, as it was already described for the transport of RAB11 vesicles and melanosomes (Schuh, 2011; Alzahofi, Robinson, Welz et al., 2018). In contrast to RAB11 vesicles and melanosomes, we propose that these actin filaments are not used for transport but rather to anchor the mitochondria at specific positions. In this context, the positioning of mitochondria could be facilitated by an actin meshwork containing randomly oriented actin filaments. As a consequence, myosin motor proteins could walk along polarized actin filaments in distinct directions, block each other in forward movement and would finally stabilize the mitochondria at a specific position. Myosin motor proteins could also just bind the actin filament and freeze in a certain position to block mitochondria movement and work finally as an anchor. It is most likely that MYO5 motors are involved in these processes, because these proteins colocalize with mitoSPIRE1 and MYO5 is already associated to arrest kinesin-driven cargoes in the axon initial segment, which is an actin-rich region (Janssen et al., 2017). Finally, our predicted mitochondrial transport model is supported by the fact that myosin motors are reported before to participate in the tethering and positioning of many other organelles at actin filaments (Venkatesh et al., 2019).

However, the hypothesized mitochondria anchoring system organized by mitoSPIRE1 seems to be highly energy consuming compared to immobilization of mitochondria by syntaphilin. The anchor mechanism mediated by syntaphilin seems to be an area specific system for neuronal axons and anchors mitochondria at microtubules but not at actin filaments (Kang et al., 2008; Chen et al., 2009). Actin filaments have been proposed to aid transport processes within cell areas where rigid microtubules are not available (Kneussel and Wagner, 2013). This would explain why the cell needs an actin dependent anchor system for organelles. In agreement with syntaphilin, it could be that there is an unknown protein / (complex) which immobilizes

mitochondria at actin filaments as well. Furthermore, actin rich regions have been suggested to inhibit cargo movement by itself (Venkatesh et al., 2019) and it is an additional option to explain the mitoSPIRE1 influence on mitochondria motility. In this context, the enrichment of actin filaments synthesized by a mitoSPIRE1 / FMN complex at mitochondria act as an insurmountable obstacle for mitochondrial transport, and mitochondria are captured at their current position until actin filaments are depolarized. Nevertheless, our results and accumulating evidence from other scientists indicate that actin filaments serve as an anchor system in the mitochondrial transport machinery, and not as transport tracks (Pathak et al., 2010; Gutnick et al., 2019; Rangaraju et al., 2019). The absence of the actin based mitochondrial anchor system facilitated by mitoSPIRE1 could influence the stationary mitochondria pools in synapses and therefore impair neuronal plasticity. Impairments in synaptic plasticity interfere with learning processes and memory formation and thus could finally influence the behavior of the whole organism and explain the fear conditioning phenotype of *SPIRE1* mutant mice, lacking the expression of proteins from the *SPIRE1* gene. Furthermore, the loss of actin-based stationary mitochondria pools could influence pre-synaptic neurotransmitter release and therefore the behavior of an organism, may explain the fear phenotype of *SPIRE1* mutant mice as well.

To confirm the existence of a mitoSPIRE1 mediated anchor system of mitochondria at actin filaments, further experiments are necessary. In this context, mitochondria motility assays of mitoSPIRE1 knockout neurons have to be done. In addition, the novel mitoSPIRE1 knockout mouse has to be tested in fear conditioning experiments to investigate if the in vitro phenotypes influence animal behavior.

The actin nucleators SPIRE and FMN subfamily formins directly interact strongly with each other and form a functional actin nucleator complex at intracellular membranes (Pechlivanis et al., 2009; Pfender et al., 2011; Schuh, 2011; Alzahofi, Robinson, Welz et al., 2018). Based on this, it seems counterintuitive that *SPIRE1* mutant and FMN2 knockout mouse models display different phenotypes in fear conditioning experiments (Peleg et al., 2010; Pleiser et al., 2014; Agís-Balboa et al., 2017). Further analysis needs to be done to clarify why these mouse models show a difference in fear behavior.

Based on our results presented in this thesis and on the present literature, we propose a novel model for mitochondria anchoring at actin filaments mediated by the mitochondria associated actin nucleator mitoSPIRE1. In conclusion, the here-hypothesized mitoSPIRE1-mediated

actin-based anchor system of mitochondria might be important for several neurological functions, including neuroplasticity or neurotransmitter release, and could therefore especially influence fear behavior.

5. References

- Agís-Balboa RC, Pinhero PS, Rebola N, Kerimoglu C, Benito E, Gertig M, Bahari-Javan S, Jain G, Burkhardt S, Delalle I, Jatzko A, Dettenhofer M, Zunszain PA, Schmitt A, Falkai P, Pape JC, Binder EB, Mülle C, Fischer A, Sananbenesi F. (2017) Formin 2 links neuropsychiatric phenotypes at young age to an increased risk for dementia. *EMBO J.* 36:2815-2828.
- Alzahofi N, Robinson CL, Welz T, Page EL, Briggs DA, Stainthorp AK, Reekes J, Elbe DA, Straub F, Tate EW, Goff PS, Sviderskaya EV, Cantero M, Montoliu L, Bailly M, Kerkhoff E, Hume A. (2018) Rab27a co-ordinates actin-dependent transport by controlling organelle-associated motors and track assembly proteins. *bioRxiv*. doi.org/10.1101/314153.
- Amiott EA, Lott P, Soto J, Kang PB, McCaffery JM, DiMauro S, Abel ED, Flanigan KM, Lawson VH, Shaw JM. (2008) Mitochondrial fusion and function in Charcot-Marie-Tooth type 2A patient fibroblasts with mitofusin 2 mutations. *Exp Neurol.* 211:115-27.
- Andritschke D, Dilling S, Emmenlauer M, Welz T, Schmich F, Misselwitz B, Rämö P, Rottner K, Kerkhoff E, Wada T, Penninger JM, Beerenwinkel N, Horvath P, Dehio C, Hardt WD. (2016) A Genome-Wide siRNA Screen Implicates Spire1/2 in SipA-Driven Salmonella Typhimurium Host Cell Invasion. *PLoS One.* 11:e0161965.
- Archer SL. (2013) Mitochondrial dynamics - mitochondrial fission and fusion in human diseases. *N Engl J Med.* 369:2236-51.
- Ashrafi G, Ryan TA. (2017) Glucose metabolism in nerve terminals. *Curr Opin Neurobiol.* 45:156-161.
- Baas PW, Black MM, Banker GA. (1989) Changes in microtubule polarity orientation during the development of hippocampal neurons in culture. *J Cell Biol.* 109:3085-94.
- Baas PW, Deitch JS, Black MM, Banker GA. (1988) Polarity orientation of microtubules in hippocampal neurons: uniformity in the axon and nonuniformity in the dendrite. *Proc Natl Acad Sci U S A.* 85:8335-9.
- Berg JS, Powell BC, Cheney RE. (2001) A millennial myosin census. *Mol Biol Cell.* 12:780-94.
- Bonora M, Patergnani S, Rimessi A, de Marchi E, Suski JM, Bononi A, Giorgi C, Marchi S, Missiroli S, Poletti F, Wieckowski MR, Pinton P. (2012) ATP synthesis and storage. *Purinergic Signal.* 8:343-357.
- Cağdaş D, Özgür TT, Asal GT, Tezcan I, Metin A, Lambert N, de Saint Basile G, Sanal O. (2012) Griscelli syndrome types 1 and 3: analysis of four new cases and long-term evaluation of previously diagnosed patients. *Eur J Pediatr.* 171:1527-31.
- Cai Q, Gerwin C, Sheng ZH. (2005) Syntabulin-mediated anterograde transport of mitochondria along neuronal processes. *J Cell Biol.* 170:959-69.
- Cai Q, Zakaria HM, Simone A, Sheng ZH. (2012) Spatial parkin translocation and degradation of damaged mitochondria via mitophagy in live cortical neurons. *Curr Biol.* 22:545-52.

- Carlier MF, Husson C, Renault L, Didry D. (2011) Control of actin assembly by the WH2 domains and their multifunctional tandem repeats in Spire and Cordon-Bleu. *Int Rev Cell Mol Biol.* 290:55-85.
- Castellanos E, Lanning NJ. (2019) Phosphorylation of OXPHOS Machinery Subunits: Functional Implications in Cell Biology and Disease. *Yale J Biol Med.* 92:523-531.
- Chang DT, Reynolds IJ. (2006) Mitochondrial trafficking and morphology in healthy and injured neurons. *Prog Neurobiol.* 80:241-68.
- Chen H, Chan DC. (2009) Mitochondrial dynamics--fusion, fission, movement, and mitophagy--in neurodegenerative diseases. *Hum Mol Genet.* 18:R169-76.
- Chen H, Chan DC. (2010) Physiological functions of mitochondrial fusion. *Ann N Y Acad Sci.* 1201:21-5.
- Chen H, Detmer SA, Ewald AJ, Griffin EE, Fraser SE, Chan DC. (2003) Mitofusins Mfn1 and Mfn2 coordinately regulate mitochondrial fusion and are essential for embryonic development. *J Cell Biol.* 160:189-200.
- Chen Y, Sheng ZH. (2013) Kinesin-1-syntaphilin coupling mediates activity-dependent regulation of axonal mitochondrial transport. *J Cell Biol.* 202:351-64.
- Chen YM, Gerwin C, Sheng ZH. (2009) Dynein light chain LC8 regulates syntaphilin-mediated mitochondrial docking in axons. *J Neurosci.* 29:9429-38.
- Cheney RE, O'Shea MK, Heuser JE, Coelho MV, Wolenski JS, Espreafico EM, Forscher P, Larson RE, Mooseker MS. (1993) Brain myosin-V is a two-headed unconventional myosin with motor activity. *Cell.* 75:13-23.
- Chevalier-Larsen E, Holzbaur EL. (2006) Axonal transport and neurodegenerative disease. *Biochim Biophys Acta.* 1762:1094-108.
- Costes SV, Daelemans D, Cho EH, Dobbin Z, Pavlakis G, Lockett S. (2004) Automatic and quantitative measurement of protein-protein colocalization in live cells. *Biophys J.* 86:3993-4003.
- D'Orazio J, Jarrett S, Amaro-Ortiz A, Scott T. (2013) UV Radiation and the Skin. *Int J Mol Sci.* 14:12222-12248.
- Dahlgaard K, Raposo AA, Niccoli T, St Johnston D. (2007) Capu and Spire assemble a cytoplasmic actin mesh that maintains microtubule organization in the *Drosophila* oocyte. *Dev Cell.* 13:539-53.
- Dietrich S, Weiß S, Pleiser S, Kerkhoff E. (2013) Structural and functional insights into the Spir/formin actin nucleator complex. *Biol Chem.* 394:1649-60.
- Doench JG, Fusi N, Sullender M, Hegde M, Vaimberg EW, Donovan KF, Smith I, Tothova Z, Wilen C, Orchard R, Virgin HW, Listgarten J, Root DE. (2016) Optimized sgRNA design to maximize activity and minimize off-target effects of CRISPR-Cas9. *Nat Biotechnol.* 34:184-191.

- Dominguez R, Holmes KC. (2011) Actin structure and function. *Annu Rev Biophys.* 40:169-86.
- Dumas JJ, Merithew E, Sudharshan E, Rajamani D, Hayes S, Lawe D, Corvera S, Lambright DG. (2001) Multivalent endosome targeting by homodimeric EEA1. *Mol Cell.* 8:947-58.
- Dumont J, Million K, Sunderland K, Rassinier P, Lim H, Leader B, Verlhac MH. (2007) Formin-2 is required for spindle migration and for the late steps of cytokinesis in mouse oocytes. *Dev Biol.* 301:254-65.
- Espindola FS, Suter DM, Partata LB, Cao T, Wolenski JS, Cheney RE, King SM, Mooseker MS. (2000) The light chain composition of chicken brain myosin-Va: calmodulin, myosin-II essential light chains, and 8-kDa dynein light chain/PIN. *Cell Motil Cytoskeleton.* 47:269-81.
- Espreafico EM, Cheney RE, Matteoli M, Nascimento AA, De Camilli PV, Larson RE, Mooseker MS. (1992) Primary structure and cellular localization of chicken brain myosin-V (p190), an unconventional myosin with calmodulin light chains. *J Cell Biol.* 119:1541-57.
- Evans RD, Robinson C, Briggs DA, Tooth DJ, Ramalho JS, Cantero M, Montoliu L, Patel S, Sviderskaya EV, Hume AN. (2014) Myosin-Va and dynamic actin oppose microtubules to drive long-range organelle transport. *Curr Biol.* 24:1743-50.
- Fagarasanu A, Mast FD, Knoblach B, Jin Y, Brunner MJ, Logan MR, Glover JN, Eitzen GA, Aitchison JD, Weisman LS, Rachubinski RA. (2009) Myosin-driven peroxisome partitioning in *S. cerevisiae*. *J Cell Biol.* 186:541-54.
- Firat-Karalar EN, Welch MD. (2011) New mechanisms and functions of actin nucleation. *Curr Opin Cell Biol.* 23:4-13.
- Fletcher DA, Mullins RD. (2010) Cell mechanics and the cytoskeleton. *Nature.* 463:485-492.
- Friedman JR, Lackner LL, West M, DiBenedetto JR, Nunnari J, Voeltz GK. (2011) ER tubules mark sites of mitochondrial division. *Science.* 334:358-62.
- Fukuda M, Kuroda TS, Mikoshiba K. (2002) Slac2-a/melanophilin, the missing link between Rab27 and myosin Va: implications of a tripartite protein complex for melanosome transport. *J Biol Chem.* 277:12432-6.
- Fukuda M. (2013) Rab27 effectors, pleiotropic regulators in secretory pathways. *Traffic.* 14:949-63.
- Gewirtz JC, McNish KA, Davis M. (2000) Is the hippocampus necessary for contextual fear conditioning?. *Behav Brain Res.* 110:83-95.
- Glater EE, Megeath LJ, Stowers RS, Schwarz TL. (2006) Axonal transport of mitochondria requires Milton to recruit kinesin heavy chain and is light chain independent. *J Cell Biol.* 173:545-557.

- Górska-Andrzejak J, Stowers RS, Borycz J, Kostyleva R, Schwarz TL, Meinertzhagen IA. (2003) Mitochondria are redistributed in *Drosophila* photoreceptors lacking Milton, a kinesin-associated protein. *J Comp Neurol.* 463:372-88.
- Guo X, Macleod GT, Wellington A, Hu F, Panchumarthi S, Schoenfield M, Marin L, Charlton MP, Atwood HL, Zinsmaier KE. (2005) The GTPase dMiro is required for axonal transport of mitochondria to *Drosophila* synapses. *Neuron.* 47:379-93.
- Gutnick A, Banghart MR, West ER, Schwarz TL. (2019) The light-sensitive dimerizer Zapalogue reveals distinct modes of immobilization for axonal mitochondria. *Nat Cell Biol.* 21:768-777.
- Hall B, Limaye A, Kulkarni AB. (2009) Overview: generation of gene knockout mice. *Curr Protoc Cell Biol.* 19.12.1-17.
- Hamdan FF, Gauthier J, Araki Y, Lin DT, Yoshizawa Y, Higashi K, Park AR, Spiegelman D, Dobrzeniecka S, Piton A, Tomitori H, Daoud H, Massicotte C, Henrion E, Diallo O, S2D Group, Shekarabi M, Marineau C, Shevell M, Maranda B, Mitchell G, Nadeau A, D'Anjou G, Vanasse M, Srour M, Lafrenière RG, Drapeau P, Lacaille JC, Kim E, Lee JR, Igarashi K, Hagan RL, Rouleau GA, Michaud JL. (2011) Excess of de novo deleterious mutations in genes associated with glutamatergic systems in nonsyndromic intellectual disability. *Am J Hum Genet.* 88:306-16.
- Hammer JA, Sellers JR. (2011) Walking to work: roles for class V myosins as cargo transporters. *Nat Rev Mol Cell Biol.* 13:13-26.
- Hartman MA, Spudich JA. (2012) The myosin superfamily at a glance. *J Cell Sci.* 125:1627-32.
- Hatch AL, Gurel PS, Higgs HN. (2014) Novel roles for actin in mitochondrial fission. *J Cell Sci.* 127:4549-60.
- Heidemann SR, Landers JM, Hamborg MA. (1981) Polarity orientation of axonal microtubules. *J Cell Biol.* 91:661-5.
- Hirokawa N, Niwa S, Tanaka Y. (2010) Molecular motors in neurons: transport mechanisms and roles in brain function, development, and disease. *Neuron.* 68:610-38.
- Hirokawa N, Noda Y, Tanaka Y, Niwa S. (2009) Kinesin superfamily motor proteins and intracellular transport. *Nat Rev Mol Cell Biol.* 10:682-96.
- Hollenbeck PJ, Saxton WM. (2005) The axonal transport of mitochondria. *J Cell Sci.* 118:5411-9.
- Houdusse A, Sweeney HL. (2016) How myosin generates force on actin filaments. *Trends Biochem Sci.* 41:989-997.
- Hsu PD, Scott DA, Weinstein JA, Ran FA, Konermann S, Agarwala V, Li Y, Fine EJ, Wu X, Shalem O, Cradick TJ, Marraffini LA, Bao G, Zhang F. (2013) DNA targeting specificity of RNA-guided Cas9 nucleases. *Nat Biotechnol.* 31:827-32.

- Huizing M, Helip-Wooley A, Westbroek W, Gunay-Aygun M, Gahl WA. (2008) Disorders of lysosome-related organelle biogenesis: clinical and molecular genetics. *Annu Rev Genomics Hum Genet.* 9:359-86.
- Hume AN, Collinson LM, Hopkins CR, Strom M, Barral DC, Bossi G, Griffiths GM, Seabra MC. (2002) The leaden gene product is required with Rab27a to recruit myosin Va to melanosomes in melanocytes. *Traffic.* 3:193-202.
- Hume AN, Collinson LM, Rapak A, Gomes AQ, Hopkins CR, Seabra MC. (2001) Rab27a regulates the peripheral distribution of melanosomes in melanocytes. *J Cell Biol.* 152:795-808.
- Hurd DD, Saxton WM. (1996) Kinesin mutations cause motor neuron disease phenotypes by disrupting fast axonal transport in *Drosophila*. *Genetics.* 144:1075-85.
- Ingwall JS. (2009) Energy Metabolism in Heart Failure and Remodelling. *Cardiovasc Res.* 81:412-9.
- Ishihara N, Nomura M, Jofuku A, Kato H, Suzuki SO, Masuda K, Otera H, Nakanishi Y, Nonaka I, Goto Y, Taguchi N, Morinaga H, Maeda M, Takayanagi R, Yokota S, Mihara K. (2009) Mitochondrial fission factor Drp1 is essential for embryonic development and synapse formation in mice. *Nat Cell Biol.* 11:958-66.
- Janak PH, Tye KM. (2015) From circuits to behavior in the amygdala. *Nature.* 517:284-92.
- Janssen AFJ, Tas RP, van Bergeijk P, Oost R, Hoogenraad CC, Kapitein LC. (2017) Myosin-V Induces Cargo Immobilization and Clustering at the Axon Initial Segment. *Front Cell Neurosci.* 11:260.
- Kang JS, Tian JH, Pan PY, Zald P, Li C, Deng C, Sheng ZH. (2008) Docking of axonal mitochondria by syntaphilin controls their mobility and affects short-term facilitation. *Cell.* 132:137-48.
- Kerkhoff E, Simpson JC, Leberfinger CB, Otto IM, Doerks T, Bork P, Rapp UR, Raabe T, Pepperkok R. (2001) The Spir actin organizers are involved in vesicle transport processes. *Curr Biol.* 11:1963-8.
- Kerkhoff E. (2006) Cellular functions of the Spir actin-nucleation factors. *Trends Cell Biol.* 16:477-83.
- Kerkhoff E. (2011) Actin dynamics at intracellular membranes: the Spir/formin nucleator complex. *Eur J Cell Biol.* 90:922-5.
- Kinsey ST, Locke BR, Dillaman RM. (2011) Molecules in motion: influences of diffusion on metabolic structure and function in skeletal muscle. *J Exp Biol.* 214:263-74.
- Kirschner M, Mitchison T. (1986) Beyond self-assembly: from microtubules to morphogenesis. *Cell.* 45:329-42.
- Kline-Smith SL, Walczak CE. (2004) Mitotic spindle assembly and chromosome segregation: refocusing on microtubule dynamics. *Mol Cell.* 15:317-27.

- Kneussel M, Wagner W. (2013) Myosin motors at neuronal synapses: drivers of membrane transport and actin dynamics. *Nat Rev Neurosci.* 14:233-47.
- Knobloch HS, Charlet A, Hoffmann LC, Eliava M, Khrulev S, Cetin AH, Osten P, Schwarz MK, Seeburg PH, Stoop R, Grinevich V. (2012) Evoked axonal oxytocin release in the central amygdala attenuates fear response. *Neuron.* 73:553-66.
- Knowles BC, Roland JT, Krishnan M, Tyska MJ, Lapierre LA, Dickman PS, Goldenring JR, Shub MD. (2014) Myosin Vb uncoupling from RAB8A and RAB11A elicits microvillus inclusion disease. *J Clin Invest.* 124:2947-62.
- Kollmar M, Welz T, Straub F, Alzahofi N, Hatje K, Briggs DA, Samol-Wolf A, Burkhardt P, Hume A, Kerkhoff E. (2019) Animal evolution coincides with a novel degree of freedom in exocytic transport processes. *bioRxiv.* doi.org/10.1101/591974.
- Korobova F, Gauvin TJ, Higgs HN. (2014) A role for myosin II in mammalian mitochondrial fission. *Curr Biol.* 24:409-14.
- Korobova F, Ramabhadran V, Higgs HN. (2013) An actin-dependent step in mitochondrial fission mediated by the ER-associated formin INF2. *Science.* 339:464-467.
- Kraus F, Ryan MT. (2017) The constriction and scission machineries involved in mitochondrial fission. *J Cell Sci.* 130:2953-2960.
- Lackner LL, Nunnari JM. (2009) The molecular mechanism and cellular functions of mitochondrial division. *Biochim Biophys Acta.* 1792:1138-44.
- Langford GM. (1995) Actin- and microtubule-dependent organelle motors: interrelationships between the two motility systems. *Curr Opin Cell Biol.* 7:82-8.
- Law R, Dixon-Salazar T, Jerber J, Cai N, Abbasi AA, Zaki MS, Mittal K, Gabriel SB, Rafiq MA, Khan V, Nguyen M, Ali G, Copeland B, Scott E, Vasli N, Mikhailov A, Khan MN, Andrade DM, Ayaz M, Ansar M, Ayub M, Vincent JB, Gleeson JG. (2014) Biallelic truncating mutations in FMN2, encoding the actin-regulatory protein Formin 2, cause nonsyndromic autosomal-recessive intellectual disability. *Am J Hum Genet.* 95:721-8.
- Leader B, Lim H, Carabatsos MJ, Harrington A, Ecsedy J, Pellman D, Maas R, Leder P. (2002) Formin-2, polyploidy, hypofertility and positioning of the meiotic spindle in mouse oocytes. *Nat Cell Biol.* 4:921-8.
- Lee JE, Westrate LM, Wu H, Page C, Voeltz GK. (2016) Multiple dynamin family members collaborate to drive mitochondrial division. *Nature.* 540:139-143.
- Lenaers G, Hamel C, Delettre C, Amati-Bonneau P, Procaccio V, Bonneau D, Reynier P, Milea D. (2012) Dominant optic atrophy. *Orphanet J Rare Dis.* 7:46.
- Li S, Xu S, Roelofs BA, Boyman L, Lederer WJ, Sesaki H, Karbowski M. (2015) Transient assembly of F-actin on the outer mitochondrial membrane contributes to mitochondrial fission. *J Cell Biol.* 208:109-23.
- Li Z, Okamoto K, Hayashi Y, Sheng M. (2004) The importance of dendritic mitochondria in the morphogenesis and plasticity of spines and synapses. *Cell.* 119:873-87.

- Liesa M, Palacín M, Zorzano A. (2009) Mitochondrial dynamics in mammalian health and disease. *Physiol Rev.* 89:799-845.
- Lisé MF, Wong TP, Trinh A, Hines RM, Liu L, Kang R, Hines DJ, Lu J, Goldenring JR, Wang YT, El-Husseini A. (2006) Involvement of myosin Vb in glutamate receptor trafficking. *J Biol Chem.* 281:3669-78.
- Lopes VS, Ramalho JS, Owen DM, Karl MO, Strauss O, Futter CE, Seabra MC. (2007) The ternary Rab27a-Myrip-Myosin VIIa complex regulates melanosome motility in the retinal pigment epithelium. *Traffic.* 8:486-99.
- MacAskill AF, Rinholm JE, Twelvetrees AE, Arancibia-Carcamo IL, Muir J, Fransson A, Aspenstrom P, Attwell D, Kittler JT. (2009) Miro1 is a calcium sensor for glutamate receptor-dependent localization of mitochondria at synapses. *Neuron.* 61:541-55.
- MacDonald JA, Bothun AM, Annis SN, Sheehan H, Ray S, Gao Y, Ivanov AR, Khrapko K, Tilly JL, Woods DC. (2019) A nanoscale, multi-parametric flow cytometry-based platform to study mitochondrial heterogeneity and mitochondrial DNA dynamics. *Commun Biol.* 2:258.
- Manczak M, Sesaki H, Kageyama Y, Reddy PH. (2012) Dynamin-related protein 1 heterozygote knockout mice do not have synaptic and mitochondrial deficiencies. *Biochim Biophys Acta.* 1822:862-74.
- Mandal A, Drerup CM. (2019) Axonal Transport and Mitochondrial Function in Neurons. *Front Cell Neurosci.* 13:373.
- Manor U, Bartholomew S, Golani G, Christenson E, Kozlov M, Higgs H, Spudich J, Lippincott-Schwartz J. (2015) A mitochondria-anchored isoform of the actin-nucleating spire protein regulates mitochondrial division. *Elife.* 4:e08828.
- Manseau LJ, Schüpbach T. (1989) Cappuccino and Spire: Two Unique Maternal-Effect Loci Required for Both the Anteroposterior and Dorsoventral Patterns of the Drosophila Embryo. *Genes Dev.* 3:1437-52.
- Matesic LE, Yip R, Reuss AE, Swing DA, O'Sullivan TN, Fletcher CF, Copeland NG, Jenkins NA. (2001) Mutations in *Mlph*, encoding a member of the Rab effector family, cause the melanosome transport defects observed in leaden mice. *Proc Natl Acad Sci U S A.* 98:10238-43.
- Medler K, Gleason EL. (2002) Mitochondrial Ca(2+) buffering regulates synaptic transmission between retinal amacrine cells. *J Neurophysiol.* 87:1426-39.
- Mercer JA, Seperack PK, Strobel MC, Copeland NG, Jenkins NA. (1991) Novel myosin heavy chain encoded by murine dilute coat colour locus. *Nature.* 349:709-13.
- Miller KE, Sheetz MP. (2004) Axonal mitochondrial transport and potential are correlated. *J Cell Sci.* 117:2791-804.
- Misra S, Hurley JH. (1999) Crystal structure of a phosphatidylinositol 3-phosphate-specific membrane-targeting motif, the FYVE domain of Vps27p. *Cell.* 97:657-66.

- Mogensen M, Sahlin K, Fernström M, Glintborg D, Vind BF, Beck-Nielsen H, Højlund K. (2007) Mitochondrial respiration is decreased in skeletal muscle of patients with type 2 diabetes. *Diabetes*. 56:1592-9.
- Mogessie B, Scheffler K, Schuh M. (2018) Assembly and Positioning of the Oocyte Meiotic Spindle. *Annu Rev Cell Dev Biol*. 34:381-403.
- Montaville P, Jégou A, Pernier J, Compper C, Guichard B, Mogessie B, Schuh M, Romet-Lemonne G, Carlier MF. (2014) Spire and Formin 2 synergize and antagonize in regulating actin assembly in meiosis by a ping-pong mechanism. *PLoS Biol*. 12:e1001795.
- Nagashima K, Torii S, Yi Z, Igarashi M, Okamoto K, Takeuchi T, Izumi T. (2002) Melanophilin directly links Rab27a and myosin Va through its distinct coiled-coil regions. *FEBS Lett*. 517:233-8.
- Nicholls DG, Budd SL. (2000) Mitochondria and neuronal survival. *Physiol Rev*. 80:315-60.
- Oberhofer A, Spieler P, Rosenfeld Y, Stepp WL, Cleetus A, Hume AN, Mueller-Planitz F, Ökten Z. (2017) Myosin Va's adaptor protein melanophilin enforces track selection on the microtubule and actin networks in vitro. *Proc Natl Acad Sci U S A*. 114:E4714-E4723.
- Otomo T, Tomchick DR, Otomo C, Panchal SC, Machius M, Rosen MK. (2005) Structural basis of actin filament nucleation and processive capping by a formin homology 2 domain. *Nature*. 433:488-94.
- Otto IM, Raabe T, Rennefahrt UE, Bork P, Rapp UR, Kerkhoff E. (2000) The p150-Spir protein provides a link between c-Jun N-terminal kinase function and actin reorganization. *Curr Biol*. 10:345-8.
- Pagliuso A, Cossart P, Stavru F. (2018) The ever-growing complexity of the mitochondrial fission machinery. *Cell Mol Life Sci*. 75:355-374.
- Pathak D, Sepp KJ, Hollenbeck PJ. (2010) Evidence that myosin activity opposes microtubule-based axonal transport of mitochondria. *J Neurosci*. 30:8984-92.
- Paul AS, Pollard TD. (2008) The role of the FH1 domain and profilin in formin-mediated actin-filament elongation and nucleation. *Curr Biol*. 18:9-19.
- Pechlivanis M, Samol A, Kerkhoff E. (2009) Identification of a short Spir interaction sequence at the C-terminal end of formin subgroup proteins. *J Biol Chem*. 284:25324-33.
- Peleg S, Sananbenesi F, Zovoilis A, Burkhardt S, Bahari-Javan S, Agis-Balboa RC, Cota P, Wittnam JL, Gogol-Doering A, Opitz L. (2010) Altered histone acetylation is associated with age-dependent memory impairment in mice. *Science*. 328:753-6.
- Pfender S, Kuznetsov V, Pleiser S, Kerkhoff E, Schuh M. (2011) Spire-type actin nucleators cooperate with Formin-2 to drive asymmetric oocyte division. *Curr Biol*. 21:955-60.

- Pilling AD, Horiuchi D, Lively CM, Saxton WM. (2006) Kinesin-1 and Dynein are the primary motors for fast transport of mitochondria in *Drosophila* motor axons. *Mol Biol Cell*. 17:2057-68.
- Pleiser S, Banchaabouchi MA, Samol-Wolf A, Farley D, Welz T, Wellbourne-Wood J, Gehring I, Linkner J, Faix J, Riemenschneider MJ, Dietrich S, Kerkhoff E. (2014) Enhanced fear expression in *Spir-1* actin organizer mutant mice. *Eur J Cell Biol*. 93:225-37.
- Pleiser S, Rock R, Wellmann J, Gessler M, Kerkhoff E. (2010) Expression patterns of the mouse *Spir-2* actin nucleator. *Gene Expr Patterns*. 10:345-50.
- Pleiser S. (2012) Mouse genetic analyses of *Spir* functions. dissertation. Julius-Maximilians-University Würzburg.
- Pollard TD, Cooper JA. (2009) Actin, a central player in cell shape and movement. *Science*. 326:1208-12.
- Pollard TD, Goldman RD. (2016) The cytoskeleton. Cold Spring Harbor Laboratory Press. 978-1621820161.
- Pollard TD. (2016) Actin and Actin-Binding Proteins. Cold Spring Harb Perspect Biol. 8:a018226.
- Pompey SN, Michaely P, Luby-Phelps K. (2013) Quantitative fluorescence co-localization to study protein-receptor complexes. *Methods Mol Biol*. 1008:439-53.
- Provance DW, James TL, Mercer JA. (2002) Melanophilin, the product of the *leaden* locus, is required for targeting of myosin-Va to melanosomes. *Traffic*. 3:124-32.
- Pylypenko O, Welz T, Tittel J, Kollmar M, Malherbes G, Weiss S, Michel C, Samol-Wolf A, Grasskamp A, Hume A, Goud B, Baron B, England P, Schwillle P, Weidemann T, Houdusse A, Kerkhoff E. (2016) Coordinated recruitment of *Spir* actin nucleators and myosin V motors to Rab11 vesicle membranes. *eLife*. 5:e17523.
- Quinlan ME, Kerkhoff E. (2008) Actin nucleation: bacteria get in-Spired. *Nat Cell Biol*. 10:13-15.
- Quinlan ME, Heuser JE, Kerkhoff E, Mullins RD. (2005) *Drosophila* Spire is an actin nucleation factor. *Nature*. 433:382-8.
- Quinlan ME, Hilgert S, Bedrossian A, Mullins RD, Kerkhoff E. (2007) Regulatory interactions between two actin nucleators, Spire and Cappuccino. *J Cell Biol*. 179:117-128.
- Ramabhadran V, Korobova F, Rahme GJ, Higgs HN. (2011) Splice variant-specific cellular function of the formin INF2 in maintenance of Golgi architecture. *Mol Biol Cell*. 22:4822-33.
- Ramalho JS, Lopes VS, Tarafder AK, Seabra MC, Hume AN. (2009) Myrip uses distinct domains in the cellular activation of myosin VA and myosin VIIA in melanosome transport. *Pigment Cell Melanoma Res*. 22:461-73.

- Ran FA, Hsu PD, Wright J, Agarwala V, Scott DA, Zhang F. (2013) Genome engineering using the CRISPR-Cas9 system. *Nat Protoc.* 8:2281-2308.
- Rangaraju V, Lauterbach M, Schuman EM. (2019) Spatially Stable Mitochondrial Compartments Fuel Local Translation during Plasticity. *Cell.* 176:73-84.
- Raposo G, Marks MS. (2007) Melanosomes - dark organelles enlighten endosomal membrane transport. *Nat Rev Mol Cell Biol.* 8:786-97.
- Reck-Peterson SL, Novick PJ, Mooseker MS. (1999) The tail of a yeast class V myosin, myo2p, functions as a localization domain. *Mol Biol Cell.* 10:1001-17.
- Robinson RC, Turbedsky K, Kaiser DA, Marchand JB, Higgs HN, Choe S, Pollard TD. (2001) Crystal structure of Arp2/3 complex. *Science.* 294:1679-1684.
- Rodriguez OC, Cheney RE. (2002) Human myosin-Vc is a novel class V myosin expressed in epithelial cells. *J Cell Sci.* 115:991-1004.
- Rogers SL, Gelfand VI. (2000) Membrane trafficking, organelle transport, and the cytoskeleton. *Curr Opin Cell Biol.* 12:57-62.
- Romero S, Le Clainche C, Didry D, Egile C, Pantaloni D, Carlier MF. (2004) Formin is a processive motor that requires profilin to accelerate actin assembly and associated ATP hydrolysis. *Cell.* 119:419-29.
- Ross JL, Ali MY, Warshaw DM. (2008) Cargo transport: molecular motors navigate a complex cytoskeleton. *Curr Opin Cell Biol.* 20:41-7.
- Rottner K, Faix J, Bogdan S, Linder S, Kerkhoff E. (2017) Actin assembly mechanisms at a glance. *J Cell Sci.* 130:3427-3435.
- Ryley DA, Wu HH, Leader B, Zimon A, Reindollar RH, Gray MR. (2005) Characterization and mutation analysis of the human formin-2 (FMN2) gene in women with unexplained infertility. *Fertil Steril.* 83:1363-71.
- Sakamoto T, Amitani I, Yokota E, Ando T. (2000) Direct observation of processive movement by individual myosin V molecules. *Biochem Biophys Res Commun.* 272:586-90.
- Schliwa M, Woehlke G. (2003) Molecular motors. *Nature.* 422:759-65.
- Schönichen A, Geyer M. (2010) Fifteen formins for an actin filament: a molecular view on the regulation of human formins. *Biochim Biophys Acta.* 1803:152-63.
- Schuh M. (2011) An actin-dependent mechanism for long-range vesicle transport. *Nat Cell Biol.* 13:1431-6.
- Schumacher N, Borawski JM, Leberfinger CB, Gessler M, Kerkhoff E. (2004) Overlapping expression pattern of the actin organizers Spir-1 and formin-2 in the developing mouse nervous system and the adult brain. *Gene Expr Patterns.* 4:249-55.
- Sehgal M, Song C, Ehlers VL, Moyer JR Jr. (2013) Learning to learn - intrinsic plasticity as a metaplasticity mechanism for memory formation. *Neurobiol Learn Mem.* 105:186-99.

- Sellers JR. (2000) Myosins: a diverse superfamily. *Biochim Biophys Acta*. 1496:3-22.
- Sept D, McCammon JA. (2001) Thermodynamics and kinetics of actin filament nucleation. *Biophys J*. 81:667-74.
- Sheng ZH. (2014) Mitochondrial trafficking and anchoring in neurons: New insight and implications. *J Cell Biol*. 204:1087-98.
- Smirnova E, Griparic L, Shurland DL, van der Blik AM. (2001) Dynamin-related protein Drp1 is required for mitochondrial division in mammalian cells. *Mol Biol Cell*. 12:2245-56.
- Smolina N, Bruton J, Kostareva A, Sejersen T. (2017) Assaying Mitochondrial Respiration as an Indicator of Cellular Metabolism and Fitness. *Methods Mol Biol*. 1601:79-87.
- Spinelli JB, Haigis MC. (2018) The multifaceted contributions of mitochondria to cellular metabolism. *Nat Cell Biol*. 20:745-754.
- Syamaladevi DP, Spudich JA, Sowdhamini R. (2012) Structural and functional insights on the Myosin superfamily. *Bioinform Biol Insights*. 6:11-21.
- Tanaka Y, Kanai Y, Okada Y, Nonaka S, Takeda S, Harada A, Hirokawa N. (1998) Targeted disruption of mouse conventional kinesin heavy chain, kif5B, results in abnormal perinuclear clustering of mitochondria. *Cell*. 93:1147-58.
- The Allen Mouse Brain Reference Atlas. (2019) <http://atlas.brain-map.org/atlas?atlas=1&plate=100960264#atlas=1&plate=100960264&resolution=16.75&x=5399.7333984375&y=3808&zoom=-3&z=6>. Mouse, P56, Coronal, image 65 of 132.
- Thomas ER, Walker LJ, Pullaperuma S, Cooper B, Brueton LA, Basile Gde S, Suri M, Brady AF. (2009) Griscelli syndrome type 1: a report of two cases and review of the literature. *Clin Dysmorphol*. 18:145-8.
- Tilelli CQ, Martins AR, Larson RE, Garcia-Cairasco N. (2003) Immunohistochemical localization of myosin Va in the adult rat brain. *Neuroscience*. 121:573-86.
- Tittel J, Welz T, Czogalla A, Dietrich S, Samol-Wolf A, Schulte M, Schwille P, Weidemann T, Kerkhoff E. (2015) Membrane targeting of the Spir·formin actin nucleator complex requires a sequential handshake of polar interactions. *J Biol Chem*. 290:6428-44.
- van Bergeijk P, Hoogenraad CC, Kapitein LC. (2016) Right Time, Right Place: Probing the Functions of Organelle Positioning. *Trends Cell Biol*. 26:121-134.
- van Bokhoven A. (2011) Genetic and epigenetic networks in intellectual disabilities. *Annu Rev Genet*. 45:81-104.
- van der Blik AM, Shen Q, Kawajiri S. (2013) Mechanisms of mitochondrial fission and fusion. *Cold Spring Harb Perspect Biol*. 5:a011072.
- van Gele M, Dynoodt P, Lambert J. (2009) Griscelli syndrome: a model system to study vesicular trafficking. *Pigment Cell Melanoma Res*. 22:268-82.

- van Spronsen M, Mikhaylova M, Lipka J, Schlager MA, van den Heuvel DJ, Kuijpers M, Wulf PS, Keijzer N, Demmers J, Kapitein LC, Jaarsma D, Gerritsen HC, Akhmanova A, Hoogenraad CC. (2013) TRAK/Milton motor-adaptor proteins steer mitochondrial trafficking to axons and dendrites. *Neuron*. 77:485-502.
- Varadi A, Johnson-Cadwell LI, Cirulli V, Yoon Y, Allan VJ, Rutter GA. (2004) Cytoplasmic dynein regulates the subcellular distribution of mitochondria by controlling the recruitment of the fission factor dynamin-related protein-1. *J Cell Sci*. 117:4389-400.
- Venkatesh K, Mathew A, Koushika SP. (2019) Role of actin in organelle trafficking in neurons. *Cytoskeleton (Hoboken)*. 77:97-109.
- Vicente-Manzanares M, Ma X, Adelstein RS, Horwitz AR. (2009) Non-muscle myosin II takes centre stage in cell adhesion and migration. *Nat Rev Mol Cell Biol*. 10:778-90.
- Vizcarra CL, Kreutz B, Rodal AA, Toms AV, Lu J, Zheng W, Quinlan ME, Eck, MJ. (2011) Structure and function of the interacting domains of Spire and Fmn-family formins. *Proc Natl Acad Sci*. 108:11884-9.
- Wakabayashi J, Zhang Z, Wakabayashi N, Tamura Y, Fukaya M, Kensler TW, Iijima M, Sesaki H. (2009) The dynamin-related GTPase Drp1 is required for embryonic and brain development in mice. *J Cell Biol*. 186:805-16.
- Wales P, Schuberth CE, Aufschnaiter R, Fels J, García-Aguilar I, Janning A, Dlugos CP, Schäfer-Herte M, Klingner C, Wälte M, Kuhlmann J, Menis E, Hockaday Kang L, Maier KC, Hou W, Russo A, Higgs HN, Pavenstädt H, Vogl T, Roth J, Qualmann B, Kessels MM, Martin DE, Mulder B, Wedlich-Söldner R. (2016) Calcium-mediated actin reset (CaAR) mediates acute cell adaptations. *Elife*. 5:e19850.
- Wasmeier C, Hume AN, Bolasco G, Seabra MC. (2008) Melanosomes at a glance. *J Cell Sci*. 121:3995-9.
- Wei Q, Wu X, Hammer JA. (1997) The predominant defect in dilute melanocytes is in melanosome distribution and not cell shape, supporting a role for myosin V in melanosome transport. *J Muscle Res Cell Motil*. 18:517-27.
- Wellington A, Emmons S, James B, Calley J, Grover M, Tolia P, Manseau L. (1999) Spire contains actin binding domains and is related to ascidian posterior end mark-5. *Development*. 126:5267-74.
- Wells AL, Lin AW, Chen LQ, Safer D, Cain SM, Hasson T, Carragher BO, Milligan RA, Sweeney HL. (1999) Myosin VI is an actin-based motor that moves backwards. *Nature*. 401:505-8.
- Welz T, Wellbourne-Wood J, Kerkhoff E. (2014) Orchestration of cell surface proteins by Rab11. *Trends Cell Biol*. 24:407-15.
- Welz T. (2018) Mechanisms of force generation for vesicle transport processes: identification and characterisation of the Spir actin nucleator - myosin V motor protein complex. dissertation, University Regensburg. 355-epub-368567.

- Woolner S, Bement WM. (2009) Unconventional myosins acting unconventionally. *Trends Cell Biol.* 19:245-52.
- Wu X, Bowers B, Rao K, Wei Q, Hammer JA. (1998) Visualization of melanosome dynamics within wild-type and dilute melanocytes suggests a paradigm for myosin V function *In vivo*. *J Cell Biol.* 143:1899-918.
- Wu X, Bowers B, Wei Q, Kocher B, Hammer JA. (1997) Myosin V associates with melanosomes in mouse melanocytes: evidence that myosin V is an organelle motor. *J Cell Sci.* 110:847-59.
- Wu X, Rao K, Bowers MB, Copeland NG, Jenkins NA, Hammer JA. (2001) Rab27a enables myosin Va-dependent melanosome capture by recruiting the myosin to the organelle. *J Cell Sci.* 114:1091-100.
- Wu XS, Rao K, Zhang H, Wang F, Sellers JR, Matesic LE, Copeland NG, Jenkins NA, Hammer JA. (2002) Identification of an organelle receptor for myosin-Va. *Nat Cell Biol.* 4:271-8.
- Xue B, Robinson RC. (2013) Guardians of the actin monomer. *Eur J Cell Biol.* 92:316-32.
- Yang H, Wang H, Jaenisch R. (2014) Generating genetically modified mice using CRISPR/Cas-mediated genome engineering. *Nat Protoc.* 9:1956-68.
- Yu C, Feng W, Wei Z, Miyanoiri Y, Wen W, Zhao Y, Zhang M. (2009) Myosin VI undergoes cargo-mediated dimerization. *Cell.* 138:537-48.
- Zeth K, Pechlivanis M, Samol A, Pleiser S, Vonrhein C, Kerkhoff E. (2011) Molecular basis of actin nucleation factor cooperativity: crystal structure of the Spir-1 kinase non-catalytic C-lobe domain (KIND)•formin-2 formin SPIR interaction motif (FSI) complex. *J Biol Chem.* 286:30732-9.
- Zhai QY, Ge W, Wang JJ, Sun XF, Ma JM, Liu JC, Zhao Y, Feng YZ, Dyce PW, De Felici M, Shen W. (2018) Exposure to Zinc oxide nanoparticles during pregnancy induces oocyte DNA damage and affects ovarian reserve of mouse offspring. *Aging (Albany NY).* 10:2170-2189.
- Zhao LP, Koslovsky JS, Reinhard J, Bähler M, Witt AE, Provance DW Jr, Mercer JA. (1996) Cloning and characterization of myr 6, an unconventional myosin of the dilute/myosin-V family. *Proc Natl Acad Sci U S A.* 93:10826-31.
- Zhou F, Leder P, Zuniga A, Dettenhofer M. (2009) Formin1 disruption confers oligodactylism and alters Bmp signaling. *Hum Mol Genet.* 18:2472-82.

6. Supplement

6.1 Overview of used materials

All materials used in this thesis are systematically listed in this chapter. Materials for experiments not done primarily by myself (like CRISPR / Cas9 experiments, protein purification or embedding brain in paraffin blocks and cutting brain sections from paraffin blocks) are not listed here, because experiments were done by our collaboration partners or by Kerkhoff laboratory members. Most cloning experiments were done by Dr. Tobias Welz and Annette Samol-Wolf from the Kerkhoff laboratory, why all needed endonucleases for cloning of used plasmids are listed here.

6.1.2 Chemicals and reagents

Article	Quantity	Company	Order Number
Acetic acid, Rotipuran, 100 %, p.a.	1 l	Carl Roth	3738.1
Albumin standard (2 mg/ml)	10 × 1 ml	ThermoFisher	23209
Ammoniumpersulfat	100 g	Sigma-Aldrich	A3678
Ampicillin sodium salt	25 g	Sigma-Aldrich	A9518-25G
Blood bank saline	10 l	ThermoFisher	23-312-651
BM-Purple	100 ml	Roche	11442074001
Boric acid	1 kg	Sigma-Aldrich	B0252-1KG
Bovine serum albumin	1 Vial	Sigma-Aldrich	A8531
Bromophenol blue sodium salt	10 g	Carl Roth	A512.1
Citric acid	100 g	Sigma-Aldrich	251275
cOmplete Mini, EDTA-free	25 tabs	Roche	11836170001
Coomassie Plus Protein Assay, Reagent for Bradford assays	950 ml	ThermoFisher	1856210
D-MEM (HG) W/O NA PYR (CE)	500 ml	ThermoFisher	41965-062
dATP	100 µM	NEB	N0440S
dCTP	100 µM	NEB	N0441S
Denhardt's Solution 50x	5 ml	Sigma-Aldrich	D2532
Dextran sulfate	50 g	Sigma-Aldrich	D8906
dGTP	100 µM	NEB	N0042S
Digitonin	100 mg	Sigma-Aldrich	D141
Dimethyl sulfoxide (DMSO), Hybri-Max	5 × 10 ml	Sigma-Aldrich	D2650
DL-Dithiothreitol (DTT)	5 g	Sigma-Aldrich	D0632-5G
dTTP	100 µM	NEB	N0443S

Ethanol > 99.8 % + 1 % MEK	2.5 l	Carl Roth	K928.1
Ethanol > 99.8 %, p.a.	2.5 l	Carl Roth	9065.2
Ethidiumbromide solution, 0.5 %	15 ml	Carl Roth	HP46.1
Ethylenediaminetetraacetic acid tetrasodium salt hydrate (EDTA)	500 g	Sigma-Aldrich	E5134-500G
Fetal bovine serum	50 ml	Merck	F2442
Formamide	1 l	Carl Roth	6749.1
Formamide deionized	250 ml	Carl Roth	P040.1
GeneRuler 1 kb DNA	5 × 50 µg	ThermoFisher	SM0311
GeneRuler 100 bp DNA	5 × 50 µg	ThermoFisher	SM0241
Glutathione Sepharose 4B	10 ml	GE Healthcare Life Sciences	17-0756-01
Glycerine-solution for microscopy	1 vessel	Leica	11513872
Glycerol	100 ml	Merck	G5516
Glycine, 99 %	5 kg	Carl Roth	3790.3
Hydrochloric acid, Rotipuran, 25 %	1 l	Carl Roth	6331.1
Immersion liquid, Type F	1 vessel	Leica	11513859
Isopropanol, > 99.5 %	2.5 l	Carl Roth	9866.5
Kanamycin B sulfate salt	250 mg	Sigma-Aldrich	B5264-250MG
LB-Medium (Luria/Miller; 10 g/l NaCl)	5 kg	Carl Roth	X968.4
Levamisole hydrochloride	5 g	Sigma-Aldrich	L9756
Luminata TM Forte Western HRP Substrate	100 ml	Merck-Millipore	WBLUF0100
Magnesium chloride hexahydrate	100 g	Sigma-Aldrich	M2670-100G
Methanol, LiChrosolv	2.5 l	Merck-Millipore	1.06007.2500
Milk powder	500 g	Carl Roth	T145.2
MitoTracker Orange CMTMRos	20 × 50 µg	ThermoFisher	M7510
MitoTracker Red CMXRos	20 × 50 µg	ThermoFisher	M7512
MOWIOL 4-88 Reagent	100 g	Merck	475904
N-propyl-gallate	100 g	Sigma-Aldrich	P3130
Nonidet P 40 Substitute	1 l	Merck	74385
Nonidet P-40 BioChemica (NP-40)	500 ml	AppliChem	A1694,0500
Opti-MEM I (1X)	100 ml	ThermoFisher	31985-062
Paraformaldehyde	250 g	Carl Roth	0335.1
PBS buffer (10x, powder)	10 l	AppliChem	A0965,9010
Phenylmethylsulfonylfluorid, PMSF	5 g	Sigma-Aldrich	P-7626-5G
Ponceau S, practical grade	50 g	Sigma-Aldrich	P3504-50G

Precision Plus Protein Dual Color Standards	500 µl	Bio-Rad	161-0374
Protease and Phosphatase Inhibitor Cocktail	1 package	Abcam	ab201119
RNAlater™ Stabilization Solution	100 ml	ThermoFisher	AM7020
RNase AWAY	475 ml	Carl Roth	7002
Rotiphorese Gel 30, Acrylamid/Bis-Acrylamid solution	1 l	Carl Roth	3029.1
Salmon sperm DNA	1 ml	Agilent Technologies	201190
Select agar	1 kg	Sigma-Aldrich	A5054
Sodium chloride, > 98 %	1 kg	Sigma-Aldrich	S3014-1KG
Sodium citrate tribasic dihydrate	100 g	Sigma-Aldrich	C8532
Sodium dodecyl sulfate (SDS)	500 g	Sigma-Aldrich	L4390-500G
Sodium hydroxide pellets	1 kg	Merck	1064621000
TEMED	100 ml	Sigma-Aldrich	T9281
TMRM	5 × 100 µl	ThermoFisher	I34361
Tris-EDTA (TE) buffer solution	100 ml	Merck	93283
Triton X-100, for molecular biology	100 ml	Sigma-Aldrich	T8787-100ML
Trizma base (Tris)	5 kg	Sigma-Aldrich	T1503-5KG
Trypsin-EDTA solution (0.05 %)	100 ml	ThermoFisher	25300054
Tween 20, BioChemica	500 ml	AppliChem	A1389,0500
UltraPure™ Agarose	100 g	ThermoFisher	16500100
Xylol	2.5 l	Carl Roth	9713.3
Yeast t-RNA	100 mg	Merck	10109517001
β-Mercaptoethanol (12.8 M)	100 ml	Carl Roth	4227.3

Table 5 - Overview on used chemicals and reagents.

6.1.3 Cell culture media, reagents and supplements

Article	Quantity	Company	Order Number
DMEM (1X) Dulbecco´s Modified Eagle Medium	500 ml	ThermoFisher	41965-039
Dulbecco's Phosphate Buffered Saline (1X; 1x PBS)	500 ml	ThermoFisher	14190-094
HyClone FetalClone III Serum (FCS III)	500 ml	GE Healthcare Life Sciences	SH30109.03
L-Glutamine; 200 mM	100 ml	ThermoFisher	25030024
Lipofectamine™ 2000 reagent	1.5 ml	ThermoFisher	11668019
Penicillin/Streptomycin solution	100 ml	ThermoFisher	15140122

Poly-L-Lysine	50 ml	Sigma-Aldrich	P4707
Trypan Blue solution (0.4 %, sterile-filtered, suitable for cell culture)	100 ml	Sigma-Aldrich	T8154-100ML
Trypsin-EDTA (0.05 %)	100 ml	ThermoFisher	25300054
Water, sterile filtered, BioReagent, suitable for cell culture	1 l	Sigma-Aldrich	W3500-1L

Table 6 - Overview on used cell culture media, reagents and supplements.

6.1.4 Buffers, solutions and media

Buffer, solution or media	ingredients
100 mg/ml tRNA	- 100 mg in 10 ml Millipore-H ₂ O - aliquots at -20 °C
200 mM Levamisole	- 2.4 g of levamisole in 50 ml of Millipore-H ₂ O
20x SSC	- 175.3 g NaCl - 88.2 g sodium citrate tribasic dihydrate - 800 ml Millipore-H ₂ O - adjust pH to 8.0 with 1 M citric acid - fill to 1 l with Millipore-H ₂ O - 1 ml of DEPC - autoclave - solution is stored at room temperature
5 % (w/v) Milk powder blocking solution	- 50 g dry milk powder in 1 l 1x PBST - freeze 50 ml aliquots at -20 °C
7.5 % SDS polyacrylamide separation gel	- 5.7 ml Millipore-H ₂ O - 1.3 ml 3 M Tris-HCl pH 9.0 - 2.6 ml Acrylamide30 solution - 50 µl 20 % SDS - 10 µl TEMED - 50 µl 10 % APS
Agar selection plates for bacterial culture	- 25 g LB medium (Luria/Miller) - 13 g select agar - fill up with Millipore-H ₂ O to 1 l - autoclave for 20 min at 121 °C, cool to approx. 42 °C - add antibiotics
Agarose solution for gel electrophoresis	- dissolve desired amount of agarose in 0.5x TBE by boiling and shaking (1 - 2.5 %)
Ampicillin solution (10 %)	- 1 g Ampicillin sodium salt in 10 ml Millipore-H ₂ O - filter sterile and store aliquots at 4 °C
APS solution (10 %)	- 10 % Ammoniumpersulfat (w/v) in Millipore-H ₂ O - store at 4 °C
Blocking buffer	- 0.2 % BSA - 2 % fetal bovine serum - 1x PBS

Cell lysis buffer	<ul style="list-style-type: none"> - 25 mM Tris-HCl pH 7.4 - 150 mM NaCl - 5 mM MgCl₂ - 10 % (v/v) glycerol - 0.1 % (v/v) Nonidet P-40 - 1 mM PMSF - protease inhibitor cocktail
Coomassie staining solution	<ul style="list-style-type: none"> - 10 % acetic acid - 40 % ethanol - 0.6 % (w/v) Coomassie brilliant blue G250 - 0.6 % (w/v) Coomassie brilliant blue R250
DEPC-H ₂ O	<ul style="list-style-type: none"> - add 1 ml of DEPC to 1 l of Millipore-H₂O - autoclave and store at room temperature
DNA loading dye (6x)	<ul style="list-style-type: none"> - 10 mM Tris-HCl, pH 7.6 - 0.03 % bromophenol blue - 60 % glycerol - 60 mM EDTA
FACS buffer	<ul style="list-style-type: none"> - 0.5 % BSA - 2 mM EDTA - 1x PBS pH 7.2
FCSIII for cell culture	<ul style="list-style-type: none"> - inactivate at 56 °C (waterbath) for 30 min - store 50 ml aliquots at -20 °C
<i>Full Medium</i> for cell culture	<ul style="list-style-type: none"> - DMEM - 10 % FCSIII - 2 mM L-glutamine - 100 units/ml Penicillin - 100 µg/ml Streptomycin
Hybridization mixture	<ul style="list-style-type: none"> - Prehybridization buffer - add 15 µl of specific DIG-labeled RNA (final concentration of 2 ng/µl)
Hypo-osmotic buffer	<ul style="list-style-type: none"> - 10 mM NaCl - 1.5 mM MgCl₂ - 10 mM Tris-HCl (pH 7.6)
Kanamycin stock solution	<ul style="list-style-type: none"> - dissolve Kanamycin monosulfate in Millipore-H₂O (25 mg/ml) - filter sterile and store 2 ml aliquots at -20 °C
LB medium (Luria/Miller)	<ul style="list-style-type: none"> - dissolve 25 g/l in Millipore-H₂O - autoclave for 20 min at 121 °C
Mowiol solution	<ul style="list-style-type: none"> - 15 g Mowiol 4-88 in 70 ml Millipore-H₂O - 30 ml glycerol - 2.5 % (w/v) n-propylgallat - centrifuge at 17,300 × g for 15 min - store 1 ml aliquots at -20 °C
NTE buffer	<ul style="list-style-type: none"> - 100 ml 5 M NaCl - 10 ml 1 M Tris pH 7.5 - 10 ml 0.5 M EDTA to 880 ml of Millipore-H₂O - store solution at 4 °C
NTMT buffer	<ul style="list-style-type: none"> - 20 ml 5 M NaCl - 50 ml 1 M MgCl₂ - 100 ml 1 M Tris pH 9.5 to 830 ml of Millipore-H₂O - 1 ml Tween 20 - store solution at 4 °C

Paraformaldehyde solution (3.7 %)	<ul style="list-style-type: none"> - 7.4 g paraformaldehyde in 100 ml 1x PBS - 2 drops 10 M NaOH - incubate at 60 °C for at least 30 min - 100 ml 1x PBS, adjust to pH 7.4 - store 10 ml aliquots at -20 °C
PBS (10x)	- dissolve 95.5 g PBS powder in 1 l Millipore-H ₂ O
PBST (1x; 0.05 % Tween20)	- add 0.05 % Tween20 to 1x PBS
PMSF stock solution (0.1 M)	<ul style="list-style-type: none"> - dissolve in ethanol - store 2 ml aliquots at -20 °C
Ponceau S staining solution	<ul style="list-style-type: none"> - 5 % acetic acid - 0.1 % (w/v) Ponceau S
Prehybridization buffer	<ul style="list-style-type: none"> - 50 % deionized formamide - 1x Denhardt's solution - 10 mM DTT - 4x SCC - 10 % Dextran sulfate - 1 mg/ml yeast t-RNA and 1 mg/ml salmon sperm DNA
Proteinase K (10 mg/ml)	<ul style="list-style-type: none"> - 10 mg proteinase K to 1 ml proteinase K buffer - store aliquots at -20 °C
Proteinase K buffer	<ul style="list-style-type: none"> - 20 ml 1 M RNase-free Tris pH 7.5 - 2 ml 0.5 M EDTA/DEPC pH 8.0 - 978 ml DEPC-H₂O - store at room temperature
Pulldown buffer	<ul style="list-style-type: none"> - 25 mM Tris-HCl, pH 7.4 - 150 mM NaCl - 5 mM MgCl₂ - 0.1 % NP-40 - 10 % glycerol
SDS polyacrylamide stacking gel	<ul style="list-style-type: none"> - 2.6 ml Millipore-H₂O - 420 µl 1 M Tris-HCl pH 6.8 - 550 µl Acrylamide30 solution - 17 µl 20 % SDS - 5 µl TEMED - 33 µl 10 % APS
SDS protein sample buffer (5x) Laemmli buffer	<ul style="list-style-type: none"> - 100 mM Tris-HCl, pH 6.8 - 50 % glycerol (v/v) - 15 % SDS (w/v) - 25 % β-Mercaptoethanol (v/v) - 0.025 % bromophenol blue (w/v) - store 1 ml aliquots at -20 °C
SDS-PAGE-buffer (10x)	<ul style="list-style-type: none"> - 250 mM Tris - 1.9 M glycine - 1 % SDS (w/v)
TBE buffer (10x)	<ul style="list-style-type: none"> - 890 mM Tris - 890 mM boric acid - 20 mM EDTA, pH 8.0
TBST (10x)	<ul style="list-style-type: none"> - 0.5 M Tris - 1.5 M NaCl - 0.5 % Tween20 - adjusted to pH 7.4 with HCl - store at room temperature
Transfer buffer (10x)	<ul style="list-style-type: none"> - 250 mM Tris - 1.92 M glycine

Transfer buffer (1x)	- 25 mM Tris - 192 mM glycine - 20 % methanol
Tris-EDTA, pH 8.0 for plasmid DNA storage	- 20 mM Tris - 1 mM EDTA - adjust pH to 8.0 with HCl - autoclave
Triton X-100 (0.2 %)	- 0.2 % in 1x PBS
Tween20 (10 %)	- dilute Tween20 in 1x PBS
β -Mercaptoethanol solution (12.8 M)	- mix stock solution with Millipore-H ₂ O to obtain 12.8 M

Table 7 - Overview on used buffers, solutions and media.

6.1.5 Disposable materials

Article	Company	Order Number
Autoclave indicator tape (120 °C)	A. Hartenstein	STKD
BD Microlance™ 3 (0.9 × 40 mm)	Becton Dickinson	301300
Biosphere Filter Tip 100	Sarstedt	70.760.212
Blotting papers, Grade 3 MM Chr	Whatman	3030.917
Cell culture dish (100 × 20 mm)	Greiner Bio-One	664160
Cell culture plate (6-well)	Greiner Bio-One	657160
Cellstar reaction tubes, conical (15 ml)	Greiner Bio-One	188 271
Cellstar reaction tubes, conical (50 ml)	Greiner Bio-One	227 261
CryoTube Vials (1 ml)	Nunc	366656
Embedding cassette	Carl-Roth	E478.1
Microscope cover glasses, 15 mm	A. Hartenstein	DKR2
Microscope slides, Menzel-Gläser, Superfrost® Plus	ThermoFisher	J1800AMNZ
Needles, BD Microlance 3, 20G × 1.5"	BD Biosciences	301300
Nitrocellulose transfer membrane, PROTAN® BA85, 0.45 µm pore size	Whatman	10401196
Parafilm® "M" Laboratory Film	Pechiney Plastic Packaging	PM-996
Pasteur pipettes	A. Hartenstein	PP07
PCR SoftTubes (0.2 ml)	Biozym Scientific GmbH	710920
Petri dishes (94 × 16 mm)	A. Hartenstein	PP90
Pipette tips, blue (100 - 1000 µl)	Axygen	T-1000-B
Pipette tips, white (0.5 - 10 µl)	Axygen	T-300
Pipette tips, yellow (2 - 200 µl)	Sarstedt	70.760.002

qPCR reaction tubes (Strip Tubes and Caps, 0.1 ml (250))	Qiagen	981103
Reaction tubes (1.5 ml)	A. Hartenstein	RK1G
Reaction tubes (2.0 ml)	A. Hartenstein	RK2G
Sapphire Filter Tip (10 µl)	Greiner Bio-One	771261
Scalpel	Megro	147222
Syringe with needle, 1 ml 26G × 3/8", Luer	BD Biosciences	300015
T25 cell culture flask (25 cm ² , 50 ml)	Sarstedt	83.1810.002
T75 cell culture flask (75 cm ² , 250 ml)	Sarstedt	83.1813.002
TissueRuptor Disposable Probes	Qiagen	990890
Transfection tubes (5 ml, 75 × 12 mm)	Sarstedt	55.476.013
Ventilation cap tubes (14 ml)	Sarstedt	62.515.006
Videoprinter paper	VWR	PEQRCD80E1091
WillCo-Dish (Glass-bottom dish; 40 mm)	WillCo Wells B.V.	GWSt-5040

Table 8 - Overview on used disposable materials.

6.1.6 Kits

Article	Company	Order Number
DIG RNA Labeling Kit	Merck	11175025910
NucleoSpin Gel and PCR Clean-up	Macherey-Nagel	REF 740609.50
NucleoSpin RNA Kit	Macherey-Nagel	740955.50
PE/Cy7 Conjugation Kit - Lightning Link	Abcam	ab102903
QIAGEN Plasmid Maxi Kit (25)	Qiagen	12163
QIAprep Spin Miniprep Kit (250)	Qiagen	27106
QIAxcel RNA QC Kit v2.0	Qiagen	929104
QuantiNova Reverse Transcription Kit	Qiagen	205411
QuantiNova SYBR Green PCR Kit (100)	Qiagen	208052
RNeasy Midi Kit	Qiagen	75144
Seahorse XFp Cell Mito Stress Kit	Agilent Technologies	103010-100

Table 9 - Overview on used kits.

6.1.7 Antibodies

6.1.7.1 Primary antibodies

Article	Species / Clonality	Purpose	Company	Order Number
anti-c-Myc (9E10)	mouse, monoclonal	Immunostain	Santa Cruz Biotechnology	sc-40
anti-cytochrome C	mouse, monoclonal	Immunostain	ThermoFisher	33-8200
anti-Digoxigenin-AP	sheep, polyclonal	<i>in situ</i>	Merck	11093274910
anti-MYO5A (G-4)	mouse, monoclonal	FAMS	Santa Cruz Biotechnology	sc-365986
anti-SPIRE1 (SA-2133)	rabbit, polyclonal	Immunostain, Western blot	Schumacher et al., 2004	-

Table 10 - Overview on used primary antibodies.

6.1.7.2 Secondary antibodies

Article	Species	Purpose	Company	Order Number
Amersham ECL anti-rabbit IgG, HRP-linked	donkey	Western blot	GE Healthcare Life Sciences	NA934-1ML
anti-mouse TRITC	donkey	Immunostain	Dianova	715-025-151
anti-rabbit Cy5	donkey	Immunostain	Dianova	711-175-152

Table 11 - Overview on used secondary antibodies.

6.1.8 Enzymes

6.1.8.1 Restriction endonucleases

Restriction endonuclease	Concentration / Volume	Company	Order Number
<i>Bam</i> HI-HF	20,000 units/ml	NEB	R3136S
<i>Bcl</i> I-HF	20,000 units/ml	NEB	R3160S
<i>Eco</i> RI-HF	20,000 units/ml	NEB	R3101L
<i>Hind</i> III-HF	20,000 units/ml	NEB	R3104S
<i>Kpn</i> I-HF	20,000 units/ml	NEB	R3142L
<i>Nhe</i> I	20,000 units/ml	NEB	R3131S
<i>Sal</i> I	20,000 units/ml	NEB	R0138S
<i>Xba</i> I	20,000 units/ml	NEB	R0145S
<i>Xho</i> I	20,000 units/ml	NEB	R0146L

Table 12 - Overview on used restriction endonucleases.

6.1.8.2 DNA polymerases

Polymerase	Concentration / Volume	Company	Order Number
AccuPrime™ Pfx DNA Polymerase	2.5 units/μl	ThermoFisher	12344-024
Pfu DNA Polymerase	500 u	Promega	M7745
Q5® High-Fidelity DNA Polymerase	2000 units/ml	NEB	M0491S
Taq DNA Polymerase	5000 units/ml	NEB	M0273L

Table 13 - Overview on used DNA polymerases.

6.1.8.3 Additional enzymes

Enzyme	Concentration / Volume	Company	Order Number
Calf Intestinal Alkaline Phosphatase (CIP)	10,000 units/ml	NEB	M0290L
Proteinase K (genotyping)	30 units/mg	Carl Roth	7528.1
Proteinase K (<i>in situ</i>)	2 units/mg	Merck	03115836001
RNase A	7000 units/ml	Qiagen	19101
T4 DNA Ligase	400,000 units/ml	NEB	M0202L

Table 14 - Overview on additional enzymes.

6.1.9 Primer (PCR / qPCR)

Primer name	T _m (°C)	Product size	Purpose	Primer sequence (5' → 3')
SPIRE1-FW	60.03	149 bp	PCR, qPCR	AGGATGAAGGGTACGAGGCT
SPIRE1-REV	58.85			CTGATAATGATTGGGTGCCTCC
SPIRE1-E9-FW	58.63	129 bp	PCR, qPCR	GGCCACTTAGCATGTCTCAC
SPIRE1-E9-REV	58.67			CGCTCAGCCCATTTTCTTTTG
mitoSPIRE1-FW	57.71	113 bp	PCR, qPCR	TCTGTTTGAGAGAGCTTTTACCA
mitoSPIRE1-REV	59.78			GGACCTGACGGATGTGCAT
SPIRE2-FW	61.5	133 bp	PCR, qPCR	AACTGCACGAGAAGATCCT
SPIRE2-REV	64.3			ACTTGATGTCCCCAGAGCAG

<i>genoS1-FW</i>	58.6	269 bp (WT shows a specific PCR-product, <i>SPIRE1</i> mutant does not show a specific PCR-product)	Genotyping (<i>SPIRE1</i> WT / <i>SPIRE1</i> mutant)	GCATGACTCTTTGGAGAGCATT AGC
<i>genoS1-REV</i>	60.8			AGGCTACAAGAAGCTGGTCTCCA AGC
<i>genoS1-FW</i>	58.6	142 bp (<i>SPIRE1</i> mutant shows a specific PCR-product, WT does not show a specific PCR-product)	Genotyping (<i>SPIRE1</i> WT / <i>SPIRE1</i> mutant)	GCATGACTCTTTGGAGAGCATT AGC
<i>genoS1mutant-REV</i>	56.2			ATAAACCCCTCTTGCAGTTGCATC
<i>genomitoSPIRE1-FW</i>	55.82	749 bp (WT), 575 bp (mitoSPIRE1)	Genotyping (<i>SPIRE1</i> WT / mitoSPIRE1 knockout)	TCCCTCCAACCAAAAATGTC
<i>genomitoSPIRE1-REV</i>	57.57			TCAGCAGTCAAAGCAAAGTG
<i>SPIRE1-E8E13-FW</i>	58.18	687 bp (when <i>exon 13</i> of <i>SPIRE1</i> is present)	PCR (absence of <i>exon 13</i> on mRNA levels)	GCCAGAAAAGCTGAAACCAACC
<i>SPIRE1-E8E13-REV</i>	59.32			CCCAAACATGGCTGCTTCAA
<i>SPIRE1-E12E14-FW</i>	59.9	295 bp (including the <i>exon 13</i> of <i>SPIRE1</i>), 121 bp (when <i>exon 13</i> of <i>SPIRE1</i> is absent)	PCR (absence of <i>exon 13</i> on mRNA levels)	ACGAACGTGAGGCAGTTTCT
<i>SPIRE1-E12E14-REV</i>	59.78			GGACCTGACGGATGTGCAT

Table 15 - Overview on used primer for PCR and qPCR.

6.1.10 Mouse lines

Mouse line	Company
C57BL/6J	Charles River
C57BL/6N	Charles River
mitoSPIRE1 (background: C57BL/6N)	in this thesis developed mouse model
<i>SPIRE1</i> mutant (background: C57BL/6J)	Pleiser et al., 2014

Table 16 - Overview on used mouse lines.

6.1.11 Machines and equipment

Article	Company
AF6000LX fluorescence microscope (HCX PL APO 63x/1.3 GLYC objective, DFC7000 GT digital camera)	Leica
AM TIRF MC microscope (HCX PL APO 100x/1.47 oil objective, Hamamatsu EM-CCD C9100-02 digital camera)	Leica, Hamamatsu
BD FACS Aria III (fitted with a PMT detector for forward light scatter of a 488 nm laser)	Becton Dickinson
Cell counting chamber (Neubauer, depth: 0.1 mm; 0.0025 mm ²)	Paul Marienfeld GmbH & Co. KG
Centrifuge, 5417 R, refrigerated	Eppendorf
Centrifuge, 5424	Eppendorf
Centrifuge, Multifuge 1 s-r, refrigerated	Heraeus
Digital-pH-Meter	Knick
Dumont forceps Nr. 5	Dumont, (neoLab)
E-Box 3026 WL-26M (UV-Transilluminator)	PeqLab
Eppendorf Research plus 0.1 - 2.5 µl variable Pipette	Eppendorf
Eppendorf Research plus 0.5 - 10 µl variable Pipette	Eppendorf
Eppendorf Research plus 10 - 100 µl variable Pipette	Eppendorf
Eppendorf Research plus 100 - 1000 µl variable Pipette	Eppendorf
Eppendorf Research plus 2 - 20 µl variable Pipette	Eppendorf
Eppendorf Research plus 20 - 200 µl variable Pipette	Eppendorf
Forma Orbital Shaker, 37 °C	ThermoFisher
Forma Orbital Shaker, refrigerated	ThermoFisher
Humidity Chamber Plus	BioLegend
ImageQuant LAS 4000	GE Healthcare Life Sciences
KIMBLE Dounce tissue grinder set	Sigma-Aldrich
Leica DMIL (Tissue Culture Microscope)	Leica
Leica DMR microscope (PL Fluotar 10x/0.30 objective, DFC320 digital camera)	Leica
Mastercycler ep gradient S	Eppendorf
micro-scissors	Megro
Mini Trans-Blot [®] Cell	Bio-Rad
Mini-Sub Cell GT Cell (electrophoresis system)	Bio-Rad
Nanophotometer P300	Implen
POWER PAC 300 (power supply)	Bio-Rad
PowerPac TM 300	Bio-Rad
PowerPac TM Basic Power Supply	Bio-Rad

QIAxcel Advanced System	Qiagen
Rotor-Gene Q 2plex HRM Platform	Qiagen
Seahorse Flux Analyzer	Agilent Technologies
TissueRuptor	Qiagen
Water bath	Memmert

Table 17 - Overview on used machines and equipment.

6.1.12 Eukaryotic expression vectors

6.1.12.1 pAcGFP1-C1 (Clontech)

The pAcGFP1-C1 vector was used to generate SPIRE1, SPIRE1-E9, mitoSPIRE1, SPIRE1 exon 13, SPIRE2, FMN1, FMN2 and INF2 N-terminal AcGFP1 tagged plasmids for expression in HeLa cells. The cDNA expression of the vector is regulated by the strong CMV promoter and the vector has a kanamycin resistance for bacterial selection. Vector and restriction map are available in the world wide web (<https://www.addgene.org/vector-database/1663/>).

6.1.12.2 pcDNA3 (Invitrogen)

The pcDNA3 vector was used to generate a SPIRE1 N-terminal c-Myc-epitope tagged plasmid for expression in HeLa cells. The protein expression of the vector is regulated by the strong CMV promoter and the vector has an ampicillin resistance for bacterial selection. Vector and restriction map are available in the world wide web (<https://www.addgene.org/vector-database/2092/>).

6.1.12.3 pEGFP-C1 (Clontech)

The pEGFP-C1 vector was used to generate FMN2 N-terminal GFP tagged plasmids for expression in HeLa cells. The plasmid expression of the vector is regulated by the CMV promoter and the vector has a kanamycin resistance for bacterial selection. Vector and restriction map are available in the world wide web (<https://www.addgene.org/vector-database/2487/>).

6.1.12.4 pEGFP-C2 (Clontech)

The pEGFP-C2 vector was used by our collaboration partner to generate a MYO5A N-terminal GFP tagged plasmid and I used it for expression in HeLa cells. The plasmid expression of the vector is regulated by the CMV promoter and the vector has a kanamycin resistance for bacterial selection. Vector and restriction map are available in the world wide web (<https://www.addgene.org/vector-database/2488/>).

6.1.12.5 pmStrawberry-C1

The pmStrawberry-C1 expression vector is based on the pAcGFP1-C1 vector and was generated by substituting the AcGFP1 cassette by an mStrawberry cassette. This vector was used to generate mitoSPIRE1, SPIRE1 exon 13 and MYO5B N-terminal mStrawberry tagged plasmids for expression in HeLa cells. The cDNA expression of the vector is regulated by the strong CMV promoter and the vector has a kanamycin resistance for bacterial selection.

6.1.12.6 List of used constructs

Construct name	Plasmid	Internal Plasmid Number	Boundaries (restriction sites)	Purpose
GFP (AcGFP1; (*))	pAcGFP1-C1	# 201	-	mitochondrial motility study
GFP-exon 13	pAcGFP1-C1-mm-SPIRE1-exon 13	# 615	aa 521 - 578 (<i>HindIII</i> / <i>EcoRI</i>)	colocalization
GFP-FMN1A-FL	pAcGFP1-C1-mm-FMN1A-fl	# 967	aa 2 - 1430 (<i>EcoRI</i> / <i>KpnI</i>)	colocalization
GFP-FMN1C-FL	pAcGFP1-C1-mm-FMN1C-fl	# 976	aa 2 - 1204 (<i>HindIII</i> / <i>KpnI</i>)	colocalization
GFP-FMN2-FH2-C1493	pAcGFP1-C1-mm-FMN2-FH2-C1493	# 631	aa 1135 - 1493 (<i>KpnI</i> / <i>BamHI</i>)	colocalization
GFP-FMN2-FH2-FSI	pAcGFP1-C1-mm-FMN2-FH2-FSI	# 628	aa 1135 - 1578 (<i>KpnI</i> / <i>XbaI</i>)	colocalization
GFP-FMN2-FH2-FSI-K1571A	pEGFP-C1-mm-FMN2-FH2-FSI-K1571A	# 351	aa 1135 - 1578 (<i>KpnI</i> / <i>XbaI</i>)	colocalization
GFP-FMN2-FL	pEGFP-C1-mm-FMN2-fl	# 417	aa 1 - 1578 (<i>KpnI</i> / <i>BclI</i>)	colocalization
GFP-INF2-FL-CAAX	pAcGFP1-C1-hs-INF2-CAAX-fl	# 916	aa 1 - 1249 (<i>XhoI</i> / <i>EcoRI</i>)	colocalization
GFP-INF2-FL-NonCAAX	pAcGFP1-C1-hs-INF2-NonCAAX-fl	# 923	aa 2 - 1240 (<i>EcoRI</i> / <i>KpnI</i>)	colocalization
GFP-mitoSPIRE1	pAcGFP1-C1-mm-mitoSPIRE1-fl	# 626	aa 2 - 788 (<i>KpnI</i> / <i>BamHI</i>)	PCR, qPCR, mitochondrial motility study, colocalization

GFP-MYO5A-CC-GTD (*)	pEGFP-C2-mm-MYO5A-CC-GTD	# 589	aa 1260 - 1853 (<i>EcoRI</i> / <i>Sall</i>)	colocalization
GFP-SPIRE1	pAcGFP1-C1-mm-SPIRE1	# 500	aa 2 - 730 (<i>KpnI</i> / <i>BamHI</i>)	PCR, qPCR, colocalization
GFP-SPIRE1-E9	pAcGFP1-C1-mm-SPIRE1-exon 9	# 679	aa 2 - 745 (<i>KpnI</i> / <i>BamHI</i>)	PCR, qPCR, colocalization
GFP-SPIRE2	pAcGFP1-C1-mm-SPIRE2	# 502	aa 2 - 718 (<i>KpnI</i> / <i>BamHI</i>)	PCR, qPCR, colocalization
GST-FMN2-eFSI	pGEX-4T1-NTEV-mm-FMN2-eFSI	# 255	aa 1523 - 1578 (<i>BamHI</i> / <i>XhoI</i>)	GST-pulldown
mStrawberry-exon 13	pmStrawberry-C1-mm-SPIRE1-exon 13	# 613	aa 521 - 578 (<i>HindIII</i> / <i>EcoRI</i>)	colocalization
mStrawberry-mitoSPIRE1	pmStrawberry-C1-mm-mitoSPIRE1	# 627	AcGFP1 in # 626 substituted by mStrawberry (<i>NheI</i> / <i>XhoI</i>)	colocalization
mStrawberry-MYO5B-CC-GTD	pmStrawberry-C1-hs-myosin-5B-CC-GTD	# 321	aa 904 - 1848 (<i>HindIII</i> / <i>XbaI</i>)	colocalization
Myc-SPIRE1	pcDNA3-Myc-hs-SPIRE1	# 14	aa 2 - 742 (<i>BamHI</i> / <i>XhoI</i>)	colocalization

Table 18 - Overview on used eukaryotic expression vectors. (*), these expression vectors were bought from companies or generated by other laboratories and kindly provided by them. All other expression vectors were generated in the Kerckhoff laboratory (mostly by Annette Samol-Wolf and Dr. Tobias Welz); aa, amino acid.

6.1.13 Sequence related data

Protein Name	Species	NCBI Number
FMN1A	Mus musculus	XM_011239294.1
FMN1C	Mus musculus	NM_001285459.1
FMN2	Mus musculus	NM_019445.2
INF2 (CAAX)	Homo sapiens	NM_022489.3
INF2 (NonCAAX)	Homo sapiens	NM_001031714.3
mitoSPIRE1	Mus musculus	XM_006526204.3
MYO5A	Mus musculus	NM_010864
MYO5B	Homo sapiens	NM_001080467
SPIRE1	Homo sapiens	NM_020148.2
SPIRE1	Mus musculus	XM_006526207.3
SPIRE1-E9	Mus musculus	XM_006526205.1
SPIRE2	Mus musculus	AJ459115.1

Table 19 - Overview on used proteins and respective cDNA accession numbers.

6.2 Amino acids, one letter code

A alanine	C cysteine	D aspartic acid	E glutamic acid	F phenylalanine
G glycine	H histidine	I isoleucine	K lysine	L leucine
M methionine	N asparagine	P proline	Q glutamine	R arginine
S serine	T threonine	V valine	W tryptophan	Y tyrosine

Table 20 - One letter code of amino acids.

7. List of abbreviations

a.u.	arbitrary units
aa	amino acid
ANOVA	analysis of variance
ATP	adenosine triphosphate
Bio-Rad	Bio-Rad Laboratories, Inc
CIP	Calf Intestinal Alkaline Phosphatase
C _T	cycle threshold
DIG	Digoxigenin
Dm	<i>Drosophila melanogaster</i>
Drp1	dynamamin-related protein 1
ER	endoplasmic reticulum
ES cells	embryonic stem cells
FACS	fluorescence-activated cell sorting
FAMS	fluorescence-activated mitochondria sorting
GBD	GTPase binding domain
FCCP	carbonylcyanide-p- triflouromethoxyphenylhydrazone
FH1	formin homology domain 1
FH2	formin homology domain 2
FL	full-length
FSC	forward scatter
FSC PMT	forward scatter photomultiplier tube
FSC PMT-A	forward scatter photomultiplier tube area
FSI	formin-SPIRE Interaction

FYVE	FYVE-type zinc-finger
gRNA	guide RNA
GS	Griscelli syndrome
GTBM	globular tail domain binding motif
GTD	globular tail domain
<i>Hs</i>	Homo Sapiens
ID	intellectual disability
iMEFs	immortalized mouse embryonic fibroblasts
IMM	inner mitochondrial membrane
IMS	intermembrane space
INF2	Inverted formin 2
KIND	kinase non-catalytic C-lobe domain
Mfn1	mitofusin 1
Mfn2	mitofusin 2
MLPH	melanophilin
<i>Mm</i>	Mus musculus
mtDNA	mitochondrial DNA
MTR	MitoTracker Red CMXRos
MYO5	myosin 5
MYO5A	myosin 5A
MYO5B	myosin 5B
MYO5C	myosin 5C
NEB	New England Biolabs
OCR	oxygen consumption rate
OMM	outer mitochondrial membrane

OPA1	optic atrophy 1
OXPHOS	oxidative phosphorylation
PAM	protospacer adjacent motif
PCC	Pearson's correlation coefficient
PCR	polymerase chain reaction
pMEFs	primary mouse embryonic fibroblasts
qPCR	quantitative real-time PCR
RFU	relative fluorescence units
RPE cells	retinal pigment epithelial cells
SB	SPIRE-box
SHD	Slp homology domain
SMART	Simple Modular Architecture Research Tool
SSC	side scatter
SSC-A	side scatter area
ThermoFisher	Thermo Fisher Scientific Inc.
TIRF	total internal reflection fluorescence
TMRM	tetramethylrhodamine-methylester
WH2	Wiskott-Aldrich-Syndrome protein homology 2
η^2	eta squared
η^2_P	partial eta squared

8. List of Figures

Figure 1 - Mitochondrial dynamics is characterized by fission, fusion and motility	2
Figure 2 - Structure of mouse SPIRE genes and proteins	9
Figure 3 - Model of SPIRE / FMN subfamily formin cooperation in efficient actin nucleation and filament elongation	12
Figure 4 - Model for the different molecular states of the SPIRE / FMN actin nucleation complex at vesicle membranes	13
Figure 5 - Schematic overview of a vertebrate myosin 5 motor protein	15
Figure 6 - Schematic overview of the <i>highways and local roads</i> model for intracellular transport	18
Figure 7 - Model how RAB27A could regulate actin filament driven melanosome transport in melanocytes by recruiting SPIRE1 / FMN1 and MLPH / MYO5A towards melanosomes	21
Figure 8 - Schematic representation of the CRISPR / Cas9 targeting strategy used to generate the mitoSPIRE1 knockout mouse model.....	49
Figure 9 - Schematic overview of used SPIRE proteins encoded by expression vectors.....	52
Figure 10 - Schematic overview of used MYO5, FMN and INF2 proteins encoded by expression vectors.....	53
Figure 11 - Tissue specific <i>SPIRE</i> gene expression	56
Figure 12 - Brain specific <i>in situ</i> hybridization of mitoSPIRE1	57
Figure 13 - SPIRE splice variants show different subcellular localization	59
Figure 14 - Experimental setup to determine the localization of the C-terminal end from mitoSPIRE1	61
Figure 15 - The C-terminal end of mitoSPIRE1 might be located in the cytosol	62
Figure 16 - mitoSPIRE1 colocalizes with formin proteins at mitochondrial membranes.....	66
Figure 17 - Number of MYO5A positive mitochondria can be determined by fluorescence conjugated anti-MYO5A antibodies in FAMS.....	69
Figure 18 - mitoSPIRE1 targets MYO5 proteins towards mitochondrial membranes.....	70
Figure 19 - Generation of the mitoSPIRE1 knockout mouse	73
Figure 20 - mitoSPIRE1 regulates mitochondria size in mouse fibroblasts.....	76

Figure 21 - Absence of mitoSPIRE1 does not influence mitochondrial respiration rate in response to bioenergetic modulators78

Figure 22 - mitoSPIRE1 influences mitochondria motility 80

Figure 23 - Overexpression of mitoSPIRE1 influences mitochondria motility in pMEFs.....82

Figure 24 - Model for mitoSPIRE1 function in mitochondria transport85

9. List of Tables

Table 1 - Protocol for routine PCR using defined components (i) and thermocycling conditions (ii) for DNA fragment amplification by Q5 High-Fidelity DNA Polymerase.....	29
Table 2 - Protocol for routine PCR using defined components (i) and thermocycling conditions (ii) for DNA fragment amplification by Taq DNA Polymerase	30
Table 3 - Protocol for routine PCR using defined components (i) and thermocycling conditions (ii) for DNA fragment amplification by Pfx DNA Polymerase.....	31
Table 4 - Number of cells (<i>ocher</i>) and embryos (<i>blue</i>) used in experiments of Figure 22 / 23.	83
Table 5 - Overview on used chemicals and reagents.....	118
Table 6 - Overview on used cell culture media, reagents and supplements	119
Table 7 - Overview on used buffers, solutions and media.....	122
Table 8 - Overview on used disposable materials	123
Table 9 - Overview on used kits	123
Table 10 - Overview on used primary antibodies.....	124
Table 11 - Overview on used secondary antibodies	124
Table 12 - Overview on used restriction endonucleases.....	124
Table 13 - Overview on used DNA polymerases	125
Table 14 - Overview on additional enzymes	125
Table 15 - Overview on used primer for PCR and qPCR.....	126
Table 16 - Overview on used mouse lines	126
Table 17 - Overview on used machines and equipment	128
Table 18 - Overview on used eukaryotic expression vectors	130
Table 19 - Overview on used proteins and respective cDNA accession numbers.....	130
Table 20 - One letter code of amino acids	131

10. Acknowledgements / Danksagung

In erster Linie möchte ich meinem Doktorvater Herrn Prof. Dr. Eugen Kerkhoff für die hervorragende Betreuung während der letzten Jahre danken. Anregende Diskussionen, zahlreiche Labormeetings sowie viele hilfreiche Tipps seinerseits führten maßgeblich zum Gelingen dieser Dissertation. Außerdem möchte ich Herrn Prof. Kerkhoff vor allem dafür danken, dass er es mir ermöglichte an mehreren internationalen Konferenzen teilzunehmen und ein Teilprojekt meiner Forschungsarbeit an der *Northeastern University* in Boston durchzuführen.

Ich möchte mich bei sämtlichen betreuenden Professoren und Doktoren des Regensburger *GRK 2174* für das angenehme Klima und das fachliche *Feedback* bedanken. Insbesondere möchte ich mich bei Prof. Dr. Christian Wetzl, Prof. Dr. Veronica Egger und Prof. Dr. Oliver Bosch bedanken, die Teil der Prüfungskommission dieser Arbeit sind. Außerdem möchte ich Herrn Prof. Dr. Schneuwly danken, der ebenfalls Teil der Prüfungskommission ist. Ich schätze es sehr, dass die genannten Professoren sich bereit erklärt haben meine Arbeit der letzten Jahre zu begutachten und zu bewerten.

An dieser Stelle gilt mein ganz besonderer Dank der Arbeitsgruppe Kerkhoff vor allem Annette Samol-Wolf und Dr. Tobias Welz. Euch beiden ist es zu verdanken, dass ich bei experimentellen Misserfolgen stets lachen konnte und immer genug Energie hatte, um das Projekt fortzuführen. Eure fachliche Unterstützung und euer Humor vollendeten diese Arbeit letztendlich. Ich habe euch als Kollegen kennengelernt und werde das Regensburger Universitätsklinikum nach einigen Jahren mit der Gewissheit verlassen, dass aus Kollegen Freunde wurden. Danke!

In 2019 I went with some colleagues to Cold Spring Harbor to participate in a conference. During the conference I met the young and talented PhD student Hannah (Sheehan) Alberico from Northeastern University, Boston and we figured out that we have similar scientific interests, why we initiated a collaboration. At the beginning of the collaboration Hannah visited our laboratory in Germany and gave a great lecture about a novel technique called

fluorescence-activated mitochondria sorting. In spring 2019 I traveled to Boston and worked together with Hannah at my research project. I want to thank the PI of Hannah Prof. Dr. Dori Woods for the opportunity to stay and work in her lab. At this point, I want to thank Hannah for the great collaboration and for becoming a real friend! In addition, I want to thank Hannah's family for showing me Boston and bringing me to the 'real' American leisure activities (sorry Bob that these guys took your bike).

I want to thank Prof. Dr. Uri Manor, Prof. Dr. Henry Higgs, Prof. Dr. Benoit Kornmann and all the other great scientists for their scientific advices regarding my research project. I met most of the listed researchers at international conferences and I am really lucky that I could talk to these scientists.

Ich möchte mich außerdem bei meinen Freunden aus Regensburg und ehemaligen Kollegen aus der U-Bar (allen voran Krissi und Andi) bedanken. Ihr habt mir eine tolle Zeit in Regensburg bereitet, was letztendlich auch zum guten Gelingen dieser Doktorarbeit geführt hat.

Natürlich möchte ich mich auch bei meinen Freunden aus Ravensburg, meinen Eltern, meinen Brüdern und meinen Omas für die jahrelange Unterstützung bedanken.

Letztendlich möchte ich mich bei meiner langjährigen Freundin Nora bedanken. Danke, dass du so bist wie du eben bist und mit mir während allen Höhen und Tiefen lachen kannst.

„Merci vielmal“